UNIVERSITAT DE BARCELONA

Synthesis and Characterization of UV-Selective Oxide-based Transparent Thin Film Solar Cells

Alex López García

Aquesta tesi doctoral està subjecta a la llicència ***Reconeixement- NoComercial – SenseObraDerivada 4.0. Espanya de Creative Commons***.

Esta tesis doctoral está sujeta a la licencia ***Reconocimiento - NoComercial – SinObraDerivada 4.0. España de Creative*** **Commons**.

This doctoral thesis is licensed under the ***Creative Commons Attribution-NonCommercial-NoDerivs 4.0. Spain License***.

Doctoral Thesis

Synthesis and Characterization of UV-Selective Oxide-based Transparent Thin Film Solar Cells

Alex López García

UNIVERSITAT DE BARCELONA

Synthesis and Characterization of UV-Selective Oxide-based Transparent Thin Film Solar Cells

Memòria presentada per optar al grau de doctor per la

Universitat de Barcelona

Programa de doctorat en Nanociències

Autor: Alex López García

Directors: Prof. Dr. Alejandro Pérez Rodríguez, Prof. Dr. Joaquim Puigdollers González

Tutor: Prof. Dr. Alejandro Pérez Rodríguez

UNIVERSITAT DE BARCELONA

"Science, my lad, is made up of mistakes, but they are mistakes which are useful to make, because little by little they lead towards the truth."

This page is left intentionally blank.

Table of Contents

I - Acknowledgments

II - List of acronyms and abbreviations

III - Table of Figures

IVa - Preface: thesis summary and related scientific publications

V – Author contribution to publications in the thesis

1 - Chapter 1: Introduction 21

1.1 – Energy production and consumption in the XXI century society: a need to shift towards clean renewable energy sources 21

1.2 – Transparent Photovoltaics: an unconventional disruptive application 27

1.2.1 - UV-Selective TPV applications 32

1.3 – Fundamental physics of transparent solar cells 35

1.3.1 – Solar cells: principles, working mechanisms and theoretical limits 35

1.3.2 – Characterization of a Transparent Solar Cell: Optical and Optoelectronic Parameters 40

1.4 – Thesis objectives 47

2 - Chapter 2: Methodology 49

2.1 – Material deposition techniques and TPV device fabrication 50

2.2 – Material and device characterization techniques 59

3 - Chapter 3: Article compendium 63

3.1 - Introduction and context to research work and related publications 64

3.2 – First research article 81

3.3 – Second research article 91
3.4 – Third research article 101
4 - Conclusions and Outlook 113
Bibliography 116
Appendix A 118
Appendix B 120

I - Acknowledgments

A mi familia, que siempre estará ahí, mis padres, Blanca y Álvaro, gracias por haberme criado, educado y querido. Siempre habéis trabajado y os habéis esforzado para darnos lo mejor, incluso sacrificando vuestro propio tiempo. Os quiero. A mi hermano, Víctor, gracias por estar ahí, por el apoyo incondicional y por haber estado en mis peores momentos. Te quiero. A Iria, mi cuñada, me has ayudado mucho también y siempre has intentado comprenderme y apoyarme. Te quiero. A mis abuelas, Abuela Blanca y Abuela Maruja, esto también va por vosotras, ya que sin vosotras no hubiese venido el resto. Siempre he recibido apoyo y amor incondicional. Ojalá siguieseis aquí para leer estas líneas, aunque ya lo sabéis. Os quiero.

A Cris. Tú también eres mi familia, la persona que tuve la suerte de poder elegir y que decidió elegirme y que pudo amar a una persona tan compleja, caminando a mi lado durante tanto tiempo. Gracias por haber aguantado tanto este proceso y más, todo lo que hemos podido compartir juntos. Han sido años muy bonitos y muy complicados, pero por suerte has estado ahí, mi amor y mi agradecimiento no caben en esta tesis ni en ningún tipo de formato. Lo que hemos vivido juntos, lo mejor que me ha pasado en la vida. El sentimiento más bonito que he tenido, el amor de mi vida. Te quiero, siempre.

A Pedro, Pablo, Juan, Figue, también sois familia, tengo la suerte inmensa de contaros como mis mejores amigos, no sabéis lo que me alegro de que estéis, aunque a veces me hubiese encerrado y distanciado, pero igual que lo he necesitado habéis estado ahí, yo también quiero poder estar para vosotros. Os quiero.

A mis amigos y compañeros durante la etapa de Compostela: Pedro, Pablo, Cris, Verde, Antía, Varo, sin vosotros tampoco me hubiese podido graduar, en años difíciles me acogisteis sin dudarlo un segundo. Me ayudasteis cuando parecía que no se podía continuar. No sabéis lo que agradezco el haber tenido la suerte de convivir tantos años con todos vosotros. Os lo agradeceré siempre y espero que también estéis cerca siempre. Os quiero. A todos los amigos, los que ya estaban y los que he encontrado por el camino y que también han estado ahí, gracias.

A Alejandro, gracias por haberme dirigido la tesis, por haber confiado en mí, por haberme apoyado también en momentos muy complicados. No lo puedo agradecer lo suficiente. He intentado aprender lo posible de tu parte, hay mucha dedicación en lo que haces. A Víctor, gracias por aguantarme desde el minuto cero. También me lo he pasado muy bien discutiendo contigo. Me has animado y ayudado también en momentos importantes de este periodo. A Kim, gracias por haberme acogido en la UPC con las puertas abiertas y por el esfuerzo puesto sobre todo en la recta final. Ha sido un placer colaborar y trabajar con vuestro equipo tanto en la tesis como en los proyectos. Gracias por la enseñanza, la confianza y el apoyo.

A todo el equipo, tanto de IREC como de UPC. A Nacho, Jacob, Diouldé, Marcel, Yude, Fabien, Maykel, Alex J., Ale N., Iván, Max, Sergio, Zac, Angélica, Robert, Fer, Enric, Gustavo, Oriol, Zac, Edgardo, Kunal, Cristóbal, Eloi, Pablo, Gema. Gracias por los buenos momentos pasados, por el apoyo y ayuda recibidos y por las enseñanzas que he sacado de cada personalidad y cada persona. Ha sido un placer y espero de veras que os vaya bien a todos.

A todos, en cada momento, he intentado e intento aprender de todas y cada una de las personas que me he encontrado. En fin, a todos, gracias.

II - List of acronyms and abbreviations

ALD – Atomic Layer Deposition

AM 1.5G – Reference Air Mass 1.5 Global Spectrum

APV – Agrophotovoltaic

ARC – Anti-reflective Coating

a-Si:H – Hydrogenated Amorphous Silicon

AVT – Average Visible Transmittance

AZO – Aluminum-doped ZnO

BCP – Bathocuproine

BIPV – Building Integrated Photovoltaics

c – Speed of Light

C_{60} – Fullerene

CBD – Chemical Bath Deposition

CBM – Conduction Band Minimum

CCD – Charge-Coupled Device

CdTe – Cadmium Telluride

CIE – Comission Internationale d'Éclairage

CIGS – $CuInGaS_2$

CZTS – $Cu_2ZnSnSe_4$ (Sulphur Kesterite)

CRI – Colour Rendering Index

CRM – Critical Raw Material

CTL – Charge Transport Layer

CVD – Chemical Vapour Deposition

E_g – Bandgap Energy

E_C – Conduction Band Energy

E_F – Fermi Energy

E_{Fn} – Quasi-Fermi Energy of electrons

E_{Fn} – Quasi-Fermi Energy of electrons

E_{ph} – Photon Energy

E_U – Urbach Energy

EU – European Union

E_V – Valence Band Energy

E_{vac} – Vacuum Level Energy

ETL – Electron Transport Layer

EQE – External Quantum Efficiency

eV – Electron Volt

FE-SEM – Field Emission Scanning Electron Microscopy

FF – Fill Factor

FTO – Fluorine-doped Tin Oxide

GIXRD – Grazing Incidence X-Ray Diffraction

HTL – Hole Transport Layer

I – Current

IoT – Internet of Things

IQE – Internal Quantum Efficiency

ITO – Tin-oxide Indium-oxide (90 % In_2O_3: 10% SnO_2)

J – Current Density

J_0 – Saturation/Dark Current Density

J_{mpp} – Maximum Power Point Current Density

J_{ph} – Photogenerated Current Density

J_{SC} – Short-circuit Current Density

J-V – Current Density-Voltage

k_B – Boltzmann Constant

LUE – Light Utilization Efficiency

n – Diode Ideality Factor

NiO – Nickel Oxide

NIR – Near Infrared

MoO3 – Molybdenum oxide

mpp – Maximum Power Point

PCE – Power Conversion Efficiency

PDA – Post-Deposition Annealing

PDT – Post-Deposition Treatment

P – Power

p-Si – Polycrystalline Silicon

PE-CVD – Plasma-enhanced Chemical Vapour Deposition

PV – Photovoltaic

PVD – Physical Vapour Deposition

q – Electron Charge

QCM – Quartz Crystal Microbalance

R_s – Series Resistance

R_{sh} – Sheet Resistance

R_p – Parallel/Shunt Resistance

RT – Room Temperature

SLG – Soda-Lime Glass

SoA – State of the Art

SQ – Shockley-Queisser

SRH – Shockley-Read-Hall

T – Temperature

TCO – Transparent Conductive Oxide

TRL – Technology Readiness Level

TPV – Transparent Photovoltaics

UV – Ultraviolet

UVF – Ultraviolet Filtering

V – Voltage

V_a – Applied Voltage

V_{bi} – Built-in Voltage

V_{mpp} – Maximum Power Point Voltage

V_{OC} – Open-Circuit Voltage

VBM – Valence Band Maximum

VIPV – Vehicle Integrated Photovoltaics

WF – Workfunction

XRD – X-ray Diffraction

ZnO – Zinc Oxide

Zn(O,S); $ZnO_{1-x}S_x$ – Zinc Oxysulfide

Å – Angstrom

α – Absorption Coefficient

λ_{ex} – Excitation Wavelength

$\hbar$ – Reduced Plank Constant

III - Table of Figures

Figure 1: Share of cumulative power capacity by technology from 2010 to 2027, extracted from the IEA, showing that Solar PV generation is poised to be the most established and implemented renewable technology from today to short- and mid- term. The legend presents the forecasted share in the energy mix for each type by next year 2024.[4] 25
Figure 2: PV Market data from 1980 to 2021 showing the percentage of annual production per year and per technology type. In the last decade first generation silicon modules take up 95% of annual production while second generation thin film only accounts for 5%. Extracted from ref.[6]. 27
Figure 3: Data from 2000 to 2021 of thin film market share percentages out of total PV market, highlighting the dominant thin film technology types. In the last decade the market is being dominated by CdTe technologies. Extracted from ref.[6].....28
Figure 4: TPV approaches with various degrees of transmission. a) Conventional opaque PV module. b) Segmented opaque PV module. c) Non-wavelength-selective semitransparent PV. d) Non-wavelength-selective luminescent solar concentrator. e) Wavelength-selective thin film TPV. f) Wavelength-selective luminescent solar concentrator TPV. Figure reproduced with permission from ref. [7] 29
Figure 5: Power draw for different application integrations. Average power draw per device surface area applicable to TPV for various applications ranging in power draw from the Internet of Things (IoT) to electric cars. The shaded green bars correspond to the devices' average power draw (total energy consumption averaged over the full use profile, including representative periods of use and non-use), with the range capturing differences between user types and brands. An average TPV power output that is higher than the average power draw results in a completely autonomous device (infinite battery life), whereas a lower power output results in battery life extension. For comparison, the shaded grey bars show the power output of an SQ TPV under various illumination conditions. Dashed lines are also included for reference to

show a representative peak power draw for each device type. Reproduced with permission from ref.[7].....30
Figure 6: Schematic showing the ideal EQE for a wavelength-selective device, adjusted as a function of wavelength (red arrows) around the visible spectrum with varying degrees (black arrows) of visible EQE (dashed line). Reproduced with permission from ref [7] 33
Figure 7: Plot of the light utilization efficiency (LUE, defined as the product of PCE and AVT) versus AVT with referenced values for SoA devices as of 2017, near the beginning of the doctoral period. Data points are coloured according to the different type of technological TPV approach. Reproduced with permission from ref. [7].....35
Figure 8: Solar radiation spectra (AM0, AM1.5, 6000 K blackbody radiation). Extracted from ref. [28] 37
Figure 9: a) Shockley-Queisser limit for conventional PV (extracted from Wikipedia article Shockley-Queisser limit, credits to Steve Byrnes) vs b) Shockley-Queisser limit adapted for TPV (reproduced with permission from ref.[31]).....40
Figure 10: Current density-voltage characteristics of a solar cell in dark (dashed curve) and under operating conditions (solid curve)[28]. 41
Figure 11: AM1.5G spectrum from 300 nm to 900 nm and human eye photopic response.....44
Figure 12: Picture of the evaporation system used in the thesis for metal-oxide evaporation using either thermal or e-beam evaporation.....53
Figure 13: Picture of the CT-100 sputtering system used in the thesis for deposition of ZnO and ITO films.....54
Figure 14: Picture presenting the ALD deposition system used for AZO deposition on TPV devices fabricated as part of the experimental work presented in the thesis. 56
Figure 15: Picture presenting the RF PE-CVD deposition system used for a-Si:H deposition on quartz substrates and to fabricate TPV devices. 57
Figure 16: Picture presenting the spin-coater system used for C_{60} and BCP deposition as functional ETL films in TPV devices.....59
Figure 17: Optical images of oxide layers as-deposited and after post-deposition annealing treatments: (top) ZnO (bottom) NiO, on SLG substrate. 66

Figure 18: GIXRD and Raman spectroscopy of the stack FTO/ZnO(50 nm)/NiO(50 nm) to assess crystallinity and compare with different annealing processes. 67
Figure 19: Comparison of transmittance data of Glass/FTO/ZnO(50nm)/NiO(50nm) structures with different post-deposition annealing treatments. AVT experimental values are shown in the inset. 68
Figure 20: Dark J-V curves of two devices with same stack and different thickness. (right) Device with ZnO 50nm layer. (left) Same stack with 150nm of ZnO. 69
Figure 21: Transmittance spectra of ZnO/NiO devices fabricated with NiO thickness fixed at 50 nm and different thicknesses for the ZnO layer (from 100nm to 400nm). The transmittance of the SLG/FTO substrate is presented for comparison. 70
Figure 22: Raman spectra of Zn(O,S) samples grown on FTO with three different compositions and two thicknesses (100nm in light colour and 250nm in dark color). 73
Figure 23: Transmittance spectra of FTO/$ZnO_{1-x}S_x$ samples with different thickness and composition. FTO substrate transmittance spectrum is shown as reference and maximum AVT achievable. 74
Figure 24: Tauc's plots for the three different compositions and two thicknesses studied. These results show that bandgap is greatly reduced as compared with ZnO, showing bandgap below 3 eV in all cases. 74
Figure 25: Pictures presenting complete ZnOS devices with different sulphur relative content. 76
Figure 26: J-V characteristics, under AM1.5G illumination, of two different a-Si:H/oxide based devices using a MoO3 HTL and a V2O5 HTL. 79

IVa - Preface: thesis summary and related scientific publications

The work presented in this thesis book has been carried out during the period 2019-2022 within the Solar Energy Materials and Systems (SEMS) group at the Institut de Recerca en Energia de Catalunya (IREC) located in Sant Adrià del Besòs, Barcelona, Spain. The objective of this thesis was the synthesis and characterization of UV-selective transparent photovoltaic devices focusing on the use of inorganic wide-bandgap oxide-based materials and architectures, with the aim of obtaining high transparency and efficient TPV devices with a high integration potential and with features such as low-cost, stability and earth-abundance.

For the consecution of results and development of this novel research field work jump-started from state-of-the-art device architectures for UV-selective devices, which focused on ZnO absorbers. Subsequently, it was proposed to shift towards materials with a more appropriate bandgap that was best matched with the UV spectral onset in the AM1.5G spectra. The material studied was Zn(O,S) which involved the partial anionic substitution of oxygen by a chalcogenide, sulfur in this case. After an initial phase of synthesis and characterization of different compositions lying in the whole range (from oxygen-rich to sulfur-rich) as well as a screening of different materials to work as carrier selective contacts, TPV devices were successfully fabricated for the first time in literature. Device characterization suggested some device limitations that have to be overcome in order to increase the performance of the TPV devices. Afterwards, a different approach was exploited in order to obtain transparent devices. This approach relied in the use of (lower) wide-bandgap materials, that lie in the visible range. To overcome opaqueness due to unwanted absorption in the visible range the deposition of the thin films were engineered to be ultrathin, having nanometric thickness below 30 nm. For this, a-Si:H nanometric films were embedded in pure oxide-based architectures.

Throughout this doctoral period, the research performed during this thesis has resulted in the publication of 3 scientific articles in first quartile (Q1) journals with high impact factor (IF) journals, relevant to the field of materials and especially to the photovoltaic community.

Scientific publications as first author throughout the doctoral period:

A.J. Lopez-Garcia, A. Bauer, R. Fonoll Rubio, D. Payno, Z. Jehl Li-Kao, S. Kazim, D. Hariskos, V. Izquierdo-Roca, E. Saucedo, A. Pérez-Rodríguez, "UV-Selective Optically Transparent Zn(O,S)-based Solar Cells", ***Sol. RRL***, 4, 11, 2000470 (2020), doi: 10.1002/solr.202000470

IMPACT FACTOR: 9.173

A.J. Lopez-Garcia, O. Blazquez, C. Voz, J. Puigdollers, V. Izquierdo-Roca, A. Pérez-Rodríguez, "Ultrathin Wide-Bandgap a-Si:H-based Solar Cells for Transparent Photovoltaic Applications", ***Sol. RRL***, 6, 1, 2100909 (2022), doi: 10.1002/solr.202100909

IMPACT FACTOR: 9.173

A.J. Lopez-Garcia, J.M. Asensi, C. Voz, J. Puigdollers, V. Izquierdo-Roca, A. Pérez-Rodríguez, "Ultrathin a-Si:H/oxide transparent solar cells exhibiting UV-blue selective-like absorption**",** ***Sol. RRL***, 7, 7, 2200928 (2022), doi: 10.1002/solr.202200928

IMPACT FACTOR: 9.173

The report of the doctoral thesis has been structured revolving around the scientific articles produced with Alex López García as first author. These articles present the main results and conclusions extracted from the doctoral thesis carried out and reflect the research performed in the period 2019-2022. The report is divided into 4 chapters which are summarized as follows:

- Chapter 1 - Introduction: This chapter presents an introduction and the context of the energy sector, focusing on the present century and the role of renewable energies. After this, the focus will shift to the main topic of this thesis, which revolves around a novel and unconventional application in the PV realm: Transparent photovoltaics (TPV), and its

potential as a disruptive approach for the deployment of distributed applications that rely on solar energy harvesting. The evolution of TPV, from the first ideas towards the latest advancements in SoA will be commented, summarizing the different approaches towards TPV from a materials science viewpoint, discussing device strategies by types and materials. This will end in a more detailed discussion of the approach of TPV using inorganic absorbers for UV-selective applications, which try to exploit UV radiation from the Sun. This particular approach towards TPV is the core of this thesis. Continuing, we will discuss the physics of transparent solar cells, from principles and working mechanisms to their fundamental limits. Concluding the chapter, the thesis objectives are presented and summarised.

- Chapter 2 - Methodology: this chapter presents the experimental techniques and methodologies carried out during the doctoral thesis in terms of material synthesis, and device fabrication. Brief summaries of the different techniques are given and contextualized within the main work performed in the doctoral period.

- Chapter 3 – In this chapter, the main results of the thesis are presented as an article compendium. Herein, the findings arising from the work and experiments performed throughout the doctoral period are condensed. It details different successful implementations of UV-selective TPV devices as well as their characterization. Two main approaches are used and thus discussed. The first approach relies on using inorganic oxide-based materials with energy bandgaps >2 eV and another relies on the use of materials with energy bandgap <2 eV but that are engineered to be ultrathin, with thicknesses below the 30 nm and as thin as 8 nm. The chapter is structured around an introduction and context of the work and other experiments that led to the results presented in scientific journals. Afterwards, the three scientific articles where Alex Lopez-Garcia is the main author and that have been published in high impact factor (Q1) journals are presented.

The first article, *UV-Selective Optically Transparent Zn(O,S)-based Solar Cells*, is the first ever work in literature reporting on UV-selective transparent solar cells made with Zn(O,S) as the absorber material. This work paves the way towards further study of anionic substitution in ZnO in order to reduce the bandgap of the absorber and to match it to the UV

spectral onset. This potentially maximizes PCE while still being able to have a colourless and transparent absorber material, which are also key aspects that are constrained to certain values in order to have a high aesthetic value. Improving transparency will allow to implement such a technology in Building Integrated Photovoltaics (BIPV) as an architectural component that is non-obstructive to the building users and can thus be deployed in façades or in windows. The devices presented show a record PCE of 0.5%, matching the already reported SoA in pure ZnO-based TPV devices, while reaching an outstanding 69% Average Visible Transmittance (AVT).

The second article, *Ultrathin Wide-Bandgap a-Si:H-based Solar Cells for Transparent Photovoltaic Applications,* presents the first successful efforts towards TPV devices based on ultrathin a-Si:H in an otherwise pure oxide-based structure. The work systematically studies first candidate Charge Transport Layers (CTL), and confirm that it is critical to work using both types of selective contacts. The work analyses the impact of the CTLs and absorber thickness and its effect in the overall optoelectronic parameters that serve to characterize and evaluate a TPV device. The record devices rely on the structure Glass/FTO/ZnO/a-Si:H/MoO_3/ITO. Devices present AVT ranging from 50% to 69% by avoiding the use of doped a-Si:H CTLs while still reaching an efficiency of 0.5%, matching the best results in SoA for ZnO and Zn(O,S) based devices, while still having a very high transparency, virtue of the wide-bandgap oxides and the ultrathin a-Si:H film of 15 nm. It is of great interest also due to the fact that it uses materials and processes that have been up-scaled and used for industrial manufacturing of large-area solar cells. These results gave hope for improvement, as the CTLs were not greatly optimized and established a value of the degree of transparency of these structures, which is dominated by visible light absorption from the a-Si:H absorber which has the lowest bandgap in the structure.

The third article, *Ultrathin a-Si:H/oxide transparent solar cells exhibiting UV-blue selective-like absorption*, presents optimized a-Si:H/oxide structures that show record performance as compared to SoA oxide-based TPV devices, further improving the results presented in the second article. From the findings and insights presented in the mentioned article, it was possible to achieve a record result of PCE=2% while still

having moderately high AVT that still allow for exploitable TPV applications. This allowed to reach a Light Utilization Efficiency as high as 0.7%, improving on the mentioned SoA. In this case, after process optimization, the structure consisted in Glass/FTO/AZO/a-Si:H/MoO_3/ITO. In this work, the spurious visible light absorption, unwanted in this technology, is seen as a possibility to tune the transparency/efficiency trade-off. This fact potentially allows for tailored applications that can be tuned just by modification in the nanometric thickness of the a-Si:H ultrathin film. A high transparency device and a high efficiency device are presented. The best efficiency comes with the thicker absorber film (30 nm), reaching PCE=2% while the best transparency is attained with the thinner film (8 nm) showing AVT as high as 66%. Additionally, a thorough optical study of the a-Si:H films is performed, via spectrophotometry and Photothermal Deflection Spectroscopy, demonstrating that absorption still behaves in a classical manner even though the thickness is in the nanometric scale, with films as low as 8 nm. Interestingly, the complete devices are shown to present UV selective-like absorption, as shown in the Spectral Response characterization performed.

- Chapter 4 - Conclusions and Outlook: in this final chapter, the conclusions of the work carried out are gathered and condensed, analyzing the degree of completeness of the thesis objectives. An outlook into future work and possibilities for this kind of technologies will put the final remark into the work and serve for closure of the thesis.

V – Author contribution to publications in the thesis

A.J. Lopez-Garcia, A. Bauer, R. Fonoll Rubio, D. Payno, Z. Jehl Li-Kao, S. Kazim, D. Hariskos, V. Izquierdo-Roca, E. Saucedo, A. Pérez-Rodríguez, "UV-Selective Optically Transparent Zn(O,S)-based Solar Cells", ***Sol. RRL***, vol. 4, no. 11, p. 2000470, 2020, doi: 10.1002/solr.202000470

IMPACT FACTOR (IF): 9.173

In this work Álex López García fabricated UV-Selective TPV devices, reporting for the first time ever the photovoltaic effect using Zn(O,S) as an absorber material resulting in devices with PCE=0.5% and AVT=69%. This work was carried out in collaboration with Dr. Andreas Bauer, from ZSW (Zn(O,S) deposition). Álex López García envisioned and planned the experiments and participated in device fabrication. He was also responsible for the characterization of the fabricated devices. Characterization consisted in J-V measurements as well as Optical Spectrophotometry, Spectral Response and FE-SEM measurements. Álex López García also performed the analysis of the experimental data, participate in the results discussion, and the redaction of the manuscript. The resulting work was featured in the cover of the Solar RRL journal. So far this pioneering work has already been cited 18 times in scientific literature.

A.J. Lopez-Garcia, O. Blazquez, C. Voz, J. Puigdollers, V. Izquierdo-Roca, A. Pérez-Rodríguez, "Ultrathin Wide-Bandgap a-Si:H-based Solar Cells for Transparent Photovoltaic Applications", ***Sol. RRL***, vol. 6, no. 1, p. 2100909, 2022, doi: 10.1002/solr.202100909

IMPACT FACTOR (IF): 9.173

In this work, Álex López García was responsible for the synthesis of all the layers present in the devices that were studied in this experiment. He was also responsible for the characterization of the fabricated devices, performing J-V measurements and optical spectrophotometry. He was also

responsible for the optical (Transmittance and Reflectance Spectrophotometry), optoelectronic characterization (J-V characteristics and EQE) and analysis of the devices including structural (FE-SEM and Raman spectroscopy). He was responsible for performing the analysis of the experimental data, for condensing the work into a manuscript, led the manuscript redaction and results discussion and conclusions.

A.J. Lopez-Garcia, J.M. Asensi, C. Voz, J. Puigdollers, V. Izquierdo-Roca, A. Pérez-Rodríguez, "Ultrathin a-Si:H/oxide transparent solar cells exhibiting UV-blue selective-like absorption**",** ***Solar RRL***, vol. 7, no. 7, p. 2200928, 2022, doi: 10.1002/solr.202200928

IMPACT FACTOR (IF): 9.173

In this work, Álex López García was responsible for the idea and structuration of the experiments, and for the synthesis of all the films and devices present in the samples object of the study. He performed the analysis of the experimental data, manuscript redaction, including discussion of the results and final conclusions, as well as generating future avenues that have and are still being explored after the doctoral period.

1 - Chapter 1: Introduction

Technology breakthroughs have always been the motor for the advancement of civilizations and allowed for improving the material conditions as well as covering necessities for the human being since ancient times. It is not farsighted to affirm that any society has developed in parallel to these advancements. Nevertheless, technology comes at a cost. Some Energy input is needed to make a given technology work and be successfully deployed and made available for the general public. Therefore, hand in hand with technology, advances in Energy production are so critical, since without energy production there is no way of "powering" the society and all its needs. Hence, energy production and consumption are critical aspects behind the progress (or fallout) of society as we know it, since ancient times to the present times.

For the sake of brevity this section will focus on the present context, looking at the immediate past and the dynamics of today's society around Energy as well as trying to foresee the prospects of a needed change in these dynamics that society has around energy production and consumption. Given the fact that we are living a global energy crisis it is mandatory to focus on this context and present it. Hopefully, it will help the reader to better understand what is happening and to understand that it of utmost importance to make a change around these dynamics, and it will also help to get the context to raise interest in the work presented herein as well as interest in renewable energies in general and solar energy in particular.

1.1 – Energy production and consumption in the XXI century society: a need to shift towards clean renewable energy sources

To look at energy production and consumption in the XXI century it is necessary to look back into the past century. Since the Industrial

Revolution that started at the end of the XIX century and rushed into the XX century, all of the advancements in technology, commodities and logistics have come in hand with the availability of useful energy sources that have been able to completely change and revolutionize human society. This has also come with a price to pay, as our impact on Nature has been also extraordinarily harmful, forcefully modifying entire ecosystems and reducing biodiversity. To understand why it is necessary to look at the energy sources and the products of refining and using them. This aspect as well as the limited availability of some material sources bring us to the present time and the clear idea that there is a need to shift towards clean renewable energy sources. So two main factors are decisively shifting our needs towards the use of renewable energy: the limited reserves of fossil-fuels (coupled with the cost-based system that we live in, with policies that have greatly increased the extraction costs as well as the refinement processes needed to transform the raw extracted fossil based materials into final products) and the anthropogenic climate modifications associated with CO_2 emission (main by-product of burning fossil end-products) that leads to global warming and climate change.

The Industrial Revolution was made possible thanks to the shift towards the use of natural resources that were created throughout thousands of years due to physicochemical processes with timescales in the thousands of years, hence the term fossil-based. The first energy source to be exploited was coal, followed by oil and natural gas. These three fossil-based resources have been the motor of the industrial and post-industrial society and have been the main resources used up to the 21st century. In fact, they still represent an important fraction nowadays and some are even critical still. An example is the use of the diesel motor, which is the most efficient motor to transport very heavy loads and is thus employed in maritime and terrestrial transportation and logistics. The advent of electric motor is promising but there is still a lack of global infrastructure that allows for generalized and “immediate” deployment that ensures no disruption in the global chains of transportations of goods in today’s globalized and co-dependent society.

In the 20th century, an alternative energy was developed thanks to the advancements in quantum physics and nuclear physics, which is Nuclear energy, produced in fission processes. This led to the creation of nuclear

power plants that feed the electrical grid with efficient and clean energy. However, the by-products and the risks associated with their handling and disposal have led to a stall on a full-scale implementation of this type of energy. It is worth mentioning that development of this technology is still being actively pursued, with the aim of eliminating the associated risks with alternative technologies that involve the use of nuclear energy. The most renowned is the pursuit of controlled and cheap fusion technology, with the famous ITER project[1,2] as the first globally led approach towards a proof-of-concept fusion process with the future aim of designing and fabricating a prototype power plant that makes use of this process. As for fission energy, novel approaches such as next generation reactors that are powered with materials other than Uranium are in development[3].

As so, it is still important to shift towards alternative renewable energies that are clean, such as wind, hydrogen, maritime, geothermal and solar energies. These renewable energies are named this way because in our timeframe they are virtually “infinite”. This comes in hand with the first fact that was stated as a factor to push towards this kind of energy.

It is important to emphasize that for these energies to be clean it is important to assess the impact throughout the whole life-cycle (from the extraction processes of the raw materials used in the technologies to the recollection and recycling of the technologies in a way that doesn`t harm the biosphere, very much like what was discussed as the issues with nuclear energy). This comes in hand with the anthropogenic climatic change issue, that was mentioned as the other main issue arising from the use of conventional non-renewable energies.

With the context and motivations provided in a qualitative way, it is good to look at the numbers and the present and near-future scenarios to understand the potential of alternative PV applications. The International Energy Agency (IEA) provides a comprehensive summary of the Energy Economy Scenario in its World Energy Outlook[4], emphasizing the pivotal role of clean energy transitions (Figure 1). It states that PV is one of the main driving forces of global industry transformation. The report underscores the need for robust policies, market mechanisms, and international collaboration to accelerate the transition to a sustainable and resilient energy future led by renewable energies.

As of 2023, the energy landscape is undergoing significant shifts, strongly influenced by global geopolitical dynamics, economic uncertainties, and the imperative to address climate change and keep with the target of staying below a 2 ºC increase in the average global temperature. In the United States, 2022 was marked by restrictive trade measures and supply chain constraints. However, the capacity additions for PV and eolic are set to rebound in 2023, with both technologies expecting a 40% increase in capacity. India, too, anticipates growth in renewable capacity, primarily driven by onshore wind, hydropower, and distributed PV. However, challenges such as supply chain issues, low auction volumes, and trade policies might temporarily slow down utility-scale solar PV projects in India. Renewable energy auction results from 2019 to 2022 highlight the competitiveness and success of these, with 100 GW of capacity awarded. However, 20 GW remained unallocated, emphasizing the need for government auction designs that consider inflation, interest rate changes, and commodity price turbulence. Corporate Power Purchase Agreements (PPAs) are emerging as a significant driver of PV and eolic capacity expansion, with the United States leading in this area, followed by Brazil, Australia, Spain, and Sweden. The economic attractiveness of renewables, coupled with hedging against volatile power prices and sustainability goals, motivates companies to engage in such agreements, which highlights the strong effect of policy in leading to the deployment of renewables in detriment of fossil-based fuels.

Despite all the commented challenges, financial resilience in the renewable energy industry is observed. PV manufacturing is on a positive trajectory, with increasing capacity additions, while wind manufacturers face challenges stemming from high commodity prices and evolving financing environments. The global manufacturing capacity for PV is projected to reach nearly 1000 GW in 2024, meeting the demand outlined in the IEA "Net Zero Emissions by 2050 Scenario"[5]. In contrast, wind equipment manufacturing is expanding more slowly, potentially struggling to keep up with demand growth through 2030.

As the expansion of wind and PV accelerates globally, there is a growing need worldwide for policies and market rules supporting grid infrastructure and flexibility investments. In many markets, curtailment of electricity generation from wind and PV is observed due to lagging grid infrastructure

and system planning. Effective grid management becomes crucial as countries like Spain, Germany, and Ireland are expected to see their annual share of wind and PV surpass 40% by 2024, requiring measures to curb rising curtailment rates.

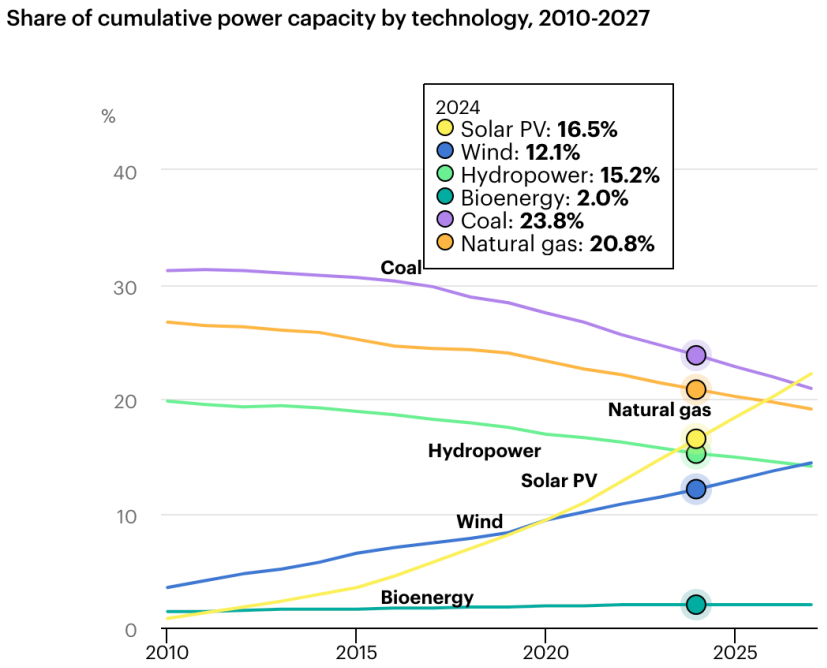

Figure 1: Share of cumulative power capacity by technology from 2010 to 2027, extracted from the IEA, showing that Solar PV generation is poised to be the most established and implemented renewable technology from today to short- and mid- term. The legend presents the forecasted share in the energy mix for each type by next year 2024.[4]

The fossil fuel era might be approaching its peak, with the oil, natural gas and coal demand expected to peak before 2030, thus setting the stage for a decline in their share in global energy supply. However, fossil fuel prices have somewhat decreased from their 2022 maximums, but markets remain tense and volatile. China, a key player in global energy trends, is experiencing an economic slowdown, potentially affecting fossil fuel demand. The scenarios presented consider China's GDP growth averaging just under 4% per year until 2030, resulting in a peak in total energy demand by the mid-2020s. A further slowdown could significantly impact coal, oil, and liquified natural gas demand, with implications for global

balances. The end of the growth era for fossil fuels emphasizes the need to redirect investments toward clean energy systems.

Despite these challenges, the emergence of a new clean energy economy, led by PV and electric vehicles, provides hope for a sustainable future. Investment in clean energy has risen by 40% since 2020, driven by efforts to reduce emissions, enhance energy security, and create clean energy jobs. PV is contributing 80% of new power capacity to 2030 in the Stated Policies Scenario. The manufacturing capacity for solar PV is projected to reach over 1.2 TW annually by the end of the decade, with China dominating the global manufacturing landscape. The analysis explores the implications of significantly scaling up solar PV deployment, potentially reducing coal-fired generation by 20% by 2030 and further decreasing fossil fuel use.

These scenarios are quite optimistic and highlight the main role of PV in the upcoming next-generation Global Energy mix. The numbers show that increased deployment in PV technologies is needed to reach the established objectives. Policies are important, but further research and industrialization of new PV applications are needed in order to extend the toolkit of PV.

1.2 – Transparent Photovoltaics: an unconventional disruptive application

Transparent Photovoltaics (TPV) is a highly innovative approach that has emerged in recent decades, as a disruptive application that promises to extend the available toolkit of PV technologies and create novel markets based on different implementations from this approach, most notably in the area of integration, possessing a distributive nature tries to strongly differentiate itself from the existing market of conventional PV.

As highlighted in the previous section, PV is leading in the deployment of renewable energy technologies. However, in order to increase PV adoption the technologies must be adapted to specific scenarios and requirements so that it is a more appealing and versatile option, extending the possible range of applications. The most standardised commercially available implementation of PV technologies so far have mainly focused on high efficiency mono- or poly-crystalline silicon solar modules. This type of modules represent almost 95% of the actual PV market, with close to a 5% being second generation PV thin film cells and modules, mainly CIGS and CdTe (Figures 2, 3).[6] Even though these are robust technologies that can find uses in various scenarios, some caveats are present, limiting its applicability in many locations and situations out.

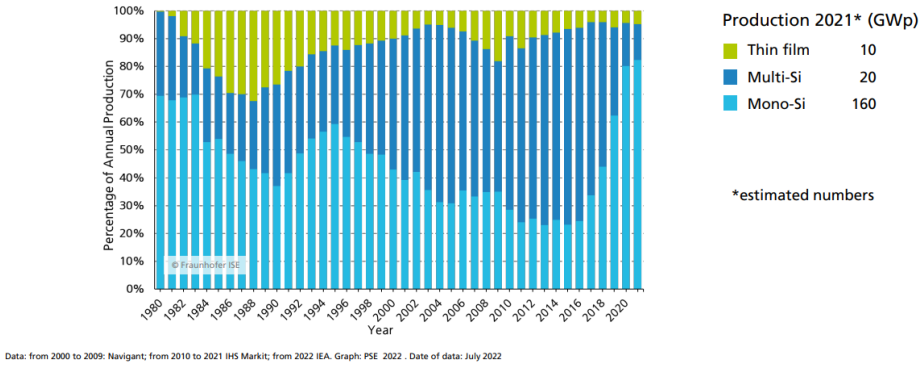

Figure 2: PV Market data from 1980 to 2021 showing the percentage of annual production per year and per technology type. In the last decade first generation silicon modules take up 95% of annual production while second generation thin film only accounts for 5%. Extracted from ref.[6].

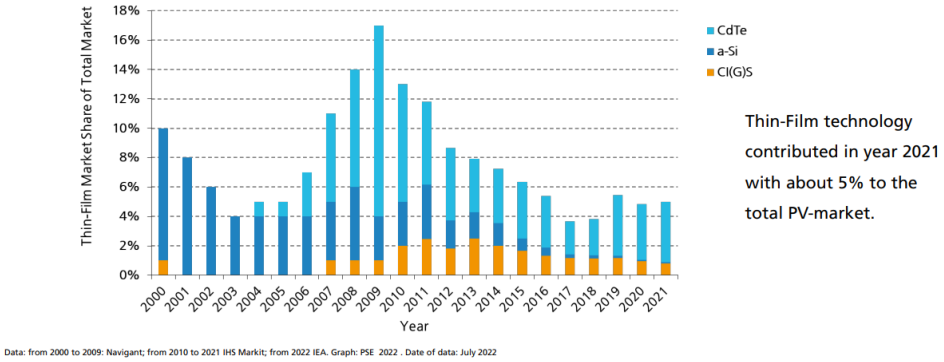

Figure 3: Data from 2000 to 2021 of thin film market share percentages out of total PV market, highlighting the dominant thin film technology types. In the last decade the market is being dominated by CdTe technologies. Extracted from ref.[6].

Additionally, different PV technologies present different limiting factors that can impede or slow their deployment or applicability in different scenarios, especially those that do not involve solar farms, which is the most sought-out application of PV technology. Specifically, for the case of Si technologies, although costs are at record lows thanks to the highly developed industry, the lack of flexibility of the technology that difficult its integration in different scenarios. The backbone circuitry of modules make them mechanically rigid, does not allow for shape variety or customization and give the modules high weight which prevents implementation in different scenarios and available surfaces. For the case of thin film technologies CdTe toxicity and material scarcity. This last factor is also a problem for other non-toxic and earth-abundant second gen PV technologies, such as CIGS or CZTS.

In order to increase adoption of PV technologies, different approaches can result in the appearance of other potential applications. Importantly, for a global acceptance of the technology by users, it is of paramount importance to move towards distributed applications and be able to provide on-site power generation, moving from industrial consumers and large-area PV installations towards utility scale and home appliances. It is a very attractive prospect, as it can allow for a non-intrusive and ubiquitous integration of PV devices in areas that were not possible with the conventional technologies that have been deployed so far.

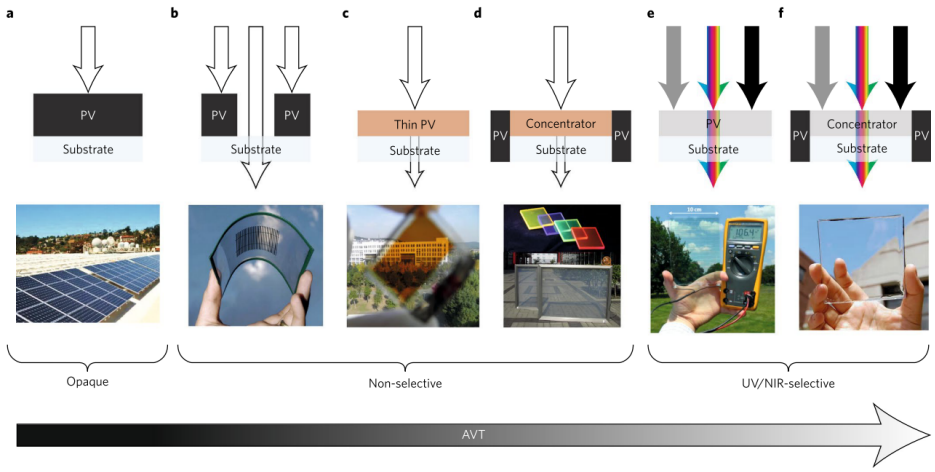

Figure 4: TPV approaches with various degrees of transmission. a) Conventional opaque PV module. b) Segmented opaque PV module. c) Non-wavelength-selective semitransparent PV. d) Non-wavelength-selective luminescent solar concentrator. e) Wavelength-selective thin film TPV. f) Wavelength-selective luminescent solar concentrator TPV. Figure reproduced with permission from ref. [7]

These factors are responsible for driving the pursuit of transparent PV applications. The possibility of alternative implementations in a ubiquitous way is very appealing and paves the way to implementation of PV into buildings and other architectural elements (Building-integrated PV, BIPV), in façades, windows and canopies; in vehicles (Vehicle integrated PV, VIPV), onto agriculture architectural elements such as greenhouses (Agrophotovoltaics, APV) and onto wearable devices, electronic display devices as well as sensors and IoT devices[8–12]. This kind of integration untaps newly available surfaces that are well suited for TPV devices and allow for an extension of the current PV technology toolkit.

When looking at the requirements for some of these potential applications, while electronic displays require high Average Visible Transmittance (AVT) values > 80%, architectural glass requirements can vary from AVT>40% up to 70%, depending on the specific scenario and legislation requirements for buildings in a given place, and PCE values above 5% can be required in such BIPV applications. However, 2–5% PCE is sufficient to self-power low-power electronic sensors and devices[7,13]. Even lower thresholds for AVT and PCE can potentially self-power smart windows or complement passive low emissivity coatings or smart windows such as

electrochromic windows, which require very low power to switch between high and low shading states (Figure 5).

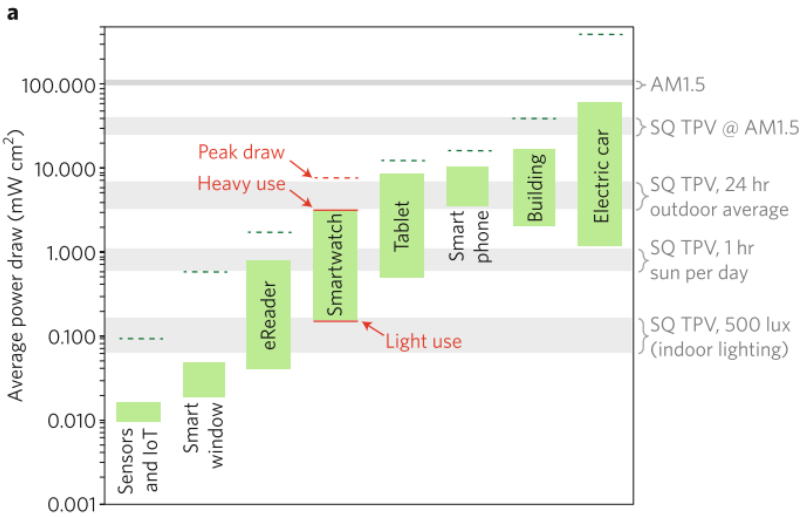

Figure 5: Power draw for different application integrations. Average power draw per device surface area applicable to TPV for various applications ranging in power draw from the Internet of Things (IoT) to electric cars. The shaded green bars correspond to the devices' average power draw (total energy consumption averaged over the full use profile, including representative periods of use and non-use), with the range capturing differences between user types and brands. An average TPV power output that is higher than the average power draw results in a completely autonomous device (infinite battery life), whereas a lower power output results in battery life extension. For comparison, the shaded grey bars show the power output of an SQ TPV under various illumination conditions. Dashed lines are also included for reference to show a representative peak power draw for each device type. Reproduced with permission from ref.[7].

As so, due to the nature of this approach, TPV has to deal with optimization of transparency, colour neutrality (or aesthetics) and power conversion efficiency (PCE). With this in mind, different variants of TPV technologies are categorised according to their absorption nature and device engineering concept. (Figure 4). A first classification deals with concentrator and non-concentrator technologies. Concentrator TPV technologies use dyes or scattering effects to capture incident light normal to a surface and redirect the light through the substrate towards its edges, where conventional opaque PV cells are grown so that the light is harvested with high efficiency (Figure 4d,f).

This thesis is focused on non-concentrator technologies. For non-concentrator technologies in TPV, it is possible to distinguish between wavelength-selective and non-wavelength-selective technologies depending on the absorption nature of the materials. For the case of non-wavelength-selective technologies, the development of this kind of TPV has relied on using spatially segmented opaque PV on glass substrates (Figure 4b) or on thin film absorbers with low thicknesses (in the nm range) (Figure 4c). With the latter approach it is possible to achieve high transparency but at the cost of a reduction in maximal attainable PCE due incomplete absorption due to the reduced thickness as well as the introduction of colour due to partial absorption in the visible range, as the bandgap of the materials used with this approach lie in the visible range. These in fact were the first reports found on scientific literature for TPV, which mostly revolved around semi-transparent PV devices by substituting metal contacts by transparent conductive oxides (TCO) in a-Si:H, CIGS technologies. However, these devices presented very low transparency values (AVT<10%) and strong colouring due to the bandgap (E_g) of the materials and the absorber thickness. With the former approach of segmented PV, opaque cells are manufactured on transparent substrates such as glass or PET. Again, different works have been presented in literature for Si or CIGS[14,15]. However, this approach depends more on the spatial arrangement and spacing between the opaque cells for a given area, so there is a direct trade-off between how much transparent area is present in comparison with the active area available for the cells. Therefore, this kind of approach, even though it can be considered part of a TPV application, is not as innovative and challenging compared to the rest of the described approaches for obtaining truly transparent and semi-transparent PV structures. Nonetheless, it is clear that they can find niche application cases where this kind of arrangement might be enough and where PCE is still needed to be comparable to commercial modules.

Concluding with the classification of TPV approaches, wavelength-selective approaches appear as the most innovative and attractive prospect in TPV. In this case, wavelength-selective approaches can be either UV-selective, IR-selective and UV/IR-selective. The first case is the topic of this thesis and is presented in more detail in the following subsection. For the case of IR- and UV/IR-selective, only nanotubes, salts and organic excitonic materials can be exploited. This is due to the fact that some

molecules can be engineered in such a way that variations in their molecular size and orbitals can be designed or tuned in order to present strong optical absorption in both the UV and IR ranges, while minimising the absorption in the visible range. Optical absorption in organic and molecular semiconductors occurs in specific quantized molecular orbitals (S_1, S_2, …, S_n) separated from the ground state (S_0). The gap between the S_1 and S_2 levels can be accessed to allow visible light transmission and UV/NIR-selective absorption by controlling the molecular structure. By modifying the bandgap and the discontinuity of states it is possible to tune the solar harvesting outside of the visible band and into the NIR[7].

1.2.1 - UV-Selective TPV applications

Focusing into UV-selective TPV devices, this area of TPV is perhaps one of the least studied so far, with most of the works being developed in the last decade. Specifically, this is the application that has been studied and developed throughout this thesis.

As the name hints, it is based on selectively absorbing UV radiation while avoiding absorption in the visible range as much as possible. When dividing the AM1.5G spectrum in UV, visible and IR, the UV region of the AM1.5G spectrum has lower potential for high PCE, due to the lower photon current density in this region as compared with the other two spectral ranges. Looking again into Figure 6, the ideal UV-selective device would present a squared EQE with 100% EQE for all wavelengths from 300 nm to 400 nm while having 0% EQE for all wavelengths from 401 nm up to the end of the reference AM1.5G spectrum. However, the pursuit is very interesting for many applications that do not rely on maximal efficiency, as the power generated from the UV-selective TPV devices might be enough to power smart devices, sensors, screens and other low-power draw devices. Additionally, UV light is typically harmful and degrades materials (especially organic materials) and is harmful for humans. So, absorbing and/or reflecting this light would potentially serve to filter out the unwanted light and exploit it as useful energy through the PV effect.

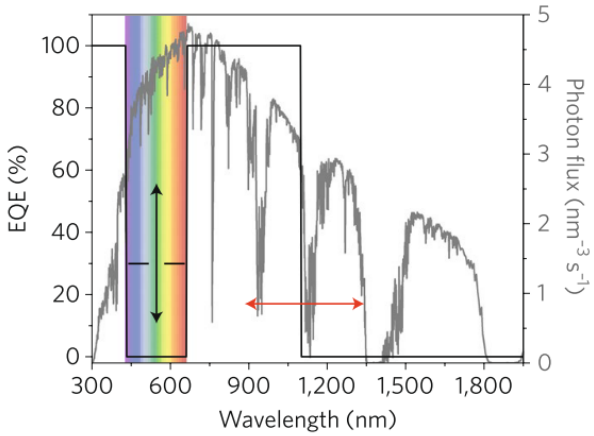

Figure 6: Schematic showing the ideal EQE for a wavelength-selective device, adjusted as a function of wavelength (red arrows) around the visible spectrum with varying degrees (black arrows) of visible EQE (dashed line). Reproduced with permission from ref [7]

Given these aspects, it is obvious that the most promising and straightforward approach would be to work on inorganic materials. Inorganic materials can be easily found in nature and are typically more resistant to UV radiation damage. It is also worth mentioning that some efforts on organic materials and hybrid perovskites have also tried to tackle this problem. However, issues as degradation might be a problem for this approach, as organic materials are prone to degrade under UV light, posing a problem in terms of long-term stability.

Oxide materials are attractive materials for the development of UV-selective devices, as these materials have good properties such as high radiation resistance, high breakdown voltages, stability, low cost, abundance, and are generally non-toxic. Among this family, ZnO presents high absorption coefficient in the UV and a direct energy bandgap of 3.3 eV[16,17]. To date, state-of-the art UV-selective solar cells rely on ZnO as the absorber material, but devices are strongly bottlenecked in terms of power conversion efficiency (PCE) as state-of-the-art (SoA) devices have not been able to surpass 0.5% efficiency for AM1.5G illumination[18–21].

Importantly, ZnO is spectrally mismatched with the complete UV spectral range, as its bandgap of 3.3 eV is higher than the UV spectral onset, located around 2.7 eV. Even more importantly, for an increase of photocurrent and maximizing PCE, when looking at the AM1.5G irradiation spectra, there

is a exponential increase in photon flux when transitioning from the shallow UV range towards the blue region of the visible spectrum. Moving towards 2.7 eV can potentially allow for PCE values close to 5% while still presenting very colour neutrality with high transmission in the visible region. Then it is interesting to dispose of a material with such properties, which in fact becomes possible by anionic substitution of oxygen by sulphur forming $ZnO_{1-x}S_x$ mixed crystals. Theoretical and experimental results have shown that by anionic modification the resulting material presents a bandgap bowing with a minimum at the intermediate sulphur relative content ratio of x=S/(S+O)=0.5 corresponding to a bandgap around 2.7 eV. Thus Zn(O,S) becomes a very attractive candidate for UV-Selective TPV absorber[22–25].

As part of this thesis work, this approach is explored and developed, showing that indeed it is possible to fabricate the mixed crystals across the whole compositional range, demonstrating for the first time in scientific literature devices working and presenting PV effect based on the use of Zn(O,S) as absorber. These results can be found in Chapter 3 of this thesis.

In Figure 7, as a starting point with SoA data from 2017 (close to the starting date of the doctoral period), a graph depicting PCE and AVT as a function of AVT is presented, showing the reported devices and their parameters and the potential limits for the different approaches for TPV (non-wavelength-selective and wavelength-selective). Looking closely into the data it can be seen that very few works on inorganic non-selective and wavelength-selective TPV devices are present, and the ones present are almost entirely located in very low Light Utilization Efficiency (LUE) values and with very low AVT.

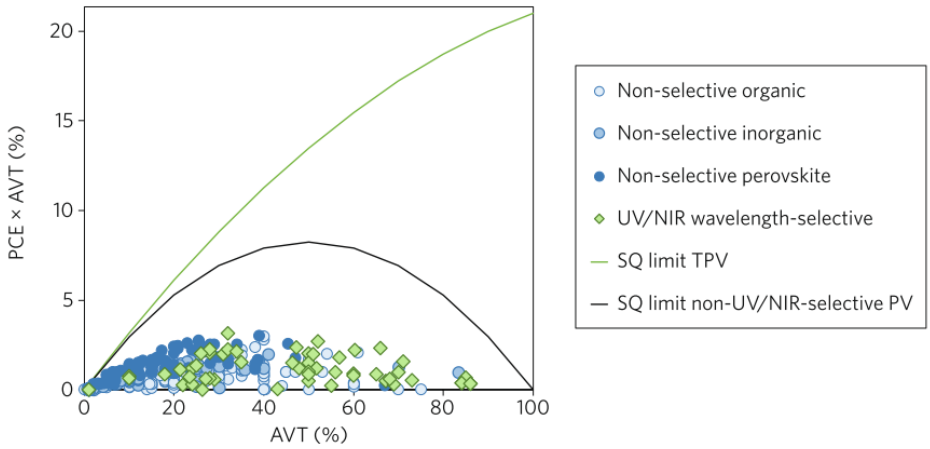

Figure 7: Plot of the light utilization efficiency (LUE, defined as the product of PCE and AVT) versus AVT with referenced values for SoA devices as of 2017, near the beginning of the doctoral period. Data points are coloured according to the different type of technological TPV approach. Reproduced with permission from ref. [7].

1.3 – Fundamental physics of transparent solar cells

This section relies on several reference scientific textbooks[26–28]. The fundamental physical mechanisms of solar cells and the energy conversion processes will be covered herein in a brief manner. As such, different concepts will be invoked along the way, but will not be derived in detail. For a complete picture on semiconductors and solid state physics the reference textbooks are excellent to expand on these aspects in a more rigorous and detailed way.

1.3.1 – Solar cells: principles, working mechanisms and theoretical limits

A solar cell is a device composed of different layers of materials that can absorb photons from the Sun's incoming radiation and convert it into electrochemical energy within the material with the final aim of collecting

this energy to be stored away or used on-site to power other devices. The sequential processes of generation, conversion, and collection mechanism compose the process of the photovoltaic effect. Hence, in short, solar energy conversion requires a photon-radiating energy source (in this specific scenario the case the Sun's electromagnetic radiation impinging on Earth's surface, characterised by the standard AM1.5G spectrum), an absorbing structure/material (typically inorganic or organic semiconductors with bandgap in the range of 0.8 eV to 3.2 eV that can absorb a certain portion or the whole of the Sun's radiation spectrum), some selective filters that can allow for the transport of one type of charge carrier and block it for the counterpart charge carrier separate the two types of electrical charges involved (or both types at the same time, for the case of the prototypical pn junction), and an external electrical circuit connected to the opposite electrical contacts of the solar cell that extracts and collects these charge carriers which carry the converted electrical energy. The efficient combination of all these aspects will determine the final output of the devices (i.e. their efficiency and power output).

The primal aspect of the solar cell is not the solar cell itself, but the photon source. In this case, obviously, it is the Sun. Photons are the energy carriers that emerge from the Sun and are radiated towards Earth, and transport a given energy current density per photon energy interval. The Sun can be modelled as a black-body, which only emits light with a specific spectrum that depends on its surface temperature, which in this case corresponds to 6000 K. The spectrum at Earth's surface is different due to absorption by different molecules (mainly O_2, O_3, H_2O, CO_2, NO_2, CH_4) as well as microparticles (PM_{10}, $PM_{2.5}$) present in the atmosphere, reducing the amount of photons arriving at the surface. Absorption in the atmosphere increases as the atmosphere path (and its mass) increases for the photons which impinge at a zenith angle, β, given by:

$$l = l_0 \cos \beta$$

The ratio l_0/l corresponds to the called air-mass coefficient (i.e. $(\cos \beta)^{-1}$). The standard spectrum used in PV characterization is the AM1.5G, corresponding to an air mass ratio of 1.5 and includes direct and diffuse radiation. In fact a standard is defined for uniformity (ASTM G-173-03) according to the ISO 9845-1 norm. Figure 8 presents the solar irradiance or energy current density per wavelength interval as a function of

wavelength, before entering Earth's atmosphere, at the top of the atmosphere (AM0 spectrum), at Earth's surface at a zenit angle of 48º (AM1.5G spectrum) and the model black-body spectrum for T = 6000 K.

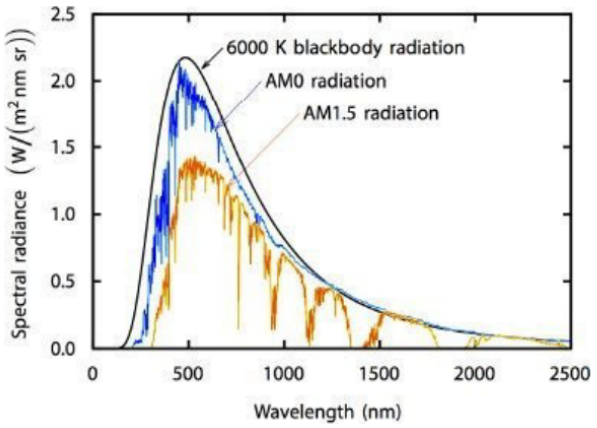

Figure 8*:* Solar radiation spectra (AM0, AM1.5, 6000 K blackbody radiation). Extracted from ref. [28]

With the source established and quantified it is the time to get into the solar cell structure. For solar cells, several structures have been designed and employed in literature, such as p-n junctions, p-i-n junctions and Schottky diodes, as examples. Basically, they all consist on an absorber material and some other materials that selectively filter the photogenerated carriers and allow for charge transport towards an external circuit. The work presented in this dissertation consists on a pin-like structure, consisting on an absorber material (in this work either Zn(O,S) or a-Si:H) and Charge Transport Layers (CTLs), one to selectively transport negative charge carriers, the Electron Transport Layer (ETL) and another to selectively transport positively charged carriers, the Hole Transport Layer (HTL).

The main feature of the absorber material, a semiconductor, is the occurrence of a gap in the energetic band distribution, where no energy states exist. This defines the bandgap energy (E_g), which is the energy difference between the bound states (Valence Band, E_v) and unbound states (Conduction Band, E_c). Electrons that are in the valence band can be promoted towards the conduction band if they receive at least the amount of energy defined by the bandgap and participate in charge transport. If the electron leaves the valence band it leaves a state which is said to be in

positive charge state, generating what is called a hole, which is a virtual particle depiction helpful for the description of charge transport in semiconductors. This process happens constantly in semiconductors for T>0 K. However, the energy can also come in the form of another process. In this case, photon absorption, with photon energies above the bandgap energy result in the creation of additional electron-hole pairs in the absorber material. This photon absorption is material dependent and is characterised by the absorption coefficient ($\alpha(\lambda)$ [cm^{-1}]) of the semiconductor material. The higher the absorption coefficient, lesser the thickness needed for the absorber material to absorb incident light.

As commented, the structure used in this thesis is based on an absorber material that is embedded between an ETL and an HTL which are connected to two opposite electrodes, which is the ideal model of a solar cell. So after light absorption and carrier photogeneration in the absorber material, carriers must get extracted from the absorber. This process happens through the ETL for the case of electrons and through the HTL in the case of holes. These are called selective contacts. Thus, an ETL will present some energetic barrier that blocks or impedes the flow of holes towards this contact, while being favourable in energetic terms for an electron to pass through it and leave the cell through the electrical contact. Similarly, an HTL will present some energetic barrier doing exactly the opposite, so that the holes can flow through the HTL and leave the solar cell through the other electrode towards the external circuit. These energetic barriers can be formed in different ways, with one of the most common being a junction with doping contrast (i.e. p-n junction). Another option is to couple materials with different work functions, which is the case presented here.

Let us assume that the absorber material is intrinsic and defect-free and analyse what happens under illumination. Upon illumination, with photon energy exceeding the bandgap, photogenerated electrons and holes are created and undergo recombination in order to reach equilibrium. Electrons originating from the ETL recombine with holes emanating from the HTL. Essentially, the electrochemical potential of electrons, as determined by the quasi-Fermi energy level E_{Fn}, equilibrates with the electrochemical potential of holes, E_{Fp}, originating a carrier flow through the external circuit. However, equilibrium under continuous illumination

is not reached. This continuous illumination separates the electrochemical potentials of electrons and holes, thereby sustaining a dynamic carrier flow seeking equilibrium. The gradient of the quasi-Fermi levels across the semiconductor establishes the driving force for the photogenerated current. In the absence of selective contacts, electrons and holes may recombine through the external circuit, mainly at the semiconductor/electrode interface. The introduction of selective contacts induces asymmetry, resulting in a sustained current. It is important to note that if electronic states lying within the absorber gap (i.e. defects) or at the semiconductor/selective contact interface exist, this will induce recombination of photogenerated electrons and holes without traversing the external circuit, thus leading to a reduction in the generated photocurrent.

Another relevant scenario is that in where electrodes are disconnected during solar cell illumination (i.e. open-circuit condition), a voltage emerges across both electrodes. Again, photogenerated electrons and holes contribute to the formation of quasi-Fermi levels for electrons and holes respectively (E_{Fn}, E_{Fp}). Subsequently, the electrochemical potential of the electrode linked to the absorber layer via the ETL aligns with the average energy of electrons in the absorber. A similar equilibrium is established with the opposite electrode in contact with the absorber through the HTL. The open circuit voltage is determined by the energy difference of the quasi-Fermi levels of electrons and holes.

Finally, to conclude, a solar cell will present some fundamental limits in the process of energy conversion. The most common approach is the one taken by Shockley and Queisser[29,30], based on thermodynamics using the principle of detailed balance, which serves to provide an upper limit for the Power Conversion Efficiency (PCE) of an absorber material as a function of its energy bandgap, E_g. It takes some approximations, as assuming that there is only radiative recombination, only one electron-hole pair is generated per photon, carrier mobility is taken to be infinite for both carrier types, as well as complete photon absorption for photon energies higher or equal than E_g. The calculation by detailed balance determines the PCE as a function of bandgap. This calculation results in the graph presented in Figure 9a. This result takes into account complete absorption above the bandgap of the absorber.

Contextualizing into transparent and semitransparent PV, the theoretical limits change slightly, depending on the absorption in the visible range (and thus its resulting EQE in this range). This approach was taken and derived by Lunt et al.[31] in order to adapt the classical S-Q limit approach for conventional opaque PV into the novel context of TPV. A similar figure of PCE as function of energy bandgap is given, as presented in Figure 9b.

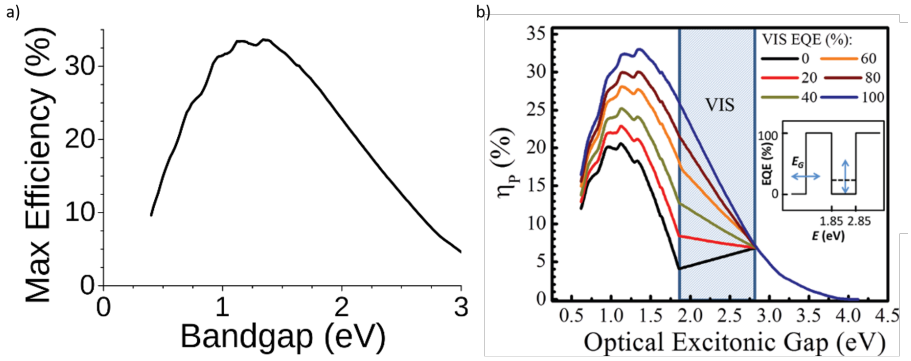

Figure 9: a) Shockley-Queisser limit for conventional PV (extracted from Wikipedia article Shockley-Queisser limit, credits to Steve Byrnes) vs b) Shockley-Queisser limit adapted for TPV (reproduced with permission from ref.[31])

1.3.2 – Characterization of a Transparent Solar Cell: Optical and Optoelectronic Parameters

To characterize any energy-transforming technology there must exist some control parameters that are a direct feature of the conversion/collection process and can allow for a standardised and objective quantification of some features. In the case of laboratory-scale solar cells one of the most important parameters, if not the most, is the efficiency of photon energy conversion (to electrochemical energy). This is typically denoted as the power conversion efficiency (PCE). This parameter is calculated indirectly from other parameters extracted from the electrical current density-voltage (J-V) characteristics (explained in the coming sections in more detail) of the solar cell under operating conditions. These parameters are: short-circuit current density (J_{sc}), open-circuit voltage (V_{oc}) and fill factor (FF). Finally, another important parameter is the external quantum efficiency (EQE).

In the case of transparent solar cells, we must introduce additional parameters to characterize and also quantify the degree of transparency as well as colour neutrality, which are features of paramount importance for the selection and implementation of a given TPV technology. The degree of transparency is characterised through the Average Visible Transmittance (AVT). The degree of colour neutrality is usually characterised by the Colour Rendering Index. Finally, an additional parameter is introduced in TPV technologies that connects the efficiency parameters of conventional solar cells with the transparency values of transparent devices, denoted as Light Utilization Efficiency (LUE). All these parameters will be discussed and derived in the following lines.

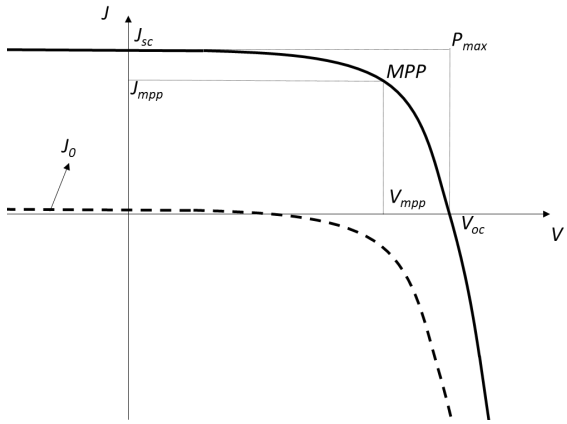

Figure 10: Current density-voltage characteristics of a solar cell in dark (dashed curve) and under operating conditions (solid curve)[28].

Recalling the working mechanisms of a solar cell, the electronic behaviour is equivalent to a diode. Thus, its J-V characteristics will typically present a curve with an exponential profile when positively (i.e. forward) biased. By measuring the J-V characteristics of a solar cell it is possible to extract parameters that can be related to the performance of the device. First, a solar cell can be characterised by measuring the J-V characteristics in dark conditions. This measurement allows extracting some interesting parameters that can be related to the quality of the materials and the junction itself. The main parameters that are usually obtained from this curve are the dark saturation current (J_0) as well as the diode ideality factor (n). From these values one can estimate non-ideal aspects of the solar cell. However, the solar cell is expected to work in other range of conditions,

basically it will be subject to some bias and work under some illuminant, in this case under solar irradiation. To uniformly compare different solar cells coming from different labs, the standard illumination is according to the AM1.5G spectrum, which is the equivalent of the spectral illumination and the power arriving at Earth's surface. For this, systems with artificial light sources that mimic these conditions in lab conditions are typically used for characterisation.

When measuring the J-V characteristics of a solar cell under illumination, the solar cell will reach steady-state conditions, out of equilibrium due to the light-matter interaction with the solar cell, particularly the absorber material. Compared to the dark curve and in an ideal case, the J-V curve under illumination would be identical in shape, but will be shifted towards another quadrant in the J-V phase space due to the additional photogenerated carriers that are generated, separated and collected, resulting in a net power output (Figure 10). From this curve the parameters that are used to calculate the solar cell efficiency are obtained. The solar cell is swept from negative to positive voltage, obtaining the J-V curve, which will cross at least three quadrants in the J-V space.

The short-circuit current density (J_{sc}) is calculated with the device subject to no electrical polarization (V= 0 V) and corresponds graphically to the intersection of the J-V curve with the y-axis. In the ideal case, it should match the photogenerated current (J_{ph}), however real solar cells typically don't match it due to different recombination mechanisms that can limit this value. Importantly, J_{sc} is a parameter that can be associated with the external quantum efficiency of the device.

The open-circuit voltage (V_{oc}) is calculated with the device subject to no current through the solar cell and graphically corresponds to the intersection of the curve with the x-axis. It is the point at which the dark saturation current density equilibrates with the photogenerated current, and corresponds to the maximum voltage that a solar cell can deliver. This value is closely related to the bandgap of the semiconducting material used as absorber.

When operating a solar cell to extract a useful power output, it is trivial to see that the solar cell will not operate in short-circuit neither open-circuit conditions. Power density results from the product of current density times

voltage. Thus, the operating point of the solar cell will be that voltage and current density conditions that yield maximum power. This condition is known as maximum power-point (mpp). Fill factor (FF) is derived from the following relationship:

$$FF = \frac{J_{mpp}V_{mpp}}{J_{sc}V_{oc}} \quad (1)$$

where J_{mpp} corresponds to current-density at mpp and V_{mpp} corresponds to voltage at mpp.

With all of these parameters it is possible to extract the power conversion efficiency (PCE) of the device. Again, this value is a ratio between the maximum power extracted from the device to the total incident power (P_{in}) on the solar cell (determined by the illumination conditions):

$$PCE = \frac{P_{max}}{P_{in}} = \frac{J_{mpp}V_{mpp}}{P_{in}} = \frac{J_{sc}V_{oc}FF}{P_{in}} \quad (2)$$

Finally, an additional characterization is performed to assess the collection efficiency at a given wavelength, which characterises the spectral response of the whole device, taken into account different electrical and optical loss mechanisms. The external quantum efficiency (EQE(λ)) is defined as the fraction of incident photons that create electron-hole pairs in the absorber material which can be effectively collected. From this spectrum it is possible to extract J_{sc} when integrating the product of the EQE times the photon flux of the AM1.5G spectrum, in short-circuit conditions, across the AM1.5G spectral range (the actual photovoltaic response spectral range of the absorber can also serve as integration limits). The relation is as follows:

$$J_{sc} = q\int_{\lambda_1}^{\lambda_2} EQE(\lambda)\Phi_{ph,\lambda}^{AM1.5G}d\lambda \quad (3)$$

Where q corresponds to the electron charge, and $\Phi_{ph,\lambda}^{AM1.5G}$ to the AM1.5G photon flux or photon current density.

Thus, the EQE can serve as a control parameter that can extract *Jsc* and compare it to the *Jsc* obtained via the J-V characteristics under illumination to confirm that no overestimation resulted from the J-V measurements,

typically due to geometric considerations such as a miscalculation of total device area that could artificially increase the PCE value.

As commented, additional parameters are required to characterise a TPV device, these are optical parameters that are related to perceived device transparency and aesthetic properties as colour. The first one is the AVT, which can be obtained by optical spectrophotometry and subsequent integration of the spectrum weighting in the photon flux of the illumination source as well as the human eye's photopic response (Figure11). As shown in Figure 11, the eye's photopic response under moderate to high illumination intensities is represented by a gaussian curve that is centered about 555 nm, reflecting that the eye is mostly sensitive to wavelengths corresponding to green colour tones[32].This makes AVT a representative parameter that more accurately relates the perceived transparency than just averaging across the visible spectral range. AVT is calculated from the following relation:

$$AVT = \frac{\int T(\lambda)P(\lambda)S(\lambda)d\lambda}{\int P(\lambda)S(\lambda)d\lambda}$$

Where λ corresponds to the photon wavelength, T is the transmittance, P is the photopic response and S is the photon flux, in this corresponding to the standard illumination conditions AM1.5G. Thus, AVT gives the ratio of transmitted photons weighting in the photon range to which the human eye is most sensitive.

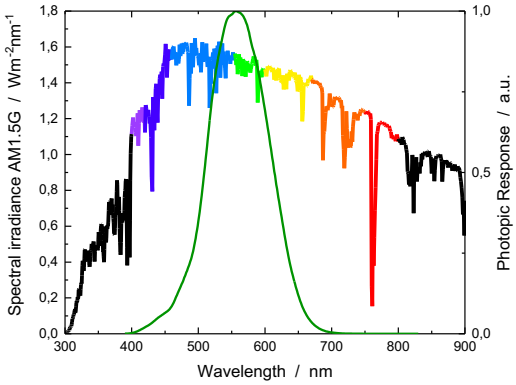

Figure 11: AM1.5G spectrum from 300 nm to 900 nm and human eye photopic response.

AVT gives information of transparency, but for many applications this is not enough to assess the aesthetic properties of the technology. In terms of perceived colour or degree of colour neutrality, the parameter that takes this into account is the Colour Rendering Index (CRI). In the window industry, CRI is applied to evaluate the ability of portraying a variety of colors of the transmitted daylight through glazing compared to those observed directly under daylight without the glazing[33] In this case it describes the perceived colour across a transparent medium, the transparent solar cell, comparing it with the colour depicted respect to an ideal illumination source, which can be a blackbody radiator at some specific colour temperature, under daylight conditions or in this case under the AM1.5G spectra. The CRI is a value that goes from 0 to 100. As an example, a transparent medium that yields CRI > 70 is considered of high quality. As reference, a perfect colour neutral source or transparent medium would yield CRI=100.

For CRI calculations of TPV devices the test light source will correspond to the product of the AM1.5G spectrum and the device transmittance of the full device architecture. Integrating the CIE 1931 xyz functions with the the source spectra will give the tristimulus values which are converted to the coordinates used in the CIE 1931 color space (CIEXYZ)[32].The tristimulus values of different light sources are then converted into (u,v) coordinates in CIE 1960 uniform colour space (CIELUV).

The relations for conversion from 1931 xy coordinates to 1960 uv coordinates in terms of the tristimulus values X,Y,Z:

$$u = \frac{4X}{X + 15Y + 3Z}$$

$$v = \frac{6Y}{X + 15Y + 3Z}$$

The definition of colour takes chromaticity and luminosity. A colour sample will exhibit colour differences and thus different chromaticity coordinates as well as luminosity when comparing the reference source (X0, Y0, Z0) to the transmitted source (i.e. the TPV device; Xt, Yt,Zt). The luminosity for the reference source (i.e. AM1.5G) is 100 while for the

transmitted source it will be the ratio of transmitted light.The differences in this chromaticity and luminosity in the CIE1960 colour space are the quantities used to determine the CRI through the following relation:

$$CRI = \frac{1}{8}\sum_{i=1}^{8}\left[100 - 4.6\sqrt{(\Delta u_i^*)^2 + (\Delta v_i^*)^2 + (\Delta L_i^*)^2}\right]$$

Where 8 different tabulated test sources are averaged in order to obtain the variation in chromaticity coordinates (Δu_i^*, Δv_i^*) as well as the luminosity (ΔL_i^*).

In summary, the characterization of a transparent solar cell involves most of the typical characterization of conventional solar cells, focusing on the extraction of the same parameters, with the added optical characterisations that involve the quantification of transparent and aesthetic properties of the transparent device.

To conclude with the optoelectronic characterization standards for a TPV device, a final measurement check consists on the so-called Photon Balance Check. This measurement serves as a check to confirm that the photocurrent extracted from the characterization has not been overestimated, for example, because the TPV sample device has been characterised under illumination placing it on top a white or reflecting matt, which would cause extra reflection paths and thus artificially increase the Jsc and thus the PCE value for the samples. It takes into account energy conservation in the form of A+R+T=1. To confirm that indeed no overestimation is taken when characterising the J-V characteristics this relation is transformed taking into account the EQE, leading to EQE+R+T≤1. This relation must hold for all wavelengths contained in the illumination source and EQE, R and T should be independently measured as a standardised consistency check in TPV characterization[33].

1.4 – Thesis objectives

The fundamental objectives of this doctoral thesis are summarized in the following lines and they consist on the development of oxide-based devices that selectively absorb in the UV range and present very high Average Visible Transmittance (AVT) and Colour Rendering Index (CRI) values as a characteristic in order to have colour-neutral and optically transparent TPV devices. Additionally, the idea is to develop devices that are multifunctional, in the sense that they will also be required to have a high degree of UV filtering that adds to the PV characteristics of the devices. The goal established by the end of the doctoral period was highly ambitious given the available state of the art (SoA), with the aim of obtaining devices with PCE=2.5%, AVT=40% and UVF=99%, with high CRI. These goals are established as part of an ambitious H2020 European Project, Tech4Win[34], and the work performed was mainly carried out within the framework of this project. In this context three main objectives were proposed:

1. Develop processes and protocols for controlled synthesis of nanometric oxide thin films that worked as active functional films. Use different characterization techniques that can help to better understand and refine the mentioned deposition processes.

2. Develop ZnO films and shift towards the development of Zn(O,S) mixed crystal absorbers, which allow for a bandgap reduction towards the specific onset of UV radiation in the AM1.5G spectrum, in order to maximize potential photocurrent and efficiency while being able to have high transparency and excellent colour neutrality. Develop novel ultrathin a-Si:H/oxide structures as an alternative strategy towards TPV and explore its limits in terms of transparency, efficiency and colour neutrality.

3. Identify potential limitations in the resulting devices and main loss mechanisms, proposing the continuity of the research line and finding potential alternatives that lead to the fundamental efficiency and transparency limits of the TPV architectures.

The consecution of these objectives has led to an established and dedicated research line in the SEMS group. It has helped to gain understanding and expertise on this application and has advanced the knowledge that existed so far. Within a broader context, the consecution of the objectives has resulted in high impact publications with a notable number of citations while presenting record devices that improved on the currently available SoA, as compared with what was presented in literature at the beginning of this thesis, were few works reported on working, efficient devices.

2 - Chapter 2: Methodology

In this section, the methodology used throughout the thesis is presented. Fundamental aspects of the different synthesis and device fabrication techniques as well as characterisation techniques used for the consecution of this thesis are introduced and put into context of the experimental work carried out.

The first subsection will describe the methodology most strongly related to the synthesis of the different materials used and the method that lead to device fabrication. Following this initial subsection, in a similar manner, a description of the characterization techniques as well as their capabilities and advantages for material and TPV device is presented in the second subsection. The different equipment and systems used throughout the thesis are presented and described, concluding with a description of what has been done and explaining where it has been applied in the context of the three scientific articles that compose this thesis.

This chapter serves as a detailed introduction and complement for the experimental section of each thesis article, all of which are presented in Chapter 3. The different synthesis and characterization techniques presented throughout this chapter have served to establish robust methodologies that have allowed for the fabrication of different types of TPV architectures and to characterize their electrical, optical, physico-chemical, morphological and TPV properties. These methodologies have been taken as standard practices for the development of a novel research line within the SEMS Group revolving on Transparent PV devices based on wide-bandgap inorganic materials and has established the new generated knowledge in the research team which is being applied in on-going projects and future projects to be developed.

2.1 – Material deposition techniques and TPV device fabrication

Different fabrication/synthesis techniques have been studied and used during this research period for material synthesis and full TPV device fabrication. The techniques are described and contextualized within this work in the following lines and are related to the experimental work presented in the article compendium.

As a reference for the reader, the architecture utilized in device fabrication throughout this thesis (except for some specific variations which will be explicitly stated) is as follows: SLG/FTO/CTL/Absorber/CTL/ITO. SLG/FTO has been the choice as the standard substrate for device fabrication.

In this case, commercial SLG/FTO (Merck) substrates of different sizes have been used. Some benefits of using SLG/FTO as substrate and back-contact include high conductivity at high transparency with high colour neutrality, high chemical stability and resistance to many acids, as well to low surface roughness. This chemical resistance is very handy, as it allows to easily reach the back contact once the complete stack is deposited by simple wet etching using acidic solutions, which selectively remove the remaining layers but will stop directly on top of the FTO, as it cannot be etched by these solutions. FTO can only be etched by a combination of Zn powder and HCl. When it is subject to acid alone, such as HCl, HF or Aqua Regia it will resist the chemical attack and its properties remain the same as before.

As a generalization, most of the CTLs explored have relied on oxide compounds, except for some notable exceptions like C_{60}. The most used material in this case as Hole Transport Layer (HTL) have been MoO_3, V_2O_5, NiO. As Electron Transport Layer (ETL) we have explored again different sets of oxide compounds, mainly ZnO, aluminium-doped ZnO (AZO), SnO_2, TiO_2, C_{60}. To deposit these layers, we have resourced to chemical vapour deposition (CVD) and physical vapour deposition techniques (PVD), such as Atomic Layer deposition (ALD) for the former deposition type and sputtering and evaporation for the later.

For the deposition of the absorber materials, we have also explored some of these techniques depending on the material of choice. The main absorbers that have been explored throughout the doctoral period have been ZnO, Zn(O,S) and a-Si:H. For the first two materials PVD techniques have been the main approach for depostion, using either conventional or reactive sputtering. For the later material, CVD techniques have been the standardised approach, relying on Plasma-Enhanced Chemical Vapour Deposition (PE-CVD) as the synthesis technique. All the techniques used throughout the doctoral period are described in the following lines.

Thermal and electron beam evaporation

The most used deposition method has been evaporation (either thermal or electron beam). This is a PVD method with a simple and straightforward working mechanism: in a high vacuum chamber (10^{-6} mbar) a material is indirectly or directly heated up to its vaporization. A substrate is placed in a rotating substrate holder with a given geometry and at a specific distance, depending on the configuration of the evaporation system. The vaporised atoms that are in a gaseous state then reach the substrate and will condense on its surface by physisorption, to later begin the nucleation and film formation process. The rotating holder ensures thickness uniformity across the xy surface of the substrate. To control total film thickness and deposition rate, typically in the order of nanometres, a complex system based on a quartz crystal microbalance (QCM) is used. This system consists of a quartz layer with metallic electrodes, which are typically made from either gold or silver. Once a material is impinging on its surface it will offset the characteristic or natural frequency of the quartz crystal, which is a well-known quantity with very low degree of uncertainty. As this natural frequency is very sensitive and its value can be calculated to great precision, the frequency shifts (which are proportional to the evaporated material quantity, i.e. thickness), which are previously calibrated by methods which lie out of the scope of this work, can assess and give a value of thickness rate which is usually presented in angstroms per second ($Å s^{-1}$) allows for high control of thickness in the nanometric scale. It is worth noting that, for better crystallisation, the substrate can be heated up and different gases can be introduced in the vacuum chamber

during deposition such as oxygen, in order to control the stoichiometry of oxide compounds.

For the e-beam evaporation technique, most of the previous applies, the main, albeit important, difference is the method used to heat and vaporize or sublime a material. Thermal evaporation is a Joule effect process, where a high intensity current is applied towards a crucible or boat (typically a metal). This heats up and the evaporant material (i.e. source) is directly heated by this dissipation, reaching eventually its vaporization. For the e-beam evaporation, an electron flux is ejected using high voltage and extracting electrons from a tungsten filament. This high energy electron flux is then oriented using magnetic fields and made to impinge directly onto the material source. Energy transfer is way higher than in thermal evaporation, as there the material is indirectly heated (the boat is the heated element) whereas in electron beam evaporation the material is heated as a result of the collision (and energy deposition) of the electron flux onto the material, causing direct heating. This is why electron beam is typically used to deposit thin films of materials that have high evaporation temperatures. This method allows in some cases for more controlled deposition depending on the material of choice. So it adds versatility to the evaporation deposition technique.

In this thesis, an Oerlikon Univex 250 evaporation system (Figure 12) was used for both thermal and electron beam evaporation, within IREC's facilities. NiO films were deposited by electron beam evaporation. NiO pieces (Alfa Aesar; 3–12 mm, 99.995%) were used as evaporant in a 4cc Al_2O_3 liner (Neyco). The chamber was evacuated at a base pressure of 10^{-6}mbar at room temperature, with no intentional heating. The high voltage power supply was set at 10 kV and with an electron current of 9 mA, resulting in a deposition rate of 0.5 $Å s^{-1}$ measured with an Au-coated quartz crystal microbalance (Inficon SQC-310). MoO_3 films were deposited using thermal evaporation starting from raw MoO_3 powder (99.995%, Alfa Aesar) as evaporant, containing the material in a tungsten boat. The chamber was pre-evacuated to a base pressure of 10^{-6} mbar and deposition took place at a rate of 0.3 $Å s^{-1}$ as measured with an Ag-coated 6 MHz quartz crystal microbalance (Inficon SQC-310). These materials were used as Hole Transport Layer (HTL) in TPV devices presented in the article compendium.

Figure 12: Picture of the evaporation system used in the thesis for metal-oxide evaporation using either thermal or e-beam evaporation.

Sputtering

Sputtering is a PVD technique in which a material source (typically known as target) has its surface atoms ejected due to the action of ionized atoms in a plasma, and similarly to evaporation, the ejected atoms will reach a substrate and condense onto its surface, generating again a nucleation process that leads to the growth of a thin film. In this process, a high voltage flows from source to substrate. The vacuum in this case, under operation, is in the mid vacuum range (10^{-2}-10^{-4} mbar). Nonetheless, the chamber is previously evacuated to high vacuum and the target is typically pre-sputtered (while having some shutter at either source, substrate or both). This is done to remove any surface contaminants of an air-exposed tarfet, leading to a pristine target surface with the expected purity that will be used for the deposition process. To begin the sputtering process, after the high-vacuum, some quantity of either inert or reactive gas (e.g. Ar, Ar/O2) is injected, building up the chamber pressure to the mid vacuum range. Then some power is applied (can be DC, DC-Pulsed or RF), and once the threshold voltage is reached, it will lead to the gas ionization and result in a plasma. This plasma has different constituents (electrons, photons, neutral atoms and ionized atoms). The ionized atoms will reach the target surface and collide with its surface atoms. These ejected atoms will cross the plasma and reach the substrate and condense into a thin film in the substrate surface. It is worth noting that these atoms have higher

order of kinetic energy than for the case of evaporation, and can thus result in damage onto the substrate surface, so it is important to work in very specific and controlled conditions (that are strongly dependent on chamber geometry and volume, target size, distance target-substrate, gas atmosphere, etc.) for a successful thin film deposition. This technique is usually used to deposit thin films with thickness around the hundreds of nm and even in microns, thanks to a higher throughput due to higher deposition rates than in thermal evaporation.

In the context of this thesis ZnO and ITO films have been deposited via DC-Pulsed Confocal Magnetron Sputtering using an Alliance CT-100 sputtering system (Figure 13) in a top-down configuration. For ZnO, deposition was carried out using a ZnO target (Neyco, 4N). Depsotion took place with no intentional heating (i.e. just residual heating from the plasma) at a working pressure at 10^{-3} mbar in a pure Argon (Ar) atmosphere at 40 sccm at a DC power density of 1.8 Wcm^{-2}. The total thickness was always adjusted by total deposition time after having calibrated the thickness rate previously. Similarly, the ITO front electrode was deposited using this same technique and starting from an ITO target (Neyco, In_2O_3/SnO_2 90/10 wt%, 4N). Prior to deposition the substrate was heated up to 200ºC nominal temperature at a working pressure of 10^{-3} mbar in a mixed Ar/O_2 atmosphere at 30/0.5 sccm at a DC power density of 1.9 Wcm^{-2}.

Figure 13: Picture of the CT-100 sputtering system used in the thesis for deposition of ZnO and ITO films.

Atomic Layer Deposition (ALD)

Atomic Layer Deposition is a quite modern technique for the deposition of thin films with layer-by-layer precision, typically in a sequential basis taking advantage of on-surface self-limiting chemical reactions thus being able to controllably deposit ultrathin and thin films with controlled stoichiometry in the nanometric and even sub-nanometric scale, even on high aspect-ratio structures. For this, the process uses some precursor materials which are transported to a chamber with a well-controlled atmosphere that can have inert or reactive gases. Excellent conformality, controlled stoichiometry and tuneable composition are some of the features that have established the technique as a powerful tool both in research as well as at an industrial scale level, the later possible in the recent years. Due to its versatility, it has been adopted as a tool for material deposition in a plethora of applications. It allows for the deposition of elemental metals as well as different compounds (oxides, nitrides, sulfides and other variations). The deposition technique was first developed in the 1970s and the first commercial systems were available around 1990. The standard deposition method is thermal ALD, although nowadays many variations exist, such as Plasma-enhanced ALD, spatial ALD or atmospheric ALD.

To illustrate the working mechanisms of this technique, the most resourced method is the Al2O3 deposition as an ideal model of an ALD process. The prototypical deposition of Al2O3 relies on trimethylaluminium (TMA) and water (H2O) as aluminium and oxygen precursors respectively. As commented, the reactions occur on-surface on a given substrate. In this process the surface chemistry can be described as:

$$a)\ AlOH^* + Al(CH_3)_3 \rightarrow AlOAl(CH_3)_2^* + CH_4$$
$$b)\ AlCH_3^* + H_2O \rightarrow AlOH^* + CH_4$$

Here the asterisks indicate surface species. The growth process occurs in sequential exposures to doses of TMA and H2O in a strictly self-limiting chemical reaction, due to the strong Al-O bond. The overall reaction can be written as:

$$2Al(CH_3)_3 + 3H_2O \rightarrow Al_2O_3 + 3CH_4$$

This reaction has a very high reaction enthalpy of $\Delta H = -376$ kcal. By repeating the surface reactions cyclically Al2O3 growth occurs in a linear

(layer-by-layer) manner that matches the number of “ab” reaction cycles. Typical growth rates found during ALD growth rates are 0.11-0.12 nm (i.e. one Al2O3 monolayer) per “ab” cycle, depending on temperature in the reaction chamber. As commented, the process usually follows a self-limiting reaction pathway that neglects the effective chemical vapour deposition (CVD) process to occur, as the surface saturates with some reactants at the surface, so higher exposures are evacuated from the chamber without affecting or etching any surface bonds. The next reaction cycle begins and follows the same process, resulting in this overall self-limiting behaviour, which is a unique feature of ALD processes. It is worth noting that this does not necessarily occur for any reactant and reaction processes can have quite different kinetics for a given target material based on different precursors.

In the context of this thesis, the ALD technique has been used to deposit ZnO as well as aluminium-doped ZnO (AZO). These materials have been implemented in devices presented within the article compendium. To deposit the materials a Savannah S200 ALD (Cambridge Nanotech) deposition system (Figure 14) located in a clean room laboratory was used. To deposit an AZO film, diethylzinc (DEZ, 95%, STREM), ultrapure H_2O and TMA (99%, STREM) were used as zinc, oxygen, and aluminium precursors, respectively. N_2 was used as purging gas. The sequential process consisted in 21 supercycles with a DEZ:TMA ratio of 19:1, with 19 $H_2O/N_2/DEZ/N_2$(20 ms/3 s/15 ms/3 s) cycles and 1 $H_2O/N_2/TMA/N_2$(50 ms/1 s/20 ms/5 s) cycle. This process formed a 75 nm AZO film, which acted as Electron Transport Layer (ETL) in TPV devices.

Figure 14: Picture presenting the ALD deposition system used for AZO deposition on TPV devices fabricated as part of the experimental work presented in the thesis.

Plasma-enhanced Chemical Vapour Deposition (PE-CVD)

Chemical Vapour Deposition (CVD) is a deposition technique that, in short, relies on precursor gases that are mixed in a chamber, resulting in a reaction that forms a given element or compound which later condenses on a given substrate, a continuous exposure leads to growth of a nanometric scale thin film in a controllable manner. This technique was developed in the 1950-1960 period, and nowadays it is an established tool for research and industrial applications.

Several variations of this type of application exist. In the context of this thesis, radio-frequency (RF) plasma-enhanced chemical vapour deposition (PE-CVD) has been a deposition method used to deposit ultrathin hydrogenated amorphous silicon (a-Si:H) films that have been studied with optical techniques and that have been used as absorber material in TPV devices. Films with controlled thickness (8, 15, 30 nm) have been synthesised. For this synthesis process an Elettrorava PE-CVD deposition system (Figure 15) was used with an RF power supply of 13.56 MHz at 6 W. The substrate temperature was set at 220ºC-250ºC during deposition, and the substrate was exposed to a SiH_4/CH_4 atmosphere of 36/12 sccm respectively, with process times ranging from 1 min (yielding 8 nm) to 4 min (yielding 30 nm a-Si:H films), in a controlled and reproducible manner.

Figure 15: Picture presenting the RF PE-CVD deposition system used for a-Si:H deposition on quartz substrates and to fabricate TPV devices.

Spin coating

Spin coating is a deposition technique that is basically used in research environments, as it a very cheap, quick and fairly simple technique to grow a wide variety of thin films, with control in the micrometric and/or nanometric scale. To deposit these films, a solution containing the target material dissolved in an adequate solvent is prepared previous to the deposition process. In the initial step, the solution is cast onto the substrate that can be either spinning previous to the casting process (dynamic spin coating) or on a still substrate that will be rotated after solution casting (static spin coating). Once spinning, the centrifugal motion will spread the solution across the substrate, while the remainder of the solution that is unadhered to the substrate will be removed. During spinning, the adhered solution will begin to thin, dominated by viscous forces and as an action of the centrifugal force that happens upon spinning at high speeds. Once this happens the solution becomes thinner due to solvent evaporation eventually leading to the formation of the desired film thickness. Solvent evaporation is often assisted with the help of a hot-plate, as mild heating typically leads to complete solvent removal. The spin coating process, as well as the solution preparation and the evaporation process steps can be either performed in air atmosphere or can be carried out in an inert atmosphere, typically working in a glovebox under N2 atmospheres.

In the context of this thesis, an Ossila spin-coater (Figure 16) was used to deposit fullerene (C_{60}) and bathocuproine (BCP) nanometric films, that were used as ETL layers in functional Zn(O,S)-based TPV devices presented in the article compendium. In order to deposit C_{60}, a solution was prepared by dissolving C_{60} (TCI, 99.5%) in 1,2-dichlorobenzene with a concentration of 10 $mgmL^{-1}$. The solution was filtered using a polytetrafluoroethylene (PTFE) filter with 420 nm pore size. The films were deposited by static spin-coating at 1500 rpm for 60 s and transferred to a preheated hot-plate at 80ºC in air for 2 min. To deposit BCP, a solution was prepared dissolving BCP (TCI, 99.0%) in dry isopropanol (IPA) at 0.6 $mgmL^{-1}$. The solution was then filtered with a 220 nm pore size filter. The films were statically spin-coated at 5000 rpm for 30 s.

Figure 16: Picture presenting the spin-coater system used for C_{60} and BCP deposition as functional ETL films in TPV devices.

2.2 – Material and device characterization techniques

During the doctoral period, different characterization techniques were systematically used on both material thin films and TPV devices. The most used characterization techniques relied on optical and electrical probing, while other characterization techniques were used to assess other properties such as film morphology, uniformity and physicochemical composition. This characterization has allowed for material identification as well for extracting relevant functional parameters of the films and devices fabricated as well as to understanding the performance of the devices and the origin of different loss mechanisms present. During the thesis period the characterization techniques applied to this research were based in the following techniques:

Field Emission Scanning Electron Microscopy (FE-SEM)

In the context of the thesis, FE-SEM micrographs have been taken and used as a tool to assess the morphology of the different layers, using it in Plan View, and to observe a transversal picture of completed TPV devices in Cross Section, which also allowed for layer thickness estimation in the nanometric range. These micrographs have nanometric resolution allowing to individually distinguish the different layers present in full TPV devices.

The micrographs were acquired using a Zeiss Series Auriga microscopy system available at IREC. Most of the images presented in the thesis are taken by analysis of secondary electron emission collected by an Everhart-Thornley detector or by using the system InLens detector. Normal operating conditions consisted on using an accelerating voltage of 2 to 5 kV, and working distances ranging around 3-5 mm, depending on the sample, working with a 20 μm aperture in order to avoid charge leakage or build-up in the thin films. The system was routinely used to assess the correct deposition, morphology and uniformity of most of the thin films deposited throughout the doctoral period.

Raman spectroscopy

Raman measurements have been performed using a tailored Raman probe setup developed by the characterization team at the SEMS group in IREC which had been optimized for the UV–Visible spectral region using a FHR640 Horiba Jobin-Yvon monochromator. This system is coupled with an open electrode Charge-Coupled Device (CCD) detectorcooled down to -75 °C. The measurements were performed in back scattering configuration through a specific probe designed at IREC and using unpolarised conditions. He-Cd laser was used as excitation source, with a wavelength of λ_{ex} = 325 nm. The measurements were always performed with laser power density below 25 Wcm^{-2}, using a "macro" spot with a diameter around 50 μm. These measurements were used in this thesis to routinely study material thin films. Specifically, it was a very important tool for the characterisation of Zn(O,S) films, because through a methodology previously established at IREC it allowed for the assessment of the relative sulphur content of the mixed crystals. Raman spectroscopy was also used to assess qualitatively the effect on the apparent crystallinity of oxide thin films used in some devices and side-experiments.

Optical Spectrophotometry (UV-VIS)

Spectrophotometry is a very simple yet complete optical characterization tool that can yield important insights into the optical properties of thin films and complete TPV devices.

In the context of this thesis, optical spectrophotometry has been routinely used to extract the Transmittance and Reflectance of the different films and, importantly, used to characterise the TPV devices presented in the article compendium. The standard characterisation routine consisted in using the tool, a Perkin-Elmer L950 UV-VIS-IR spectrophotometer, in transmittance mode and either in single-beam or dual-beam configuration. The characterisation results in a spectrum, usually spanning from the UV range to the visible or IR range in some cases (300-800 nm or 300-1500 nm typically). The spectra represent the transmittance/reflectance at a given wavelength in the spectral range. From these values (as commented previously in Chapter 1) it is possible to make use of an algorithm that yields the AVT value of complete TPV devices, which is one of the main parameters used in TPV to assess the degree of transparency of PV cells. Additionally, CRI can also be calculated using a specific algorithm from either Transmittance or Reflectance values, given specific information on the colour-neutrality (or not) of the completed TPV devices. From these measurements it is also possible to make the photon balance check that serves to avoid any overestimation on the EQE (and J_{sc}) of TPV devices when calculating their PCE using a solar simulator.

4-point probe resistivity

4-point probe resistivity measurements are a type of electrical measurement that uses four leads that are placed longitudinally at a given distance from one another (typically few mm). Typically, the two extremal probes are interconnected measuring current across, while the two centred probes are responsible for establishing a potential in the thin film that is under assessment. In this thesis, 4-point measurements were performed to assess the sheet resistance of different layers involved in device fabrication. More specifically it has been routinely used to check the quality of ITO and FTO electrical contacts used in the fabrication of transparent solar cells reported in the article compendium in Chapter 3.

Spectral Response measurements

Spectral response characterization of complete TPV devices was performed in order extract the External Quantum Efficiency (EQE) of the devices. The EQE measurements were conducted with a Bentham PVE300 spectral response system in the 300-1500 nm range calibrated with Si and Ge reference photodiodes. This tool allowed to calculate the electrical response of the TPV devices at different wavelengths as well as to obtain the EQE under light and electrical biases. Electrical bias was applied using a Keithley 2400 SMU.

Current density-voltage characteristics (J–V)

J-V characteristics measurements were carried-out on complete devices in order to characterize their optoelectronic properties, both under illumination and in dark conditions. As illuminant, a Sun 3000 AAA solar simulator from Abet Technology was used. Callibration of the source was done using a reference Si solar cell. Electrical input/output probing was performed using a Keithley 2400 SMU. Electrical contacts were performed on a four-probe configuration. In this thesis, this has been the main optoelectronic characterisation technique used to assess the performance of the complete TPV device prototypes, allowing for an accurate calculation of the power conversion efficiency of the transparent solar cells.

3 - Chapter 3: Article compendium

This thesis is compounded by a set of research publications in specialized scientific journals, with Alex López García as first author. These will serve as the foundation for this thesis having each article a dedicated subchapter. All three articles presented have been published in Q1 high impact factor journals under the following titles:

1. **A.J. Lopez-Garcia**, A. Bauer, R. Fonoll Rubio, D. Payno, Z. Jehl Li-Kao, S. Kazim, D. Hariskos, V. Izquierdo-Roca, E. Saucedo, A. Pérez-Rodríguez, "UV-Selective Optically Transparent Zn(O,S)-based Solar Cells", ***Sol. RRL***, 4, 11, 2000470, 2020, doi: 10.1002/solr.202000470 ; IMPACT FACTOR (IF): 9.173
2. **A.J. Lopez-Garcia**, O. Blazquez, C. Voz, J. Puigdollers, V. Izquierdo-Roca, A. Pérez-Rodríguez, "Ultrathin Wide-Bandgap a-Si:H-based Solar Cells for Transparent Photovoltaic Applications", ***Sol. RRL***, 6, 1, 2100909, 2022, doi: 10.1002/solr.202100909 IMPACT FACTOR (IF): 9.173
3. **A.J. Lopez-Garcia**, J.M. Asensi, C. Voz, J. Puigdollers, V. Izquierdo-Roca, A. Pérez-Rodríguez, "Ultrathin a-Si:H/oxide transparent solar cells exhibiting UV-blue selective-like absorption**",** ***Sol. RRL***, 7, 7, 2200928, 2023, doi: 10.1002/solr.202200928 ; IMPACT FACTOR (IF): 9.173

3.1 - Introduction and context to research work and related publications

In this sub-section a broad introduction and context to the related experiments that led to the different publications that compose the body work of this thesis is presented, summarizing the research carried out in the framework of this thesis during the 2018-2022 period. This thesis has been structured as an article compendium stemming from the work developed in the mentioned period that resulted in the publication of three scientific articles as first author.

As mentioned in the thesis objectives, the activities were performed in the frame of a pilot Horizon 2020 European project (Tech4Win)[34], carrying out the experiments mainly at the SEMS group facilities at IREC or at the cleanroom facilities at UPC, with the following objective: generate and develop disruptive PV applications in the form of transparent solar windows for BIPV as the main focus, explore their limitations and propose novel architectures and synthesis routes that maximize the efficiency and visual and aesthetic properties.

The three articles that compose the thesis, which are presented in the following lines, are reprinted with the following permissions and license: Permission conveyed through Copyright Clearance Center. Republished with permission of © John Wiley and Sons, from Solar RRL, UV-Selective Optically Transparent Zn(O,S)-Based Solar Cells, with license number 5574791216763; Republished with permission © John Wiley and Sons, from Solar RRL, Ultrathin Wide-Bandgap a-Si:H-Based Solar Cells for Transparent Photovoltaic Applications, with license number 5574791146400; Republished with permission of © John Wiley and Sons, from Solar RRL, Ultrathin a-Si:H/Oxide Transparent Solar Cells Exhibiting UV-Blue Selective-Like Absorption, with license number 5574791011397.

As an introduction to the article compendium and to present the workflow and context of the experimental development throughout the doctoral period, some experiments and results are presented in the following. It is recommended to jump from the introduction parts to the corresponding

research article to get the full context of the work carried out throughout the doctoral period.

The work in the initial periods revolved around the synthesis, characterisation and development of ZnO films to be used as absorber material, to fabricate multifunctional UV-selective TPV devices that present high UV filtering. The idea was to try and fabricate TPV devices that resembled the SoA at the time of these experiments, which basically were exploring the use of ZnO as a UV-selective absorber due to its wide bandgap of 3.2 eV. Besides, the point of exploring oxide materials is that these materials poses wide bandgaps typically above 3 eV, that renders the materials transparent to visible light preserving a high colour neutrality. The initial proposed architecture consisted in using a p-n architecture using ZnO as the n-type material and NiO as the p-type material. The electrical contacts in the final devices were selected to be FTO, which is a commercial substrate (FTO coated on SLG substrate) that is used as a standard substrate in different PV technologies, due to its chemical stability and very high transparency and colour neutrality while still presenting quite low resistivity (with sheet resistances around R_{sh}=8-15 ohmsq^{-1}). FTO worked as back-contact for the TPV devices. As front-contact electrode the choice was ITO, which could be routinely deposited by DC-Pulsed Confocal Magnetron Sputtering at the SEMS laboratory, presenting typical values of R_{sh}=30-100 ohmsq^{-1}, which are assumable given the geometry and active area of the TPV devices, with areas below 0.1 cm^2, enabling its use while neglecting important losses in series resistance. To deposit the ZnO absorber layers, again DC-Pulsed Magnetron Confocal Sputtering was chosen as the standard tool at this stage, while NiO could be deposited routinely by either thermal or e-beam evaporation, being the later the technique that yielded higher reproducibility and controllability of the deposition process.

ZnO and NiO were the first films to be fabricated. For their optical characterization they were deposited on SLG substrates. The first experiments consisted in performing different post-deposition treatments (PDTs) in either air or argon (Ar) atmospheres, varying the process temperature from 200 ºC to 400 ºC and comparing the results with the as-deposited or pristine samples. For this study, the film thickness in both cases was set to 50 nm. The idea was to explore the effect of these PDTs

and see how these could tune different electrical and optical properties of the materials, with the main focus on controlling its optical properties and studying its effect on UV absorption and AVT, which were target parameters for the final TPV devices.

For these experiments, characterization was done using UV-VIS spectrophotometry and Raman spectroscopy, served to quantify AVT and to assess effective material deposition and crystallinity (in a qualitative manner). It was observed that thermally evaporated NiO films were the limiting factor for high AVT values, albeit being in an acceptable range. However, AVT could be increased due to the effect of the PDT, as annealing up to 400 ºC in an oxygen-containing atmosphere led to improved AVT as compared with the pristine NiO films. Apparent crystallinity improved also with increasing annealing temperature and regardless of the PDT atmosphere used, as noticed in the reduction of the NiO associated Raman peak width.

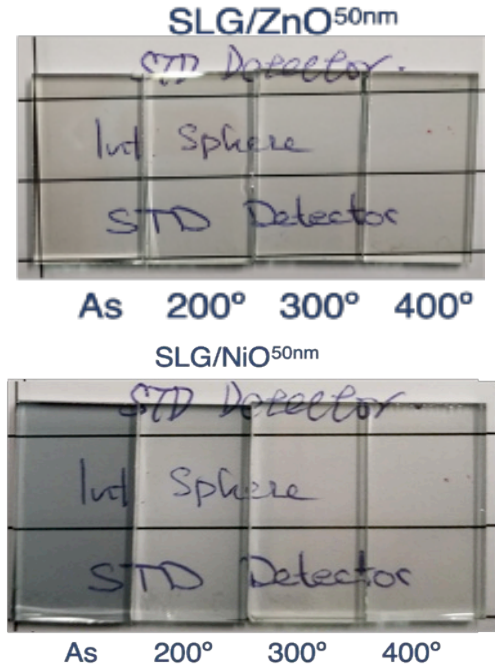

Figure 17: Optical images of oxide layers as-deposited and after post-deposition annealing treatments: (top) ZnO (bottom) NiO, on SLG substrate.

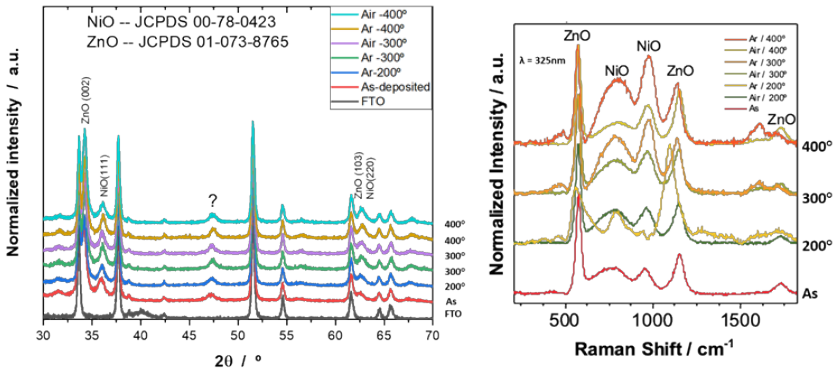

Figure 18: GIXRD and Raman spectroscopy of the stack FTO/ZnO(50 nm)/NiO(50 nm) to assess crystallinity and compare with different annealing processes.

With these aspects in mind, the first stacks of SLG/FTO/ZnO/NiO were synthesised (Figure 17), as the natural continuity leading to complete TPV devices. The experiment consisted in the PDT effect on the complete stack. Several samples were fabricated and then compared. The set consisted on an as-deposited sample versus samples annealed in air or Ar at 200 ºC, 300 ºC and 400 ºC. These samples were characterised by optical spectrophotometry, GIXRD and Raman spectroscopy. The results from this characterisation are presented in Figure 18. In Figure 18 (left), the GIXRD diffractogram is shown. The peaks could effectively be traced to the JCPDS cards corresponding to ZnO and NiO, with no apparent change in peak position or width after the PDTs. The most intense peak was associated with the 002 plane of ZnO (wurtzite) showing also the presence of the 103 plane, while NiO main peak was associated to the 111 plane corresponding to cubic NiO. In a similar manner, Raman spectroscopy using UV excitation with 325 nm wavelength confirmed again the presence of NiO and ZnO. In this case, the signal associated to the NiO seemed to evolve with the PDT treatment, suggesting an increase in apparent crystallinity of the films which came in contrast with the diffractogram. Raman spectroscopy using this excitation wavelength is more surface-sensitive than GIXRD, so this could be a possible explanation of the discrepancy.

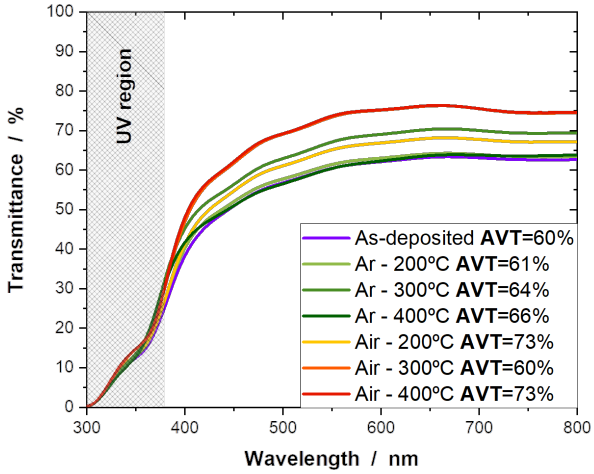

Figure 19: Comparison of transmittance data of Glass/FTO/ZnO(50nm)/NiO(50nm) structures with different post-deposition annealing treatments. AVT experimental values are shown in the inset.

Looking into the transmittance spectra obtained from optical spectroscopy, a notable evolution could be observed, as increasing temperature generally led to higher AVT values (Figure 19). Nonetheless, even for the as-deposited stack, the AVT was higher than 60%, which was already high enough to avoid performing any PDT in order to reach the desired target values. However, looking into the UV region in the transmittance spectra, it could be observed that there was still a quite high UV transmittance, out of the targeted range.

Based on these results the next experiments targeted an increase in the ZnO absorber thickness so that higher UV absorption could be achieved while still having high AVT. The PDTs were dropped from further experiments as they were deemed as an extra step that did not lead to significant improvement in the targeted parameters. Additionally, NiO was to be explored using e-beam evaporation instead of thermal evaporation, as e-beam evaporation yielded films with very high transparency and colour neutrality in a very reproducible manner, in contrast with thermally evaporated NiO films, as discussed.

The next experiment consisted on fabricating a TPV prototype device and comparing two different ZnO thicknesses and perform its optoelectronic characterisation. The two devices had the following structure:

- Glass/FTO/NiO^{50nm}/ZnO^{150nm}/ITO
- Glass/FTO/NiO^{50nm}/ZnO^{50nm}/ITO

After sample fabrication, J-V characteristics in dark conditions were measured to confirm the presence of rectification which would indicate diode formation. The characteristics are plotted in Figure 20.

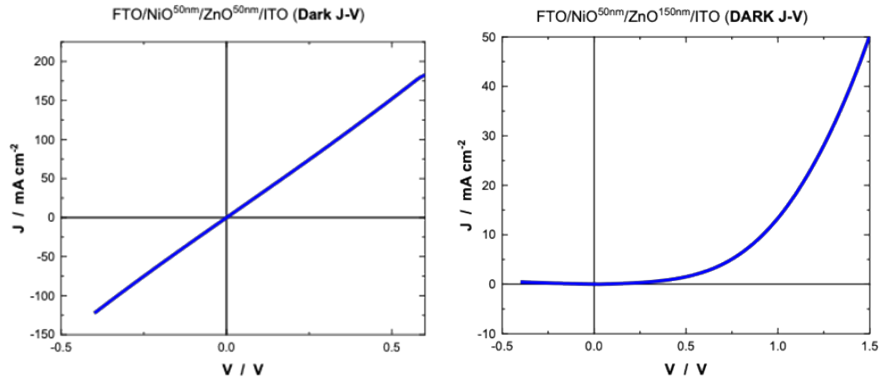

Figure 20: Dark J-V curves of two devices with same stack and different thickness. (right) Device with ZnO 50nm layer. (left) Same stack with 150nm of ZnO.

As observed in the figure, the device with a 50 nm ZnO layer showed linear behaviour, indicating that no rectification happened, so the junction did not effectively behave as a diode and only showed ohmic behaviour. However, the device with a 150 nm ZnO film displayed rectification, suggesting that an increased thickness was leading to the formation of a p-n junction, so it could be possible that the device could effectively work as a TPV device when illuminated with a light source. This result coupled with the optical characterisation was strongly leading to explore devices with higher ZnO film thickness.

The next steps consisted in fabricating FTO/ZnO/NiO stacks with thermally evaporated 50 nm NiO films and making variations in the thickness of ZnO: 100 nm, 150 nm, 190 nm, 250 nm and 400 nm. After sample preparation, they were optically characterised. The results are shown in Figure 21. Based on the spectra, it can be seen that the AVT

values remain approximately equal regardless of ZnO thickness. However, the UV absorption was dramatically increased, suggesting that the approach was effective, and didn't show any trade-off in the optical features of the TPV devices. The stack with ZnO showed the highest UV absorption, being able to absorb almost all UV photons from 300 nm to 380 nm.

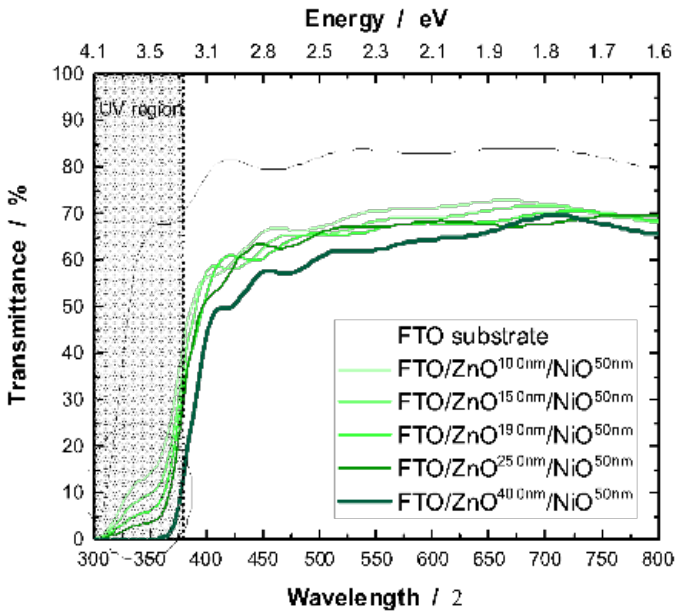

Figure 21: Transmittance spectra of ZnO/NiO devices fabricated with NiO thickness fixed at 50 nm and different thicknesses for the ZnO layer (from 100nm to 400nm). The transmittance of the SLG/FTO substrate is presented for comparison.

With these samples, J-V characteristics under illumination were measured on full TPV stacks including the ITO front-contact. However, no PV effect was obtained in any case. Rectifying diodes were obtained for ZnO absorber thickness between 100nm and 400nm. The devices are also sensitive to the UV radiation, working as ultraviolet photodetectors and filters. These evidences indicated that the devices were highly efficient UV filters with high visible transparency, but with no PV performance. Looking into the SoA at the time, it is to be noted that only a handful of articles showed a measurable PV effect, with the highest reported PCE at 0.5%.

As the plan already established the exploration of $ZnO_{1-x}S_x$ films as a potentially better absorber for UV-selective TPV due to the possibility of lowering the bandgap in comparison to pure ZnO and matching it to the spectral UV onset in the AM1.5G spectrum, the main efforts were trespassed towards $ZnO_{1-x}S_x$ film synthesis and characterisation, following with complete $ZnO_{1-x}S_x$-based TPV devices. Due to the lack of a deposition technique that could be used to synthesise this material at the time of the experiments, the synthesis was out-sourced to another laboratory, beginning a international collaboration with ZSW, located at Stuttgart, Germany. They had deposition techniques that were compatible and had already synthesised this material, which has been extensively used as a buffer layer in CIGS technology, fabricating films with thickness below 50 nm. For this work experiments were planned and coordinated at IREC while the material synthesis was performed at ZSW and samples were then returned to IREC to either characterise or fabricate functional TPV devices.

The deposition technique used at ZSW was reactive sputtering using an RF power source. The initial experiment consisted on the deposition of $ZnO_{1-x}S_x$ films across the whole compositional range and to make optical characterisation in order to see whether the experimental values matched the theoretical predictions that established that a bandgap bowing occurs in the mid-compositional range, leading to bandgaps as low as 2.7 eV. At the time, an ALD deposition system was expected to be installed at IREC's facilities, so that the same experiments and the continuation of them could be fully controlled and made on-site. Additionally, ALD is a very promising technique for the synthesis of this material as sulfur-oxygen content can be introduced layer-by-layer thus giving unparalleled composition control with high conformality as compared with the sputtering technique.

First samples were prepared in ZSW with three different target compositions with sulfur relative content of x = S/(S+O) = 0.3, 0.6, 0.8. For x=0.3, 0.6 the samples were prepared by RF sputtering of mixed ZnO/ZnS targets, while reactive sputtering of a pure ZnS target in a reactive atmosphere consisting of a specific mix of Ar/O_2 was used for x=0.8. In this case, two different nominal thicknesses were targeted: 100

nm and 250 nm. Deposition was done on two different substrate types which were sent by IREC:

- Glass/FTO (for characterization and device fabrication)
- Glass/FTO/NiO (for device fabrication)

The substrates were pre-heated up to 250 ºC before and during deposition.

After sample fabrication, they were immediately shipped to IREC facilities for characterisation. Raman spectroscopy and Optical spectrophotometry was performed on all samples, the former to confirm the formation of the mixed crystals without phase segregation and empirically calculate the relative sulfur content, and the latter to calculate the AVT and to estimate the bandgap for each composition.

To confirm the formation of $ZnO_{1-x}S_x$ mixed crystals and calculate the relative sulfur content empirically. Raman spectroscopy was performed with a monochromatic 325 nm UV excitation wavelength. The Raman spectra from $ZnO_{1-x}S_x$ present a 2-mode behaviour that is a characteristic of the mixed crystal, with the presence of a ZnO-like peak located at 574 cm^{-1} and a ZnS-like peak located at 351 cm^{-1}. The Raman shift for the ZnO peak presents a linear dependency with the x=S/(S+O) compositional ratio, while the ZnS-like shift is not affected by the relative composition of the films. These features allow for a quantitative assessment of the S/(S+O) compositional ratio in the films from the analysis of the ZnO-like peak position based on a methodology developed at IREC[23,35]. This allows to experimentally confirm that the targeted compositional values x=0.3, 0.6, 0.8 were achieved during deposition. Figure 22 shows the spectra for the six samples that compose the sample set. In the spectra the characteristic peaks for the $ZnO_{1-x}S_x$ mixed crystals are present, confirming that indeed no phase segregation occurred during synthesis. The ZnS-like peak is located around 348 cm^{-1} for the samples with x=0.6, 0.8 (close to the wavevector reported for the ZnS LO peak), while it could not be observed for the sample with x=0.3, possibly due to the low sulfur content. The ZnO-like peak is observed at 434, 473, 535 cm^{-1} for samples with x=0.8, 0.6, 0.3, respectively. This shift towards the reported ZnO peak indicated an increase of the oxygen content with respect to sulfur content in the $ZnO_{1-x}S_x$ structure, and is coherent with the targeted compositional values. In addition, there is a band located between 160-225 cm^{-1}, with a peak at 193

cm^{-1}. The relative intensity of this peak is maximal in the case of the x=0.6 sample. This band has been identified with fundamental overtones out of the Γ point of the Brillouin zone, which are activated for the induced intrinsic disorder generated in the $ZnO_{1-x}S_x$ mixed crystal. These measurements confirmed that it was indeed possible to deposit $ZnO_{1-x}S_x$ through the whole compositional range and without any phase segregation using the sputtering equipment at ZSW.

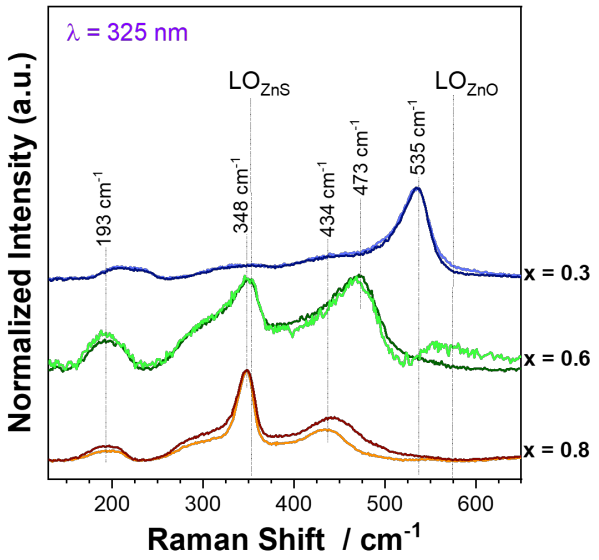

Figure 22: Raman spectra of Zn(O,S) samples grown on FTO with three different compositions and two thicknesses (100nm in light colour and 250nm in dark color).

From the optical spectrophotometry measurements transmittance spectra are generated. Resulting transmittance spectra of the SLG/FTO/$ZnO_{1-x}S_x$ samples are presented in Figure 23 and compared with the standalone SLG/FTO substrate for reference. From these spectra the AVT values were calculated. In every case, as expected, the AVT values are very high due to the wide bandgap of the materials, having values higher than 75%, making the material and adequate candidate for a TPV absorber material. The values extracted from the calculation are summarised in Table 1.

From the transmittance spectra, and having information on the material thickness, it is possible to have a rough estimation of the bandgap of the films. For this Tauc plots are presented in Figure 24. The leftmost plot

corresponds to the thicker films (nominal target 250 nm) with different composition while the rightmost graph corresponds to the thinner films (nominal target of 100 nm). Results from optical characterisation are summarised in Table 1.

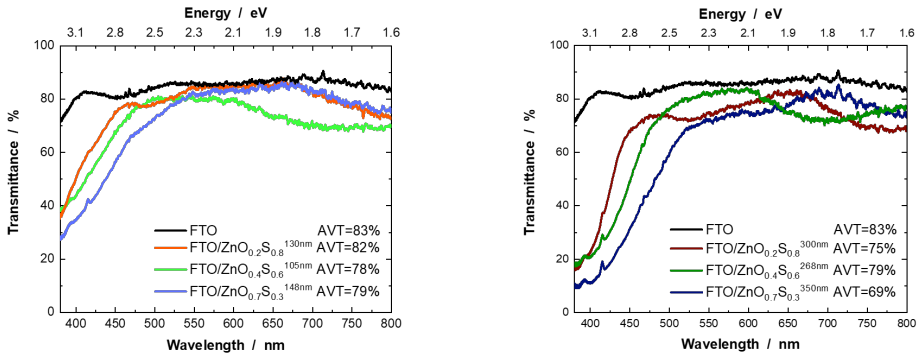

Figure 23: Transmittance spectra of FTO/$ZnO_{1-x}S_x$ samples with different thickness and composition. FTO substrate transmittance spectrum is shown as reference and maximum AVT achievable.

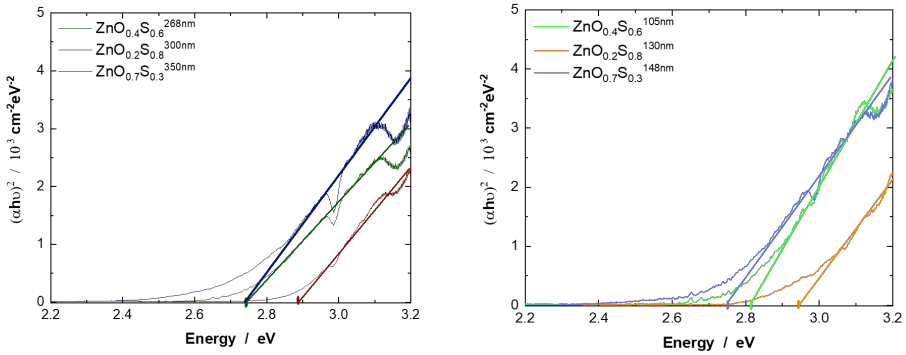

Figure 24: Tauc's plots for the three different compositions and two thicknesses studied. These results show that bandgap is greatly reduced as compared with ZnO, showing bandgap below 3 eV in all cases.

For all stoichiometries, with nominal thickness of 100 nm, the films are almost completely transparent and colourless. The FTO which acts as substrate for these samples and also as electrical back-contact for the complete TPV devices is shown in the figures as reference, and its AVT is also calculated.

Table 1: Summary of estimated bandgap values resulting from Tauc's plot method for each sample and composition.

Sample	Measured thickness / nm	AVT / %	E_g / eV
FTO/ZnO$_{0.2}$S$_{0.8}$	130	82	2.9
	300	75	2.9
FTO/ZnO$_{0.4}$S$_{0.6}$	105	78	2.8
	268	79	2.8
FTO/ZnO$_{0.7}$S$_{0.3}$	148	79	2.7
	350	69	2.7

Looking at the thinner samples, the lowest AVT value corresponds to the relative sulfur content of x=0.6, with AVT = 79%. As commented in the Introduction section, the AVT is weighted respect to the human eye's photopic response, which is modelled as a gaussian curve centred around the 555 nm wavelength. Looking into the transmittance spectra shown in Figure 24 for the three samples, it can be seen that the spectra almost overlap in such wavelength range and thus present quite similar values, yielding little differences in the AVT value. The most notable variation is in the region associated to the absorption onset, which is determined by the bandgap, which varies with relative composition. Similar trends are observed for the thicker samples in the three cases. The most notable variations come in the material absorption onset while in the "AVT region" they have a similar profile. However, in this case the AVT values differ in a higher grade. The sample with x=0.6 presents the highest AVT value at 75% while the sample with x=0.3 presents the lowest AVT of all the set, at 69%. Additionally, this sample presented a notable yellowish colour, which could possibly be due to defects in the structure. Nonetheless, all the AVT in the set are well above 69%, meaning that the materials are potential candidates for UV-selective TPV devices. Again, this is expected and attributed to the wide bandgap nature of the materials.

From this point, the continuation of the experimental work consisted in the fabrication of complete TPV devices using $ZnO_{1-x}S_x$ mixed crystals in substitution of pure ZnO. The clear advantage is that $ZnO_{1-x}S_x$ presents a lower bandgap, with a minimum around 2.7 eV, that perfectly matches the UV spectral onset for the standard AM1.5G illuminant. This results in the possibility of obtaining potentially higher photocurrents, as a greater portion of the target UV range can be effectively absorbed in contrast with

pure ZnO, while still having excellent optical properties (i.e. high AVT and colour-neutrality).

Figure 25: Pictures presenting complete $ZnO_{1-x}S_x$ devices with different sulfur relative content.

Two types of structure were fabricated, either $ZnO_{1-x}S_x$/NiO heterojunctions or an architecture that was potentially better given the fact that the $ZnO_{1-x}S_x$ films were undoped and highly resistive (an indication of them being possibly intrinsic materials). The architecture selected was ETL/Absorber/HTL, with charge-selective filters for each type of carrier. Given that the samples were quite resistive, the choice was to work with a thinner $ZnO_{1-x}S_x$ film as absorber material.

This experiment led to the results that are presented and discussed in the first research article that is the first of the article compendium. The reader is referred to Chapter 3.2. for the detailed results and discussion.

After the consecution of this achievements, it was demonstrated that $ZnO_{1-x}S_x$-based devices showed great promise as the leading material for oxide-based UV-selective TPV. Hence, the original idea was to continue with this approach and work intensively on the matter. An ALD deposition system was purchased to be dedicated to the $ZnO_{1-x}S_x$ material synthesis. The collaboration with ZSW could not be continued due to their needs to use the sputtering equipment with exclusive dedication to their research

projects. However, at the time, the COVID-19 epidemic started, resulting in a complete halt in the fabrication of the ALD system and to huge delays in logistics that eliminated the possibility of continuing on this promising topic, which was deemed to be central in the doctoral thesis. The ALD system could not be implemented in time, so an alternative mitigation strategy was devised with the same objectives that aligned with the thesis. As an alternative to working with such wide bandgap materials with a matched onset with the UV spectral range it was thought that it would still be possible to fabricate UV-selective TPV devices using inorganic materials and still working mostly on oxide materials. The key idea was to utilize materials with lower bandgaps, even lying in the visible range, but making these absorbers ultrathin, of just few nanometres. This approach presented evident trade-offs, as reducing absorber thickness leads to less absorption and thus less photocarrier generation. Additionally, the bandgap lying in the visible range inevitably imposes a limit on colour neutrality and transparency. However, with careful engineering it was thought that the idea might just work. As a note, it is worth mentioning that SoA oxide-based devices had PCE values around 0.5% and that devices with PCE>2 % with AVT>30% could still be a potentially valuable approach with acceptable implementation in practical TPV applications, albeit having more restrictive practical implementation to some specific case.

With this in mind, the chosen absorber material candidate was intrinsic a-Si:H, which is a material that had already jumped from research to industrial scale a couple of decades before, so it was a mature technology and material deposition with some techniques allowed for nanometric control of the film thickness and allowed for the deposition of ultrathin films. Stemming from the experiments done so far, the idea was to combine the present knowledge and try to implement a-Si:H into mostly oxide-based architectures. There was basically no previous research literature applied to TPV devices, with some sparse articles exploring the application of p-i-n a-Si:H homojunctions with transparent contacts. The thickness of the absorber coupled with the parasitic absorption occurring at the CTLs greatly limited the AVT of the final devices to values below 15%, thus eliminating the possibility of implementation as TPV applications. Simultaneously, other group working on UV-selective TPV devices based on pure oxide devices had published an article exploring this possibility[36].

The coming experiments revolved about replicating a similar approach to the one presented in ref. [36] and to delve into the working mechanisms of these devices, which from this point of view, behaved differently from the discussion presented in the referenced work. It also consisted on simultaneously exploring and implementing suitable CTLs with high transparency and low parasitic absorption while depositing ultrathin a-Si:H films and characterising them and finally fabricate complete TPV device prototypes that were also optoelectronically characterised.

As a first approach and based on the prior findings from this thesis the idea was to use ZnO as a base ETL and explore different HTLs, starting with NiO and also exploring MoO_3 and V_2O_5 as viable candidates, which had been successfully implemented as hole selective contacts in different PV technologies. The absorber thickness (nominal) was set to 15 nm, as it had already been reported to present adequate transparency. The ZnO ETL was set to 50 nm and was deposited by sputtering, while the three different HTLs were initially deposited by thermal evaporation. In this case NiO deposited by thermal evaporation resulted in ohmic behaviour, showing no PV effect. As for MoO_3 and V_2O_5, the results were promising, as J-V characteristics (Figure 26) confirmed a PV effect for the following structures:

- SLG/FTO/ZnO(50 nm)/a-Si:H(15 nm)/MoO_3 (20nm)/ITO
- SLG/FTO/ZnO(50 nm)/a-Si:H(15 nm)/V_2O_5 (15nm)/ITO

It can be observed that the J-V characteristics under AM1.5G illumination of the device with a V_2O_5 HTL had a non-ideal curve profile, and although showing PV effect the shape was an indicative of the presence of a barrier that resulted in this poor performance. Using a MoO_3 HTL however resulted in a more conventional shape, confirming the formation of a diode and having an exponential shape. It also presented a higher V_{OC} (310 mV) than for V_2O_5 (260 mV).

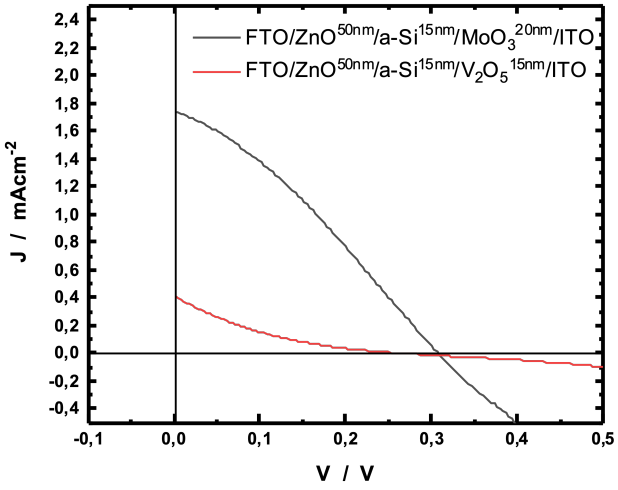

Figure 26: J-V characteristics, under AM1.5G illumination, of two different a-Si:H/oxide based devices using a MoO3 HTL and a V2O5 HTL.

From these initial results it was decided to carry on a revised experiment wherein MoO_3 was the HTL to be studied, and a set of devices was generated in order to study the impact of ZnO (and its thickness) as ETL and the impact of MoO_3 (and its thickness) as HTL, also generating devices with an ETL and no HTL and with a HTL and no ETL, in order to compare and confirm that the most promising device concept relied on the use of both charge selective contacts. In this experiment, two different thicknesses of a-Si:H were studied, which served to assess the limits and compromise in the AVT and PCE trade-off which was found for these ultrathin a-Si:H/oxide devices, which stems from the use of a material with bandgap within the energy range of visible light. The results of this work resulted in the second scientific article that forms the article compendium of this thesis. The details, discussion and conclusions of this experiment can be read in this article.

After the experiments performed therein, the decision was to work on the optimization of the selective contacts and to explore more thickness variations of the ultrathin a-Si:H absorber. The ZnO ETL deposited by sputtering was changed by ALD-deposited AZO. TPV devices were made using AZO as the new ETL while MoO_3 was kept as the HTL. Two different absorber thicknesses of 8 nm and 30 nm were studied. Given the

prior results discussed in the second scientific article, the idea was to go to the technological limits of the deposition systems and to see if it was possible to make a TPV device with 8 nm (around roughly 80 atoms thick layer of a-Si:H) and to compare the trade-off in AVT and PCE, comparing to a thicker 30 nm, which was already confirmed as a suitable candidate for some TPV applications due to its AVT>30%. The feasibility of a device with an 8 nm film would result in the possibility of tailoring the TPV properties from high PCE and lower AVT for the thicker films towards higher AVT with the con of reducing PCE. However, this aspect is a potential feature for TPV applications, as the same technology can be applied and without any change in materials (and possibly deposition techniques) the device properties can be adapted to some specific TPV applications that perhaps might not need to have a very high PCE but critically need to excel in colour-neutrality and transparency, while the thicker absorbers could be left for more PCE-reliant TPV applications.

For this experiments, the CTLs would remain fixed and all devices would be fabricated in parallel, to have a more precise and fair comparison of the mentioned outcomes. To further complete the study, a complete optical study of both a-Si:H films (8 nm, 30 nm) was carried out relying on optical spectrophotometry and Photothermal Deflection Spectroscopy (PDS), which allowed for a detailed characterisation, obtaining the Urbach energy of these ultrathin films and demonstrating that even with the thinnest film, at 8 nm, the optical properties of the material behaved in a classical manner without any quantum effects, that typically arise at the nanoscale or sub-nanoscale. The results from these experiments were condensed into the third and final scientific article that conforms the article compendium of this thesis. In the third article presented in Section 3.3 the reader can find the in-depth details of the experiments, the results and discussion of the findings and some final remarks.

As a brief summary, this section has given some introductory ideas and context into results of intermediate experiments that give the coherent line of work that led to the realisation of the thesis objectives. In the next sections the article compendium is presented, followed by the final conclusions and remarks stemming from the work done in the doctoral period.

3.2 – First research article

Solar RRL
www.solar-rrl.com

UV-Selective Optically Transparent Zn(O,S)-Based Solar Cells

Alex J. Lopez-Garcia, Andreas Bauer, Robert Fonoll Rubio, David Payno, Zacharie Jehl Li-Kao, Samrana Kazim, Dimitrios Hariskos, Victor Izquierdo-Roca, Edgardo Saucedo, and Alejandro Pérez-Rodríguez*

This work reports experimental evidence of a photovoltaic effect in transparent UV-selective Zn(O,S)-based heterojunctions. Zn(O,S) has a strong interest for the development of UV-selective solar cells with high transparency in the visible region, required for the development of nonintrusive building-integrated photovoltaic (BIPV) elements as transparent solar windows and glass-based solar façades. By anion alloying, Zn(O,S) mixed crystal absorbers can be fabricated with different sulfur content across the whole compositional range. This allows adjustment of the bandgap of the absorbers in the 2.7–2.9 eV region, maximizing absorption in the UV, while keeping a high level of transparency. Zn(O,S) alloys with composition corresponding to S/(S + O) content ratios of 0.6 are successfully grown by sputtering deposition, and first glass/FTO/NiO/Zn(O,S)/ITO device prototypes are produced. The resulting devices present an average visible transmittance (AVT) of 75% and present photovoltaic effect. By introducing a thin C_{60} film as electron transport layer (ETL), charge extraction is enhanced, and devices show an efficiency of 0.5% and an AVT > 69%. The transparency of these devices can potentially allow for their ubiquitous installation in glazing systems as part of nonintrusive BIPV elements or to power Internet of Things (IoT) devices and sensors as an integrated transparent component.

Building-integrated photovoltaic (BIPV), which nowadays represents about 2% of the PV market, is an area that has the aim of easing local energy production by providing buildings with both conventional and novel ubiquitous and efficient PV devices, with the ideal goal of reaching net-zero energy consumption buildings (nZEB).[1] These applications result in an increased interest in obtaining fully transparent PV (TPV) devices in the visible range, while they can selectively absorb UV and/or IR wavelengths.[2] Such devices present a high potential for integration in glazing systems and smart windows as nonintrusive BIPV elements. Other novel applications include devices that could be integrated as functional active harvesting components to power optoelectronic devices such as sensors, electrochromic windows, or Internet of Things (IoT) devices.[3,4] An interesting strategy for the development of these devices is the combination of UV-selective wide bandgap inorganic solar cells and IR-selective organic solar cells in a hybrid tandem-like structure.[5] Maximizing UV absorption in the UV-selective top cells

A. J. Lopez-Garcia, R. Fonoll Rubio, Dr. Z. Jehl Li-Kao, Dr. V. Izquierdo-Roca, Prof. A. Pérez-Rodríguez
Solar Energy Materials and Systems
Institut de Recerca en Energia de Catalunya (IREC)
Jardins de les Dones de Negre, 1, 2ª pl, Sant Adrià del Besòs 08930, Barcelona, Spain
E-mail: alopez@irec.cat

Dr. A. Bauer, Dr. D. Hariskos
Photovoltaik Materialforschung
Zentrum für Sonnenenergie- und Wasserstoff-Forschung
Baden-Württemberg
Meitnerstr. 1, Stuttgart 70563, Germany

D. Payno, Dr. S. Kazim
BCMaterials
Basque Center for Materials, Applications and Nanostructures
Bld. Martina Casiano, UPV/EHU Science Park, Barrio Sarriena s/n
Leioa 48940, Spain

The ORCID identification number(s) for the author(s) of this article can be found under https://doi.org/10.1002/solr.202000470.

DOI: 10.1002/solr.202000470

Dr. S. Kazim
IKERBASQUE
Basque Foundation for Science
Bilbao 48013, Spain

Prof. E. Saucedo
Photovoltaic Group
Department Enginyeria Electrònica
Universitat Politècnica Catalunya
c/ Jordi Girona 3-1, Barcelona 08034, Spain

Prof. A. Pérez-Rodríguez
IN2UB
Departament d'Enginyeria Electrònica i Biomèdica
Universitat de Barcelona
Carrer de Martí i Franquès 1, Barcelona 08028, Spain

© 2020 Wiley-VCH GmbH

has an additional interest, as this allows preventing UV-induced degradation of the subjacent IR-selective organic device in the cell structure. Wavelength-selective TPV applications can thus expand the applications in the PV industry, especially within the BIPV sector.

Focusing on UV-selective TPV devices, oxide materials are very interesting for the development of these devices because they are stable, inexpensive, abundant, easy to process, and typically nontoxic. Among them, ZnO is an interesting material which has been intensively studied for many decades. It presents high absorption coefficient ($\alpha(\lambda) > 10^4\ cm^{-1}$ for $\lambda < 390$ nm) and a direct energy bandgap of 3.37 eV.[6,7] To date, state-of-the art UV-selective solar cells are mainly based on the use of ZnO as the absorber material.[8–13]

However, there are some important caveats that limit the use of ZnO for such solar cells. First, related to polarity and charge transport properties, being the fact of lack of bipolarity (i.e., p-type ZnO) which prevents the fabrication of homojunctions in conventional p–n configuration and also the synthesis of p-ZnO as absorber.[6,7,14] ZnO, if undoped, presents mild n-type character and is highly resistive, presenting poor transport properties such as low carrier mobility. Absorbers with poor carrier transport, for example, a-Si, have thus resorted to alternative device configurations in which the absorber is sandwiched between two carrier-selective contacts, known as charge transport layers (CTLs).[15] This device architecture has also been widely used in perovskite systems, where the intrinsic absorber typically presents excellent transport properties.[16–18] It is thus relevant to study such architectures incorporating CTLs, which can be both organic or inorganic.

Second, and most important for UV-selective solar cells, the bandgap of ZnO (3.37 eV) is much higher than the UV spectral onset at around 2.7 eV. This implies that photons with energies below the bandgap energy of ZnO and down to the 2.7 eV onset will not be absorbed, resulting in a lower range of photon absorption in the UV spectral region and consequently in inherent efficiency losses. This is confirmed by the dependence of the efficiency on the absorber bandgap,[19] also simulated in this report using SCAPS.[20] The results of the simulation are presented in Figure S1, Supporting Information. As shown in this figure, using ZnO as absorber, the maximum efficiency (AM1.5G, $100\ mW\ cm^{-2}$) of the device is limited at values below 0.3%, whereas decreasing the bandgap of the absorber down to 2.7 eV results in an increase in the efficiency limit to values slightly above 4%.

Hence, it is important to find a material that presents both high absorption in the UV and a bandgap closer to the UV spectral onset. None of the binary oxides fulfil this bandgap requirement. However, by anion alloying ZnO with sulfur (S), it is possible to fabricate Zn(O,S) mixed crystals. Zn(O,S) presents a bandgap energy bowing with a reported minimum value at 2.7 eV in the mid-compositional range.[21–24] By exploring intermediate sulfur/oxygen composition, the bandgap can be reduced to values closer to the visible region while still absorbing exclusively in the UV region, allowing the development of devices with colorless visible transparency. In this work, it is shown that it is indeed possible to fabricate Zn(O,S) layers with well-controlled $S/(S+O)$ relative content that can be used for the development of UV-selective transparent devices presenting a more optimal spectral match with the UV region and showing PV effect using different device configurations. Optical and electrical properties of the fabricated absorbers and devices are analyzed and discussed herein.

$ZnO_{1-x}S_x$ layers have been grown on glass/FTO and glass/FTO/NiO stacks with a target S relative content corresponding to $x = 0.6$ and a thickness of 105 nm. Layers on glass/FTO/NiO were subsequently used for the fabrication of planar heterojunction solar cells with structures Glass/FTO/NiO/Zn(O,S)/ITO and glass/FTO/NiO/Zn(O,S)/C_{60}/BCP/ITO (**Figure 1**). NiO was used as a hole-selective contact, C_{60} was used as an electron transport layer (ETL) in conjunction with a bathocuproine (BCP) nanometric layer acting as hole-blocking layer, and In_2O_3:SnO_2 (ITO) acted as the transparent front-contact of the solar cell. The fabrication process is described in detail in the Experimental Section. Optical and electrical characterization has been done on completed devices while Raman spectroscopy measurements were carried out on Glass/FTO/Zn(O,S) and glass/FTO/NiO/Zn(O,S)/C_{60} samples to assess the formation and the composition of the mixed crystal and to assess the correct deposition of the organic ETL, respectively.

Optical transmittance of the completed devices was measured by optical spectrophotometry (Figure 1c) within the UV–visible spectral range to assess the transparency of the absorber thin films and their absorption onset. From these measurements, it is possible to calculate the average visible transmittance (AVT) of the completed device, a paramount figure-of-merit in TPV, which gives information on the visible transparency coupled with the human eye's photopic response, thus providing weighted information on the transparency of the sample, including the perception of humans (see ref. [3] for a detailed description). It is also possible to give an estimation of the energy bandgap of the Zn(O,S) absorber via Tauc's plot, which was estimated at 2.83 eV (Figure S2, Supporting Information). This value is in good agreement with the bandgap estimated from the dependence of the bandgap of Zn(O,S) on the S relative content reported in refs. [22,23]. In Figure 1c, it can be observed that the devices are highly transparent in the visible range. The FTO substrate and back-contact, presented as reference, gives an idea on the upper limit of AVT that can be achieved (83%). The other two curves correspond to completed devices, with and without the C_{60} ETL layer for comparison. It can be observed that the devices present almost the same transmission curve. However, a slight drop in transmittance can be observed near the absorption onset region and in the visible range, as expected through the addition of the ultrathin ETL layer in the device architecture. The rest of the oxide films used present wide-bandgap above 3.5 eV, making them naturally transparent due to their energy bandgap. From these spectra, it was calculated that the AVT of the devices with and without the C_{60} ETL was 69.3% and 75.4%, respectively (**Table 1**). In Figure 1d, a picture of a device is shown as visual representation of the transparency of the device. The optical properties of the samples clearly show that they are suitable candidates for being used as an active transparent component in BIPV and other fields.

To check for the presence of the Zn(O,S) mixed crystal and confirm the composition of the Zn(O,S) absorbers, Raman spectroscopy measurements have been performed. The Raman spectrum (**Figure 2a**) from $ZnO_{1-x}S_x$ system shows a two-mode

© 2020 Wiley-VCH GmbH

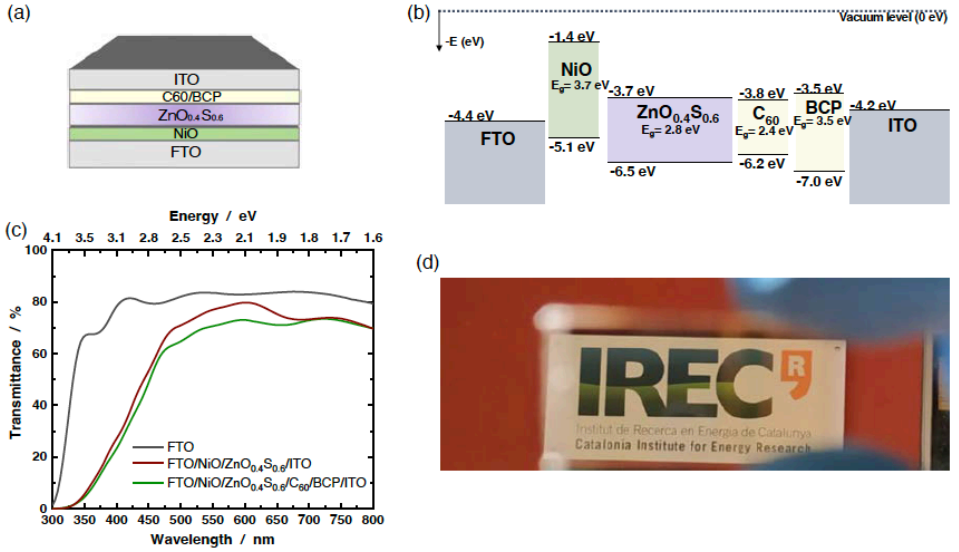

Figure 1. a) Schematic illustration of the fabricated TPV device architecture; b) Energy band diagram at equilibrium for the different layers in the system. c) Transmittance spectra of the devices FTO/NiO/Zn(O,S)/ITO and FTO/NiO/Zn(O,S)/C_{60}/BCP/ITO. FTO spectra is presented as reference and as upper limit indicator of device AVT. d) Picture taken at daylight in outdoor conditions. The picture presents a "see-through" image of the device, showing a white board with the IREC logo located at the building entrance.

Table 1. Summary of parameters and main results of fabricated TPV devices.

Device	AVT [%]	V_{oc} [V]	J_{sc} [mA cm^{-2}]	FF [%]	η [%]
FTO/NiO/$ZnO_{0.4}S_{0.6}$/ITO	75.4	0.265	0.11	32.6	<0.10
FTO/NiO/$ZnO_{0.4}S_{0.6}$/C_{60}/BCP/ITO	69.3	0.450	3.64	28.5	0.48

behavior that is characteristic of the mixed crystal, with the presence of a ZnO-like peak (located at 574 cm^{-1} in ZnO) and a ZnS-like peak (located at 351 cm^{-1} in ZnS). The frequency of the ZnO peak shows a linear dependency with the S/(S + O) composition ratio, whereas the frequency of the ZnS-like is not affected by the composition of the layers. Figure 2a shows the Raman spectra of the FTO/Zn(O,S) sample, obtained using

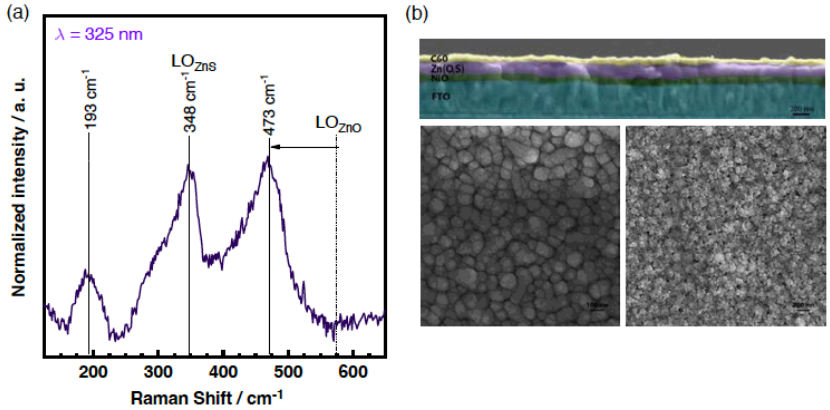

Figure 2. a) Raman spectrum of FTO/$ZnO_{1-x}S_x$ for relative sulfur content $x = S/(S + O) = 0.6$ acquired with 325 nm excitation wavelength. The main peaks observed are a characteristic Zn(O,S)-like mode at 193 cm^{-1}, the LO ZnS mode at 348 cm^{-1}, and the ZnO-like LO mode, shifted toward a lower Raman shift of 473 cm^{-1}. b) (top) CS-SEM pseudo-colored image of FTO/NiO/Zn(O,S)/C_{60}. (bottom-left) Top-view SEM image of Zn(O,S) layer. (bottom-right) Top-view SEM image of C_{60} film.

© 2020 Wiley-VCH GmbH

monochromatic 325 nm excitation wavelength. The spectra show the main peaks characteristic of the $Zn(O_{1-x}S_x)$ mixed crystal. The ZnS-like peak is visible at about 348 cm^{-1} (close to the frequency reported for the ZnS LO peak). The ZnO-like peak is observed at 473 cm^{-1}. This peak shift indicates an increase in the oxygen content with respect to the sulfur one in the Zn(O,S) structure.[22] The estimation of the S/(S + O) content ratio in the layers has been performed considering the quantitative dependence of the position of the ZnO-like peak on the alloy composition reported in ref. [22], a methodology that allows to probe the formation of the alloy avoiding errors in composition due to segregation of ZnO/ZnS into secondary phases, confirming the value of $x = 0.6$ targeted for the layers experimentally grown. In addition, a band located at the 160–225 cm^{-1} spectral region, with a peak at 193 cm^{-1} is observed, attributed to fundamental overtones out of the Γ point of the Brillouin zone activated for the induced intrinsic disorder in the mixed crystal for the break of symmetry in the crystal structure due to S–O substitution.[22,25] In addition, to check for the correct deposition and crystallization of the fullerene layer, Raman measurements were carried out (Figure S3, Supporting Information) confirming the correct deposition of the film. Importantly, it should be noted that, as reported in refs. [23,26], even though this work relies on Zn(O,S) with relative sulfur content $x = 0.6$, there is a wide region of compositions that allow adjusting the bandgap of the absorbers between 2.7 and 2.9 eV. As shown in ref. [23], working in the composition range corresponding to values of x between $x = [0.3,0.6]$ has a special interest, because in this range the bandgap as well as the conduction and valence bands of Zn(O,S) are similar for the different sulfur contents. Accordingly, in this range, the optoelectronic properties of the absorbers are not significantly affected by the variation in sulfur-relative content. This widens the choice of sulfur content to reduce the bandgap to the desired 2.7–2.9 eV range.

Field emission-scanning electron microscopy (FE-SEM) images were acquired to identify the different layers in the device and to assess the morphology of both the Zn(O,S) layer and the C_{60} layer (Figure 2b). The top image presents a cross-sectional pseudo-colored image of the device up to the fullerene layer. It can be observed that the layers are smooth and can be clearly identified, proving the correct deposition of the materials. The bottom-left image corresponds to a top-view image of the Zn(O,S) absorber layer. The Zn(O,S) layer is a compact film showing the formation of clusters of nano-sized grains. These clusters present grain sizes in the range of tens to hundreds of nanometers. The bottom-right image shows a top-view image of the C_{60} film. The film presents nanocrystalline size and some pores are present showing some degree of inhomogeneity in the processed film. Pore formation is detrimental for devices and should be avoided. To do this, two different approaches are envisaged, one involving a two-step process or bilayer, where a seed layer is formed and subsequently another layer is deposited to complete the desired thickness. Another approach would involve surface modification of Zn(O,S). Chemical or mechanical planarization of this surface would potentially decrease voids as the surface roughness plays a critical role in the growth of very thin films.

To characterize the photovoltaic properties of the devices, current density–voltage (J–V) measurements under solar simulator AM1.5G illumination (100 $mW cm^{-2}$) were carried out. **Figure 3**a shows the results obtained for the fabricated devices corresponding to the Glass/FTO/NiO/Zn(O,S)/ITO and Glass/FTO/NiO/Zn(O,S)/C_{60}/BCP/ITO device architectures. These results and the parameters obtained are summarized in Table 1. These measurements confirm the existence of a photovoltaic effect in the heterojunction devices that is mainly attributed to the selective absorption of UV photons in the Zn(O,S) optically transparent layers and that Zn(O,S)-based heterojunction solar cells can be fabricated. The device without the C_{60} ETL presents still quite low short-circuit current density, in the order of 0.11 mA cm^{-2}, and a moderate open-circuit voltage of 0.256 V. These values serve as proof-of-concept of the PV functionality of the Zn(O,S) absorbers. However, an overall low efficiency, below 0.1% is observed for the nonoptimized FTO/NiO/Zn(O,S)/ITO device architecture. Nonetheless, the AVT is notably high, slightly over 75%.

Upon introduction of a C_{60} ETL together with an ultrathin BCP hole-blocking layer, the device performance is significantly

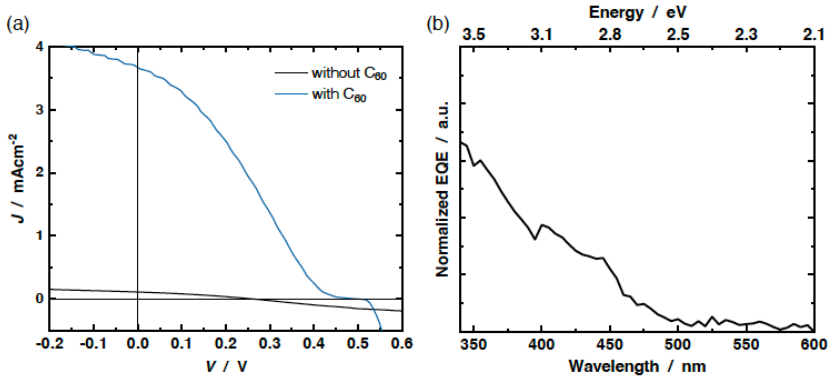

Figure 3. a) Photovoltaic characterization of fabricated TPV devices. J–V measurements under AM1.5G illumination for Zn(O,S) devices with S content $x = 0.6$, with (blue) and without (gray) the organic C_{60} ETL.

© 2020 Wiley-VCH GmbH

increased, due mainly to the increase in photocurrent and also (in a minor degree) to the increase in the photovoltage. The device presents a $J_{sc} = 3.64\,mA\,cm^{-2}$, a V_{oc} close to 0.5 V, and a low FF that yield an efficiency of 0.48% (Table 1). This device still shows an AVT of 69.3%. With these parameters, it is possible to calculate a figure-of-merit in TPV, the light utilization efficiency (LUE), which is the product of efficiency times the AVT of the device.[3] The calculated value for this device gives LUE = 0.34%. This is significantly higher than the best values achieved up to now with UV ZnO solar cells, according to the table found in supplementary data reported in ref. [3]. Albeit promising, the PCE value is still too low. However, the results are promising and can lead to the realization of real-life application devices. As reported by Traverse et al. in ref. [3], PCEs in the range 2–5% are sufficient to autonomously power smart windows and low-power displays. Future strategies for increasing the PCE rely on the identification and replacement of the CTLs, especially in the case of the NiO hole-transport layer (HTL), which could potentially be replaced by other materials such as MoS_2 or MoO_3. In addition, the Zn(O,S) film can be optimized, in terms of fine tuning carrier concentration and morphology.

Taking now a closer look into the *J*–*V* characteristics of the hybrid device, there are some particularities in the shape of the curve that need to be carefully addressed. The nonconventional shape already indicates that the device presents some limitations in performance. First, due to the low FF and second, and most important in the analysis, two regions are observed with a special behavior. For voltages closer to the V_{OC}, there is a region that shows a constant current near to zero, instead of a monotonous increase toward a negative current density. This nondesired behavior has already been reported in previous works in the organic PV community, and it is commonly known as the "S-kink". The possible working mechanisms have been related to interface morphology, oxygen doping, and the presence of charged interfaces forming extraction and injection barriers.[27] This shows the critical role of interfacial phenomena in these solar cells.

The speculative interpretation of the presence of the S-kink in the Zn(O,S) solar cells is likely related to the formation of an interfacial barrier at the CTL/electrode interface and/or at the HTL/Zn(O,S), as supported by previous reports.[28–30] It results in a V_{OC} and FF deficit, which limits device efficiency. It is suggested that by introducing an ultrathin dipolar molecule layer, such as LiF, at the interface might alleviate this issue, due to the formation of an electric dipole that generates a localized polarization field minimizing the barrier. This would lead to a reduced interface recombination. Interfacial optimization can thus potentially remove the S-kink behavior and increase device efficiency. Replacing NiO by other well-suited HTL could also result in increased performance.

Finally, another interesting aspect in the *J*–*V* characteristics happens in the region $V \in [-0.2, 0.05]$ V. A linear dependence of the photocurrent as a function of voltage is observed in this region. This particular behavior has been reported in organic planar heterojunctions with CuPc/C_{60} and explained in the work by Jeong et al.,[31] by experiment and simulation. It has been shown that the linear dependence of the photocurrent with bias originates from the C_{60} layer due to an effect known as bulk ionization photoconductivity. The maximum bulk ionization yield photocurrent has been calculated, reaching values below $0.7\,mA\,cm^{-2}$ for a 40 nm thick layer and of $0.35\,mA\,cm^{-2}$ for a 35 nm layer. The implications are that C_{60} can indeed participate actively in the PV effect due to this bulk ionization effect, but this is an additional or secondary effect that couples and is observed in the *J*–*V* curve under illumination at small forward and reverse bias. The PV effect can then be mainly attributed to the UV absorption by Zn(O,S) and to the formation of a hybrid donor–acceptor (D/A) interface with the fullerene layer that is involved in charge separation and in electron transport and collection through the ITO electrode. This hypothesis is supported also by the observation of PV effect in the devices without the C_{60} ETL.

To further confirm that the device presents selective UV absorption, spectral response measurements were carried out. Figure 3b shows the measured normalized external quantum efficiency (EQE) of the device containing the C_{60} layer. It can be seen that the EQE curve rises from 2.7 eV toward higher energies, suggesting that absorption indeed takes place in the UV region and that it is mostly related to absorption in Zn(O,S). The poor shape of the EQE curve indicates also that hole-extraction is limited, as seen by the low steepness of the curve in the lower energy region.

In summary, the fabrication of UV-selective transparent solar cells based on Zn(O,S) in a fully transparent device in a planar configuration incorporating transparent electrical contacts has been presented for the first time. Zn(O,S) mixed crystal absorbers were successfully synthesized in the intermediate range with sulfur-relative content $x = 0.6$, thus enabling the precise choice of bandgap and optical absorption onset, in this case around 2.8 eV. This material is deemed as better suited for UV-selective absorption and filtering, as compared with the most commonly studied ZnO, because of the possibility to adjust the bandgap of the absorber to values closer to the UV onset by controlling the absorber composition, resulting in a better spectral match for such application. It is critical to identify optimal electron and hole selective transport layers better suited to the Zn(O,S) wide bandgap absorbers. It would also be interesting to investigate other compositional regions in the Zn(O,S) system, as different crystal structures can be obtained in either O-rich region or in S-rich region and the bandgap energy can still be placed below 3 eV. The experimental confirmation on the existence of a photovoltaic effect in the synthesized Zn(O,S)-based devices is very promising and confirms the interest in the development of Zn(O,S) mixed crystal as absorber layers for UV-selective TPV applications with very high optical transparency and its potential use as active photovoltaic component. Other potential applications such as UV-photodetectors, powering IoT devices, UV-light-emitting diodes (LEDs), and tandem PV devices are also envisaged.

Experimental Section

Sample Preparation: The solar cells fabricated in this work present the structure Glass/FTO/NiO(40 nm)/$ZnO_{0.4}S_{0.6}$(105 nm)/ITO(190 nm) and Glass/FTO/NiO(40 nm)/$ZnO_{0.4}S_{0.6}$(105 nm)/C_{60}(35 nm)/BCP(5 nm)/ITO(190 nm). Commercial Glass/FTO substrates (Merck; $R_{sh} = 12\,\Omega\,sq^{-1}$) were used as substrate and back-contact for the solar cell devices. Prior to

© 2020 Wiley-VCH GmbH

deposition, substrates were first rinsed in distilled water, dried in Ar flux and afterward cleaned by subsequent baths in isopropanol and milli-Q H_2O in an ultrasonic bath at room temperature for 10 min each and then were dried with Ar flux. NiO films were deposited on FTO by electron beam evaporation (Oerlikon Univex 250). NiO pieces (Alfa Aesar; 3–12 mm, 99.995%) were used as evaporant in a 4cc Al_2O_3 liner (Neyco). The chamber was evacuated at a base pressure of 10^{-6} mbar before evaporation and the deposition took place at room temperature, with no intentional heating, at 10 kV and with an electron current of 9 mA, at a rate of 0.5 Å s^{-1} measured with a quartz crystal microbalance (Inficon SQC-310; Au 6 MHz sensor). Zn(O,S) layers were deposited by sputtering (von Ardenne CS730S) from mixed ZnO/ZnS targets. Deposition parameters were RF power density 0.95 W cm^{-2} (i.e., 300 W, growth rate ≈15–24 nm min^{-1}), total gas flow 20 sccm argon at 10 µbar. Prior deposition, all samples were heated to 150 °C (nominal) in vacuum and remained throughout on the heater while deposition. C_{60} solution was prepared by dissolving C_{60} (TCI, 99.5%) in 1,2-dichlorobenzene with a concentration of 10 mg mL^{-1}. The solution was filtered with a polytetrafluoroethylene (PTFE) filter of 0.42 µm pore size prior its use. Thin films were deposited by static spin-coating at 1500 rpm for 60 s and transferred to a preheated hotplate at 80 °C in air for 2 min. BCP (TCI, 99.0%) was dissolved in dry IP at 0.6 mg mL^{-1}. BCP solution was filtered with a 0.22 µm pore-size filter and spin-coated at 5000 rpm for 30 s. To complete the device, a 190 nm thick ITO film was deposited by DC-Pulsed Magnetron Sputtering (Alliance CT-100). Prior to deposition, the chamber was evacuated at 10^{-7} mbar and the substrate was heated up to 200 °C. The ITO target (Neyco; In_2O_3/SnO_2 90/10 wt%, 4N) was presputtered to remove any surface contaminants with the shutter in closed configuration. The deposition took place at 200 °C at a working pressure of 3×10^{-3} mbar in a mixed Ar/O_2 atmosphere at 30/0.5 sccm, applying a DC power density of 1.9 W cm^{-2} to the target.

Characterization: UV–vis measurements were acquired with a dual-beam spectrophotometer setup (Perkin Elmer Lambda L35) in transmittance mode (light source and detector normal to sample's surface (i.e., 0°)) scanning from 300 to 800 nm.

Raman spectroscopy was performed with a FHR640 Horiba Jobin–Yvon spectrometer coupled to a Raman probe developed at Institut de Recerca en Energia de Catalunya (IREC) and a cryogenically cooled charge coupled device detector. Measurements were carried out in backscattering configuration and with a 325 nm UV laser as the excitation wavelength. An excitation power density of about 25 W cm^{-2} was used to inhibit thermal effects on the samples. The Raman shift was calibrated using a Si monocrystal reference and adjusting the Raman shift for the main Si band at 520 cm^{-1}.

FE-SEM images were acquired with a ZEISS Auriga Series system. The images were acquired at 5 kV, aperture of 20 µm, and working distance of around 4 mm with the InLens detector.

J–V measurements under illumination were carried out using a home-made setup consisting on a 150 W xenon broadband arc Lamp (Thorlabs SLS401) calibrated using a NREL-certified Si reference solar cell (Abet Technologies, Model 15150). Electrical measurements were carried out with a source-measure unit (Keithley 2400) in four-wire sense mode, controlled by the software Tracer (ReRa solutions) using a IEEE 488 GPIB Instrument Control Device (National Instruments GPIB-USB-HS).

EQE curves were obtained using a spectral response system (Bentham PVE300) calibrated with a Si photodiode.

Supporting Information

Supporting Information is available from the Wiley Online Library or from the author.

Acknowledgements

This work has received funding from the European Union H2020 Framework Programme under Grant Agreement no. 826002 (Tech4Win). Authors from IREC and Universitat de Barcelona belong to the SEMS (Solar Energy Materials and Systems) Consolidated Research Group of the "Generalitat de Catalunya" (Ref. 2017 SGR 862). D.P. thanks to the funding from the Basque Country PI2018-08 (PISCES).

Conflict of Interest

The authors declare no conflict of interest.

Keywords

hybrids, transparent photovoltaics, ultraviolet-selective solar cells, wide-bandgaps, Zn(O,S)

Received: August 10, 2020
Revised: September 1, 2020
Published online: September 20, 2020

[1] G. Masson, I. Kaizuka, https://iea-pvps.org/wp-content/uploads/2020/02/5319-iea-pvps-report-2019-08-lr.pdf (accessed: March 2020).
[2] R. R. Lunt, *Appl. Phys. Lett.* **2012**, *101*, 043902.
[3] C. J. Traverse, R. Pandey, M. C. Barr, R. R. Lunt, *Nat. Energy* **2017**, *2*, 849.
[4] X. Lin, Y.-L. Loo, M. Sezen-Edmonds, N. C. Davy, J. Gao, A. Liu, A. Kahn, N. Yao, *Nat. Energy* **2017**, *2*, 17104.
[5] A. Pérez-Rodríguez, *presented in NEXTGEN '19: 2019 Next Generation High Efficiency Photovoltaics International School and Workshop*, Mallorca, October 2019.
[6] K. Ellmer, A. Bikowski, *J. Phys. D.: Appl. Phys.* **2016**, *49*, 413002.
[7] M. Grundmann, F. Klüpfel, R. Karsthof, P. Schlupp, F. L. Schein, D. Splith, C. Yang, S. Bitter, H. Von Wenckstern, *J. Phys. D. Appl. Phys.* **2016**, *49*, 21.
[8] D. K. Ban, M. Patel, T. T. Nguyen, J. Kim, *Adv. Electron. Mater.* **2019**, *5*, 1900348.
[9] T. T. Nguyen, M. Patel, J. W. Kim, W. Lee, J. Kim, *J. Alloys Compd.* **2020**, *816*, 152602.
[10] R. Karsthof, P. Räcke, H. Von Wenckstern, M. Grundmann, *Phys. Status Solidi A* **2016**, *213*, 30.
[11] R. Karsthof, H. von Wenckstern, M. Grundmann, *J. Vac. Sci. Technol. B* **2016**, *34*, 04J107.
[12] M. Patel, H. S. Kim, J. Kim, J. H. Yun, S. J. Kim, E. H. Choi, H. H. Park, *Sol. Energy Mater. Sol. Cells* **2017**, *170*, 246.
[13] L. Han, X. Zhao, M. Ma, F. Gao, X. Xun, Q. Liao, Z. Zhang, Z. Kang, Y. Zhang, *Nano Energy* **2019**, *57*, 528.
[14] Ü. Özgür, Y. I. Alivov, C. Liu, A. Teke, M. A. Reshchikov, S. Doğan, V. Avrutin, S.-J. J. Cho, H. Morkoç, S. Doğan, V. Avrutin, S.-J. J. Cho, H. Morkç, *J. Appl. Phys.* **2005**, *98*, 041301.
[15] E. Schiff, *Sol. Energy Mater. Sol. Cells* **2003**, *78*, 567.
[16] M. Liu, M. B. Johnston, H. J. Snaith, *Nature* **2013**, *501*, 395.
[17] S. A. Veldhuis, P. P. Boix, N. Yantara, M. Li, T. C. Sum, N. Mathews, S. G. Mhaisalkar, *Adv. Mater.* **2016**, *28*, 6804.
[18] A. M. Elseman, C. Xu, Y. Yao, M. Elisabeth, L. Niu, L. Malavasi, Q. Liang Song, *Sol. RRL* **2020**, *4*, 2000136.
[19] W. Shockley, H. J. Queisser, *J. Appl. Phys.* **1961**, *32*, 510.
[20] M. Burgelman, P. Nollet, S. Degrave, *Thin Solid Films* **2000**, *361–362*, 527.
[21] C. Persson, C. Platzer-Björkman, J. Malmström, T. Törndahl, M. Edoff, *Phys. Rev. Lett.* **2006**, *97*, 146403.
[22] M. Guc, M. Neuschitzer, D. Hariskos, A. Bauer, W. Witte, W. Hempel, L. Calvo-Barrio, P. Pistor, A. Perez-Rodriguez, V. Izquierdo-Roca, *RSC Adv.* **2016**, *6*, 24536.

© 2020 Wiley-VCH GmbH

[23] A. Polity, B. K. Meyer, T. Krämer, C. Wang, U. Haboeck, A. Hoffmann, *Phys. Status Solidi A* **2006**, *203*, 2867.
[24] G. Baldissera, C. Persson, *J. Appl. Phys.* **2016**, *119*, 045704.
[25] R. Cuscó, E. Alarcón-Lladó, J. Ibáñez, L. Artús, J. Jiménez, B. Wang, M. J. Callahan, *Phys. Rev. B* **2007**, *75*, 165202.
[26] A. Bechlaghem, B. Zebentout, Z. Benamara, *Results Phys.* **2018**, *10*, 650.
[27] A. Gusain, R. M. Faria, P. B. Miranda, *Front. Chem.* **2019**, *7*, 61.
[28] W. Tress, K. Leo, M. Riede, *Adv. Funct. Mater.* **2011**, *21*, 2140.
[29] W. Tress, O. Inganäs, *Sol. Energy Mater. Sol. Cells* **2013**, *117*, 599.
[30] A. Wagenpfahl, D. Rauh, M. Binder, C. Deibel, V. Dyakonov, *Phys. Rev. B* **2010**, *82*, 115306.
[31] W.-I. Jeong, Y. E. Lee, H.-S. Shim, T.-M. Kim, S.-Y. Kim, J.-J. Kim, *Adv. Funct. Mater.* **2012**, *22*, 3089.

© 2020 Wiley-VCH GmbH

Copyright WILEY-VCH Verlag GmbH & Co. KGaA, 69469 Weinheim, Germany, 2018.

Supporting Information

UV-Selective Optically Transparent Zn(O,S)-based Solar Cells

Alex J. Lopez-Garcia, Andreas Bauer, Robert Fonoll Rubio, David Payno, Zacharie Jehl Li-Kao, Samrana Kazim, Dimitrios Hariskos, Victor Izquierdo-Roca, Edgardo Saucedo, Alejandro Pérez-Rodríguez*

The modelling is performed using SCAPS 3.300. The optical parameters are inputted as a simple absorption coefficient above the bandgap of the absorber. The material chosen as an absorber is Zn(O,S) with different S content, varying the bandgap from 3.3eV down to 2.7eV. The absorber doping is taken p-type with a carrier concentration of 10^{16} cm^{-3}, and the absorber thickness is 1 µm. The front window is a combination of 50 nm i-ZnO (n-doping, 10^{17} cm^{-3}) and 300 nm highly n-doped ZnO:Al (n-doping, 10^{20} cm^{-3}). The contacts at the back and front interface are taken ideal (flat band, perfectly ohmic). The material parameters are taken from [M. Gloeckler et al., Proc. 3rd World Conference on Photovoltaic Energy Conversion, 2003, 2003, vol. 1, p. 491–494 Vol.1; Z. Jehl Li Kao et al., Proc. 23rd PVSEC Taipei Taiwan, Oct. 2013]. No defects are implemented in the absorber, so no voltage deficit should be observed. As the absorber does not have any defect implemented in the modelling, the solar cells are very close to the radiative limit and SRH recombination are nearly inexistent. Therefore, the open circuit voltage (Voc) increases steadily with the bandgap, without experiencing any of the deficit usually observed in the experiments for large bandgap solar cells. Similarly, the fill factor (FF) is extremely stable, and the diode behaviour is insensitive with the increasing band gap since the only recombination path is radiative. Therefore, the efficiency of the cells is purely dictated by the exponential decrease of the short-circuit current density (Jsc), related only on the variation of the extinction coefficient of the material when varying the bandgap.

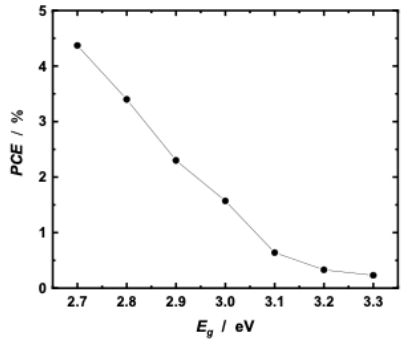

Figure S1. Efficiency plot as a function of the energy bandgap (function of S/(S+O) relative content) of the Zn(O,S) mixed crystal extracted from SCAPS modeling in a realistic device configuration.

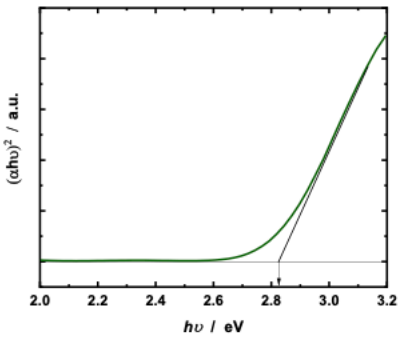

Figure S2. Tauc's plot based on absorption coefficient values extracted from Transmittance measurements of Zn(O,S) on glass/FTO. A bandgap energy of 2.83 eV is estimated for Zn(O,S) by this method.

Raman measurements with UV excitation of 325 nm has been performed in order to confirm the deposition of the C_{60} layer. The UV excitation allows to have strong light-matter interaction even with such a nanometric layer, enhancing detectivity of the C_{60} nanolayer. Figure S2 shows the resulting spectrum, showing indeed the characteristic peaks that correspond to C_{60} as reported by I. Kopova et al. [*Int. J. Mol. Sci.* **2013**, 14, 9182-9204]. This confirms the correct deposition and crystallization of the fullerene layer.

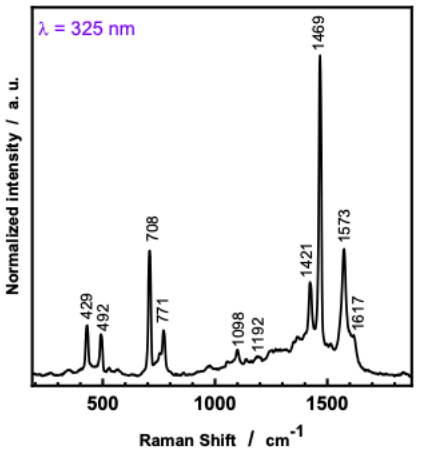

Figure S3. Raman spectra of C_{60} acquired using 325 nm excitation wavelength.

3.3 – Second research article

Solar RRL
www.solar-rrl.com

Ultrathin Wide-Bandgap a-Si:H-Based Solar Cells for Transparent Photovoltaic Applications

Alex J. Lopez-Garcia, Oriol Blazquez, Cristobal Voz, Joaquim Puigdollers, Víctor Izquierdo-Roca, and Alejandro Pérez-Rodríguez*

Herein, the fabrication of UV-blue selective transparent solar cells based on ultrathin (<30 nm) intrinsic hydrogenated amorphous silicon films (a-Si:H) as absorber and using a fully inorganic architecture is reported, using metal-oxide thin films as carrier selective contacts and as transparent electrical contacts. These transparent ultrathin devices present a photovoltaic effect and high average visible transmittance (AVT), showing their potential as candidates for implementation as a transparent energy harvester. Potential applications range from Building-Integrated PV to agrophotovoltaics, and can also be of interest as a ubiquitous and inexpensive power source integrated in functional devices such as low-power devices, Internet of Things devices, and other sensors. Glass/FTO/ZnO/a-Si:H/MoO_3/ITO device prototypes are produced. These devices present an AVT ranging from 50% to 69%, present a photovoltaic effect with a power conversion efficiency up to 0.5% calculated for an AM1.5G spectrum and have light utilization efficiency (LUE) values of 0.25%, confirming the potential of the proposed device architectures for the development of highly transparent devices with improved LUE.

1. Introduction

There is no denying on the fact that solar energy has already attained a main role as a sustainable and renewable energy source in the energy mix of many countries in the last years. PV technologies opened the possibility of providing clean energy in a wide array of settings, focusing on the deployment of vast solar arrays or farms, while some others in more local settings, such as in buildings, in order to provide onsite energy. Conventional PV technologies suffer some important drawbacks that limit the possibility of using solar energy as the main energy source to power many different and diverse applications. Main issues are: usage of very large areas of land, high visual impact, weight, costs, raw material availability, limited efficiencies, environmental impact and low stability, among others, which depend on the kind of PV technology. Due to these facts, in order to expand the PV industry, it seems quite relevant to try to extend the range of applications and implementations of photovoltaic technologies. It is thus important to look back into what has been done and create new concepts that are applicable and translatable to the industry.

In the last years, increasing efforts have been made to obtain semitransparent and fully transparent PV (TPV) devices that can be integrated in window façades. Building-Integrated PV (BIPV) applications are a clear example aiming to obtain near-zero emission buildings with solar cells fully integrated components of the building.[1–5] Other novel applications include agrophotovoltaics (APV) and application as devices that could be integrated as functional components to power mid and low power optoelectronic devices such as sensors, electrochromic windows, as a multifunctional harvester and optical filter, as indoor light harvesters or Internet of Things devices.[6–11]

For transparent PV applications maximal efficiency is not the key premise for massive deployment. Instead, other aspects such as visual impact, low cost, and stability play an important role in their viability. For example, it will be more feasible (and practical) to integrate a solar cell in a glass façade if it does not disturb the building visual aspect (i.e., integration has greater potential for a transparent PV cell that reaches 10% efficiency than to attach 25% silicon PV modules and leave gaps in the windows). TPV devices can either be wavelength selective or non-selective, and have been fabricated with different absorber materials and device architectures.[12–14]

As for inorganic wavelength-selective-based devices, oxide and chalcogenide materials are very interesting for the development of this technology as they are stable, inexpensive, abundant, easy

A. J. Lopez-Garcia, O. Blazquez, V. Izquierdo-Roca, A. Pérez-Rodríguez
Institut de Recerca en Energia de Catalunya (IREC)
Jardins de les Dones de Negre
08930 Barcelona, Spain
E-mail: alopez@irec.cat

C. Voz, J. Puigdollers
Departament Enginyeria Electrònica
Universitat Politècnica Catalunya
08034 Barcelona, Spain

A. Pérez-Rodríguez
IN2UB
Departament d'Enginyeria Electrònica i Biomèdica
Universitat de Barcelona
08028 Barcelona, Spain

The ORCID identification number(s) for the author(s) of this article can be found under https://doi.org/10.1002/solr.202100909.

© 2021 The Authors. Solar RRL published by Wiley-VCH GmbH. This is an open access article under the terms of the Creative Commons Attribution-NonCommercial License, which permits use, distribution and reproduction in any medium, provided the original work is properly cited and is not used for commercial purposes.

DOI: 10.1002/solr.202100909

to process at industrial scale and typically nontoxic. State-of-the-art inorganic UV-selective solar cells are mainly based on the use of ZnO or Zn(O,S) as the absorber material, but even though presenting high average visible transparency (AVT) values, they still have to overcome an efficiency limited to around 0.5%.[15–19] However, recently, there have been demonstrations on implementing a-Si:H in UV-selective metal-oxide-based solar cells, showing the possibility to overcome this PCE limitation, but at the cost of losing some transparency.[20] The use of a-Si based technologies in this emerging field of PV has added benefits in terms of the use of materials that are stable and durable, that are not deemed as critical raw. Besides, it allows for high-throughput and readily implementation in the already existing a-Si industry and additionally, the low-temperature used during processing allows for device implementations in alternative substrates, ranging from rigid substrates such as metallic or glass-based to flexible substrates such as PET.[21] These features highlight the versatility of this TPV application.

In this work, transparent PV cells based on ultrathin intrinsic a-Si:H and oxide-based charge transport layers (CTLs) are presented. It is shown that it is possible to tune the AVT and PCE as a function of the a-Si:H absorber thickness. A study of the effect of the different CTLs in the structure is presented. It is demonstrated that these cells absorb light in the UV range and in the blue range, by making the absorber ultrathin to increase its visual transparency at longer wavelengths. Optical and electrical properties of the fabricated devices are analyzed and discussed herein.

2. Results and Discussion

In the present work, TPV devices have been fabricated using a structure consisting of Glass/FTO/ETL/a-Si:H/HTL/ITO (**Figure 1**). Note that, the ETL and HTL layers in this structure replace the n-doped and p-doped layers of classical p-i-n solar cells, respectively. FTO and ITO act as transparent electrodes, ultrathin intrinsic a-Si:H works as the absorber layer. As carrier selective contacts, metal-oxide ZnO (ETL: electron transport layer) and MoO_3 (HTL: hole transport layer) have been explored. These materials have already been studied as CTLs for conventional c-Si and a-Si:H technologies, as well as other technologies, due to its wide-bandgap, stability, material availability, and low cost.[22–24]

Traditionally, a-Si:H conventional (opaque) devices rely on forming either a p-i-n homojunction using doped a-Si:H or heterojunction using a-SiC:H as CTL.[25,26] In this particular application, we stress that the visual aspect and transparency are critical features. Given the direct bandgap of a-Si:H (ranging from 1.8 to 2.1 eV) and its relatively high absorption coefficient, the parasitic absorption in these functional charge-selective films is an aspect to be avoided, leading thus to this change in architecture implementing metal-oxide alternatives.[27–29] In terms of electrical properties, photogenerated carriers in the a-Si:H absorber have a rather short diffusion length.[30–32] However, given that we work with an ultrathin absorber, charge carrier collection in this case can easily occur, so photogenerated carriers will reach the interfaces with the metal-oxide selective contacts. This highlights an important aspect of these cells, which is the need of effective defect passivation, especially at the interfaces a-Si:H/CTL. Finally, the absorber thickness will also have a paramount impact on both PCE and AVT, placing an effective trade-off between both parameters as a function of the thickness of the absorber, which will be discussed also.

Following optoelectronic characterization, we begin by analyzing the ZnO ETL and its impact on the device functionality. Then we study the impact of the MoO_3 HTL. Afterward, after selecting the CTL materials and their thickness we turn the focus into the effect of the ultrathin absorber film and its impact on TPV parameters, mainly in terms of AVT, color rendering index (CRI), PCE and LUE. All these aspects are discussed herein.

2.1. Analysis of the Impact of the Electron and Hole Selective Contacts and Absorber Thickness

2.1.1. ZnO ETL

Recently, some studies have presented UV-selective metal-oxide/a-Si:H-based TPV lab cells that incorporate NiO as HTL and thick ZnO film that also absorbs some UV radiation.[20] The a-Si:H film was incorporated in order to improve electrical transport at the interface ZnO/NiO. Instead, it also seems to work as an absorber, as it is shown throughout this work. The referenced report showed that a 400 nm ZnO acted as a UV absorber. However, an efficient ETL is usually made with thinner materials, typically of few nanometers in thickness, giving that carrier collection relies on tunneling mechanisms if their work function is adequate respect to the absorber energy bands.

With this in mind this work has studied the implementation of ZnO as an effective ETL in the a-Si:H system. The study consisted on using a 15 nm intrinsic a-Si:H absorber and a fixed HTL thickness and testing devices with different ZnO thicknesses: 0, 50, and 400 nm. The device structure is SLG/FTO/ZnO/a-Si:H (15 nm)/MoO_3(20 nm)/ITO. These devices have been characterized and *J–V* measurements have been carried out (**Figure 2a**).

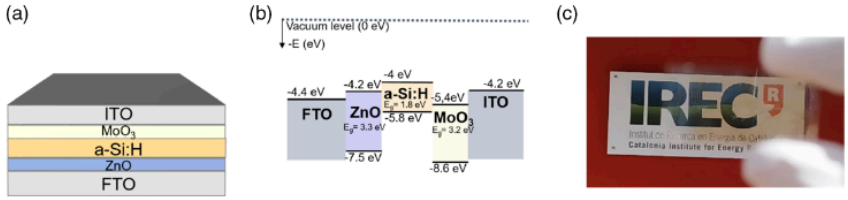

Figure 1. a) Schematic illustration of the TPV device architecture; b) energy band diagram in equilibrium for the different nanometric films in the system. c) Picture taken outdoors in broad daylight. The picture shows the TPV device, showing a white board with the IREC logo located at the building entrance. The IREC logo is reproduced with permission from the institute.

© 2021 The Authors. Solar RRL published by Wiley-VCH GmbH

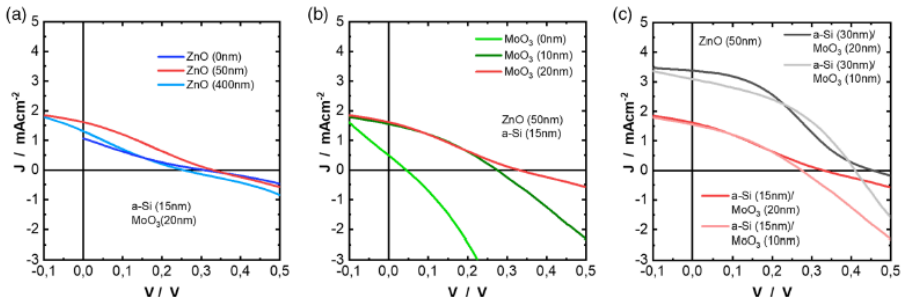

Figure 2. Photovoltaic characterization of fabricated TPV devices. a) *J–V* measurements under AM1.5G illumination of a device with a 20 nm MoO_3 HTL and a 15 nm a-Si:H absorber with different ETL thicknesses. b) *J–V* measurements for a 15 nm a-Si:H absorber and a 50 nm ZnO ETL with different HTL thicknesses. c) *J–V* measurements of devices with varying a-Si:H thicknesses with a fixed 50 nm ZnO ETL. For each a-Si:H thickness, for comparison, there are two MoO_3 films with 10 and 20 nm thicknesses.

Photovoltaic effect is obtained in all three cases. However, there are clear differences. While all three devices present a similar V_{OC}, FF, and J_{SC} are clearly affected by the thickness of the ETL. For the case of no ZnO layer (i.e., 0 nm), the shape of the curve in the first quadrant is almost a straight line from 0 V to V_{OC}. This suggests that some charges (electrons) absorbed in the ultrathin a-Si:H film can be collected as they can reach the interface with the FTO. However, the very low FF can indicate the presence of a barrier at this interface that increases recombination. By introducing the ZnO film with thickness of 50 nm an overall performance increase is observed. Notably J_{SC} and FF are enhanced, showing the need for an ETL that eases electron transport from a-Si:H to the electrical contact. However, if ZnO thickness is increased to 400 nm the photovoltaic parameters are impacted, and a reduction in performance is observed. This is attributed to a high resistance due to the intrinsic nature and high thickness of the fabricated ZnO film, causing a drop in J_{SC} and FF, as compared with the device with a 50 nm film. According to this, an optimized device using an Al-doped ZnO (AZO) layer as ETL has been produced and is discussed in Section 2.2.

2.1.2. MoO_3 HTL

Same as for the ETL case, it is worth moving toward HTLs with a wide bandgap, higher than 3 eV, in order to increase device transparency and reduce visual impact. In this work, MoO_3 is studied as HTL. MoO_3 presents a wide bandgap of 3.2 eV and a high work function, which makes it a good hole selective contact.

Similarly, different thicknesses have been explored: 0, 10, and 20 nm. Absorber thickness and ETL thickness were fixed to 15 and 50 nm, respectively. From the current–voltage characteristics the influence of the material and its thickness on the photovoltaic parameters of the devices is assessed. (Figure 2b)

The device with no MoO_3 presents almost no PV effect whatsoever, signaling the need of a HTL in order to promote hole collection at the front contact. When a 10 nm MoO_3 film is introduced in the device structure PV effect is clearly observed, showing in this case a V_{oc} close to 0.3 V. Fill factor is quite low, 30%, indicating high series resistance and low shunt resistance. When a 20 nm MoO_3 film is used the efficiency is almost the same, with a similar J_{SC} of the device with 10 nm film. However, FF and V_{OC} are slightly different. For the 20 nm films, an anomaly in the conventional exponential shape of the current–voltage curve is observed. This anomaly has been discussed already in literature in both organic and inorganic PV materials and is dubbed as s-shape, kink, or roll-over.[33–39] The impact on PV parameters is basically a reduction in FF due to a dampening of the exponential current flow with increasing voltage up to a given value where the single exponential character is recovered. These lead to a lower maximum power point than for a device without such s-shape. It can be observed that FF is reduced but V_{OC} slightly increases as compared with the case of a 10 nm MoO_3 film. Overall, the efficiency is almost the same.

The MoO_3 films are deposited by thermal evaporation at ambient temperature and were exposed to air. It has been reported that air exposed MoO_3 films present a reduced WF of 5.4 eV as compared with films unexposed to air, reported at 6.8 eV.[22,40,41] Hole transport in MoO_3 has been studied in both organic and inorganic PV technologies. Even though presenting n-type conductivity the material yields efficient hole transport. Concretely, in a-Si:H devices, the conduction band of MoO_3 is reported to be lower than the valence band of a-Si:H leading to band-to-band tunneling transport. However, if the WF is not low enough, a barrier will form. In this case the transport is also mediated by gap-states through trap-assisted tunneling. These gap-states have been attributed to oxygen vacancies and give rise to its conductivity. The height of the barrier formed at the interface a-Si:H/MoO_3 will heavily depend on the WF of the MoO_3. Thus, WF is a critical parameter affecting carrier selectivity.[42–45]

In this work, the loss of selectivity observed for the thicker MoO_3 HTLs could be attributed to two factors. The first one is the mentioned barrier due to the reduced WF due to air exposure. In this case, the hole selectivity relies on efficient tunneling via gap-states. The thicker film will possess higher resistance and recombination at the film will occur as charge accumulates, leading to the roll-over effect. However, for the 10 nm film, the curve presents a conventional exponential shape, indicating good hole selectivity, suggesting the use of even thinner films if these present excellent coverage. Nonetheless, for both film thicknesses, FF and V_{OC} present quite low values. Given the nanometric thickness of the films present in the device, it is expected that

© 2021 The Authors. Solar RRL published by Wiley-VCH GmbH

interfaces play a critical part in device functionality. It is critical to minimize energy barriers at the interfaces to have good carrier extraction. Besides, a low-defect density and well passivated interfaces are needed in order to reduce interface recombination, as this will be the dominant nonradiative recombination mechanism (given that bulk effects can be neglected at these feature sizes). Hence, this can be a potential way to notably increasing device efficiency while maintaining similar or equal AVT values.

2.1.3. Analysis of the a-Si:H Absorber Thickness

After studying the effect of the CTLs, we aim at studying and optimizing the a-Si:H absorber thickness. In this work, two absorber thickness values are investigated: 15 and 30 nm. The ZnO ETL is fixed to 50 nm and two different thicknesses of 10 and 20 nm MoO_3 films are used as HTL, according to the results presented in the previous sections. This gives a total of four different device combinations (FTO/ZnO[50 nm]/a-Si:H[15,30 nm]/MoO_3[10,20 nm]/ITO). In order to have representative results that can be compared, we make device production in parallel. Thus, a single deposition of ZnO is done, then two devices are subjected to the 15 nm a-Si:H deposition and the other two to the 30 nm deposition. Later, one 15 nm and one 30 nm device are subjected to a 10 nm MoO_3 deposition and the remaining pair of devices to the 20 nm MoO_3 deposition. Finally, a single ITO deposition for all devices is carried out.

Subsequently, current–voltage measurements under AM1.5G illumination have been carried out and will be discussed in this subsection (Figure 2c).

First, and continuing with the discussion of the previous subsection, regardless of absorber thickness and ETL, an s-shaped profile is observed for devices with the 20 nm MoO_3 HTL. Focusing on effects related to the absorber thickness, it is observed that the photovoltaic parameters are improved overall for the thickest absorber regardless of the carrier selective contacts (**Table 1**). This is straightforward, given the fact that we are working with ultrathin nanometric films and that there is a forced absorption loss. Thus, in an ideal case, the expected result could be an effective doubling of J_{SC}. Experimental results show higher J_{SC}, almost double comparing the 30 nm against the 15 nm a-Si:H film (regardless of the HTL thickness). FF and V_{OC} also increase notably for the case of the 30 nm absorber, with values up to 41% and 0.46 V, respectively.

Table 1. Summary of device parameters of absorber thickness variation analysis.

TPV device structure	V_{oc} [V]	J_{sc} [mA cm^{-2}]	FF [%]	PCE [%]
FTO/ZnO (50 nm)/a-Si:H (15 nm)/MoO_3 (10 nm)/ITO	0.29	1.85	31.0	0.21
FTO/ZnO (50 nm)/a-Si:H (30 nm)/MoO_3 (10 nm)/ITO	0.41	3.09	41.4	0.51
FTO/ZnO (50 nm)/a-Si:H (15 nm)/MoO_3 (20 nm)/ITO	0.33	1.86	30.8	0.22
FTO/ZnO (50 nm)/a-Si:H (30 nm)/MoO_3 (20 nm)/ITO	0.46	3.50	33.4	0.52

2.2. Device Architecture Design of Resulting TPV Devices

In this section, the best devices are characterized by optical spectrophotometry, performing transmittance and reflectance measurements of the completed device structure. In the previous section, it was shown that the best results came from the use of a 50 nm ZnO film as ETL and a 10 nm MoO_3 film as HTL. Two devices with these CTLs and a-Si:H absorbers with thickness of 15 and 30 nm will be used, plus an additional device with a 15 nm absorber with a first optimization including a 75 nm AZO ETL film deposited by atomic layer deposition. The *J–V* measurements under AM1.5 G illumination of these devices are presented all-together in order to compare the two relevant performance indicators in TPV: PCE and AVT (**Figure 3**; **Table 2**).

Absorbance spectra of the three devices is presented in Figure 3b. The most notable feature is that for the devices with a 15 nm a-Si:H film there is a blue-shift in the absorption onset, as compared with the device with 30 nm a-Si:H, suggesting an increase in the optical bandgap. The a-Si:H films present a reported direct bandgap of 1.8 eV in bulk, and it has also been reported to be extended up to 2.1 eV via quantum confinement, when film thickness is reduced to the nanometric scale.[46] They also present a high absorption coefficient for wavelengths with energy higher than its bandgap. A prototypical inorganic single-junction UV-TPV device should have its bandgap as close as the UV spectral onset, in order to totally avoid visible light absorption. This results in a rather natural wavelength selectivity. However, it is possible to mostly absorb UV light and some part of the blue-end spectrum with a-Si:H absorbers. By reducing the thickness to the nanometric scale, there will be frustrated absorption of visible light and hence higher transparency. However, there will still be some visible-light absorption and given the bandgap of the material, it will inevitably present some slight coloring albeit showing quite high AVT values (It is worth noting that if AVT values are >50% it is possible to implement dichroic filters in order to tune the color aspect and effectively reducing it at the cost of some AVT loss). This is observed in the absorbance spectra. For devices with 15 nm a-Si:H most of the absorption occurs below 500 nm, increasing absorption as wavelength is reduced. Same happens for the device with 30 nm a-Si:H, except that absorption is higher from 400 to 600 nm, when compared against the devices with 15 nm absorber. The devices with an optimized AZO film show higher absorption in the spectral range below 450 nm (i.e., UV/blue).

The reflectance spectra, presented in Figure 3d shows that this is attributed to an important reduction in reflectance losses within this spectral range, highlighting the need for a careful optimization of the devices in terms of optical management, as subtle changes yield notable changes in parameters such as AVT, PCE, and CRI. It is also noted that reflectance values (in the range above the absorber bandgap) are quite high, above 30%, signaling additional losses in device absorption that would not incur in reduced AVT. This is attributed to the fact that the FTO presents low roughness and thus it is expected that the nanometric films grown on top will accordingly present low roughness. Planar surfaces typically involve higher reflectance values than rough surfaces, given that optical indices of the

© 2021 The Authors. Solar RRL published by Wiley-VCH GmbH

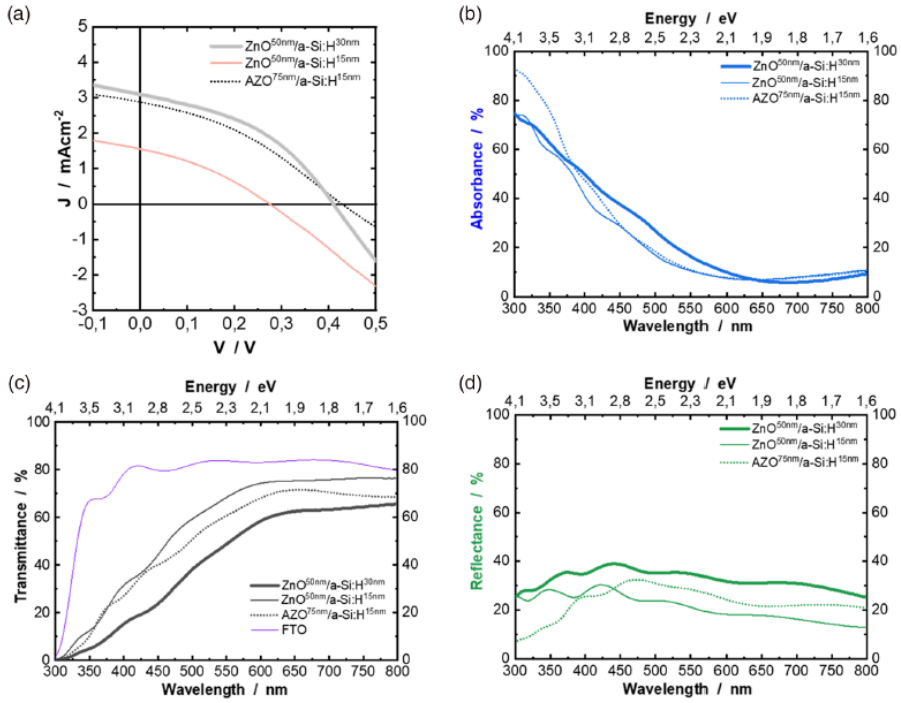

Figure 3. TPV characterization of best devices. a) *J*–*V* measurements under AM1.5G illumination of FTO/ZnO (50 nm)/a-Si:H (30 nm)/MoO_3(10 nm)/ITO, FTO/ZnO (50 nm)/a-Si:H (15 nm)/MoO_3 (10 nm)/ITO and FTO/AZO (75 nm)/a-Si:H (15 nm)/MoO_3 (10 nm)/ITO. b) Absorbance spectra of devices shown in (a). c) Transmittance spectra of the glass/FTO substrate, shown as reference, and of whole devices shown in (a). d) Reflectance spectra of devices shown in (a).

Table 2. Summary of main results with TPV parameters of fabricated devices presented in Figure 3.

TPV device structure	CRI	AVT [%]	V_{oc} [V]	J_{sc} [mAcm^{-2}]	FF [%]	PCE [%]	LUE [%]
FTO/ZnO (50 nm)/a-Si:H (15 nm)/MoO_3 (10 nm)/ITO	**89**	**69**	0.29	1.85	31.0	0.21	0.15
FTO/ZnO (50 nm)/a-Si:H (30 nm)/MoO_3 (10 nm)/ITO	74	50	0.41	**3.09**	41.4	**0.51**	**0.25**
FTO/AZO (75 nm)/a-Si:H (15 nm)/MoO_3 (10 nm)/ITO	79	62	**0.43**	2.86	**37.0**	0.41	**0.25**

materials remain unchanged. Additionally, differences seen in reflectance spectra comparing devices with 15 and 30 nm of a-Si:H are observed. This effect is very likely related to changes in optical interference for the different layer thicknesses. On the other hand, slight variations in the properties of the material could not be discarded. Reducing these reflection losses will consequently increase the device PCE in a relative percentage that is proportional to these reflection losses.

Transmittance and reflectance spectra can be used to extract the AVT and CRI of the completed devices (for detailed information on AVT and CRI see ref. [12]). Optical transmittance and reflectance of the completed devices was measured from 300 to 800 nm range to assess the transparency and visual aspect of the TPV devices. LUE is then finally calculated from multiplying AVT and PCE, in order to complete the TPV characterization. All these parameters are summarized in Table 2.

AVT values for these devices ranged from 50% to 69%. Interestingly, the AVT drastically changed in-between 15 nm a-Si:H-based devices when changing from a 50 nm ZnO film to a 75 nm AZO layer. The device with the ZnO film shows an AVT = 69%, a CRI = 89 (a^*=−0.18, b^*=21) and PCE = 0.21%, yielding a LUE = 0.15%. The device with the AZO layer shows an AVT = 62%, CRI = 79 (a^*=4, b^*=31) and PCE = 0.41%, yielding a notably higher LUE = 0.25%. This increase is basically due to the overall improved PV performance. The doped AZO layer grown by ALD yields higher FF and V_{OC}, probably due to increased doping which impacts on the increased V_{OC}. Most notably, there is a remarkable increase in J_{SC} when compared to the device with ZnO. In fact, it is almost the same as for the device with a thicker 30 nm a-Si:H absorber, suggesting a beneficial impact in both electrical and optical management. However, this increase in performance came as a

© 2021 The Authors. Solar RRL published by Wiley-VCH GmbH

reduction in AVT and more notably in CRI. The device with ZnO and a "thick" 30 nm layer presents an AVT = 50%, CRI = 74 (a^*=2.67, b^*=21), and PCE = 0.51%, yielding a LUE = 0.25%. Even though LUE is the same as for the device with a 15 nm a-Si:H film with a 75 nm AZO ETL, the visual aspect differs notably, presenting the former lower AVT and CRI values.

These results highlight that very subtle differences in device structure have much higher impact in TPV technologies compared with conventional opaque PV. This is caused by the inevitable trade-off between efficiency and transparency, with the add-on of visual aspect. It is concluded that depending on the specific application requirements and constraints, different devices could be selected if given a catalogue showing these three devices. For example, for low power applications with a high demand on color-neutrality and high transparency the device with lower LUE with high CRI and AVT may be adequate, as constraint is more pressing on visual aspect. This remarks also that when working with transparent technologies with bandgaps that lie within the visible range, like in this case, it is relevant to present, if possible, devices with different ratio AVT/PCE, to test the limits of a given TPV technology in terms of the trade-off AVT/PCE (i.e., highest PCE with lower AVT and highest AVT at cost of reduced PCE).

Finally, when assessing the photovoltaic parameters extracted from the *J–V* measurements (see Figure 3a and Table 2), different conclusions can be observed. First, comparing the devices with a 15 nm a-Si:H absorber, we see that the optimized AZO film leads to an overall improvement. Notably, FF increases from 31 to 41.4% when switching the ZnO film by an AZO film, a relative increase of 20%. J_{SC} increases from 1.85 to 2.86 mA cm^{-2}, a relative increase of 55% without changing the absorber thickness. In terms of V_{OC}, a relative increase of 48% is observed, going from 0.29 to 0.43 V (even higher than for the device with an absorber thickness of 30 nm). An antireflective coating in the UV/blue range would further increase the PCE by increasing absorption in this spectral range.

3. Conclusion

We have studied the potential use of ultrathin intrinsic a-Si:H as a potential wavelength-selective absorber for inorganic TPV applications in a device architecture including highly transparent metal-oxide carrier selective contacts and using transparent conductive oxides as electrical contacts. We have shown that ZnO acts as ETL and MoO_3 as HTL, and the impact of the thickness of the different layers in the device architecture has been analyzed, showing the possibility to achieve devices with values of AVT in the range from 50% to 69% and AM1.5G power conversion efficiencies up to 0.5%, corresponding to LUE values up to 0.25%. We have shown that by using an ultrathin a-Si absorber layer devices are engineered to allow for wavelength selectivity in the UV to blue wavelength ranges, with the existence of a trade-off behavior between PCE and AVT with the a-Si layer thickness. On the other hand, replacement of the ZnO CTL by AZO layers leads to a relevant improvement of the optoelectronic characteristics of the devices when compared with solar cells with similar a-Si absorber thickness. Estimation of the device parameters using FTO/AZO/a-Si/MoO_3/ITO optimized architectures gives expected efficiency values higher than 1%, with a relevant improvement in relation to state-of-the-art devices. Future optimizations may involve the use of alternative (doped) metal-oxides such as TiO_2 and/or dipole layers such as LiF as ETL. These structures show a promising route for alternative applications and as a ubiquitous power source for low-power devices that can effectively extend the range of applications within the photovoltaic area. In order to increase PCE it becomes relevant to perform an in-depth characterization of interfaces, as they might be critical in efficiency, especially for such an ultrathin inorganic nanodevice (around 100 nm, excluding TCO electrical contacts). The benefit is that by carefully tuning these interfaces there will not be any impact in the visual aspect of the TPV device, which is a parameter of utmost importance. An added benefit of these devices are that all materials and processes are scalable and compatible with existing and established industries, using earth-abundant, stable, and low-cost materials.

4. Experimental Section

Sample Preparation: The solar cells fabricated in this work present the structure Glass/FTO/ZnO/a-Si:H (15, 30 nm)/MoO_3/ITO. Commercial glass/FTO substrates (Merck; R_{sh} = 13 Ωsq^{-1}, AVT = 83%, thickness of 250 nm) were used as substrate and transparent back-contact for the solar cell devices. Prior to deposition, substrates were first rinsed in distilled water, dried in Ar flux and afterward cleaned by subsequent baths in isopropanol and milli-Q H_2O in an ultrasonic bath at room temperature for 10 min each and then were dried with Ar flux. Finally, they were subjected to a 5 min ozone treatment. ZnO films were deposited by DC-Pulsed Magnetron Sputtering (Alliance CT-100). Prior to deposition the chamber was evacuated at 10^{-7} mbar. The ZnO target (Neyco; 4N) was presputtered to remove any surface contaminants with the shutter in closed configuration. The deposition took place at room temperature with no intentional heating at a working pressure of 3×10^{-3} mbar in Ar atmosphere at 40 sccm, applying a DC power density of 1.8 W cm^{-2} to the target. Afterward, intrinsic a-Si:H ultrathin films of either 15 or 30 nm were deposited by PE-CVD (Elettrorava) with an RF power supply of 13.56 MHz at 6 W and at 400 °C (measured substrate temperature at around 200 °C) with a mix of SiH_4 and CH_4 at 36 and 12 sccm, respectively. The deposition time was 2 and 4 min for the a-Si:H films of 15 and 30 nm, respectively. MoO_3 films were deposited by thermal evaporation (Oerlikon Univex 250). MoO_3 powder (Alfa Aesar; 99.995%) was used as evaporant in a tungsten boat. The chamber was evacuated at a base pressure of 10^{-6} mbar before evaporation and the deposition took place at room temperature, with no intentional heating, at a rate of 0.5 Å s^{-1} measured with a quartz crystal microbalance (Inficon SQC-310; Ag 6 MHz sensor). To complete the device, a 190 nm-thick ITO film was deposited by DC-Pulsed Magnetron Sputtering (Alliance CT-100). Prior to deposition the chamber was evacuated at 10^{-7} mbar and the substrate was heated up to 200 °C. The ITO target (Neyco; In_2O_3/SnO_2 90/10 wt%, 4 N) was presputtered to remove any surface contaminants with the shutter in closed configuration. The deposition took place at 200 °C (nominal) at a working pressure of 3 pu10^{-3} mbar in a mixed Ar/O_2 atmosphere at 30/0.5 sccm, applying a DC power density of 1.9 W cm^{-2} to the target. For the optimized device with an AZO ETL, a 75 nm film was grown in an ALD system (Savannah S200, Cambridge Nanotech) at 135 °C. The precursors used are diethylzinc (DEZ), ultrapure H_2O and trimethylaluminum (TMA) and using N_2 as purging gas, with a DEZ:TMA ratio of 19:1. 21 supercycles were performed with 19 $H_2O/N_2/DEZ/N_2$ (20 ms/3 s/15 ms/3 s) cycles and 1 $H_2O/N_2/TMA/N_2$ (50 ms/1 s/20 ms/5 s) cycle.

Characterization: UV–vis measurements were acquired with a dual-beam spectrophotometer setup (Perkin Elmer Lambda L950) in transmittance and in reflectance modes (with an integrating sphere) from 300 to 800 nm.

© 2021 The Authors. Solar RRL published by Wiley-VCH GmbH

J–V (current density–voltage) measurements under illumination were carried out using a AAA solar simulator with AM1.5G illumination calibrated using a NREL-certified Si reference solar cell (Abet Technologies Model 15150). Electrical measurements were carried out with a source-measure unit (Keithley SMU 2400) in four-wire sense mode, controlled by the software Tracer (ReRa solutions) using a IEEE 488 GPIB Instrument Control Device (National Instruments GPIB-USB-HS). For these optoelectronic measurements, the sample was measured with a mask and has been placed in a dark opaque matt in order to avoid any back-reflections that could alter the characterization of the transparent solar cells.

Acknowledgements

This work has received funding from the European Union H2020 Framework Programme under Grant Agreement no. 826002 (Tech4Win). This work is also part of the R+D+i MaterOne projects (Refs. PID 2020-116719RB-C42 and PID 2020-116719RB-C41) and of the R+D+i SCALED project (Ref. PID 2019-109215RB-C4) funded by MCIN/AEI/10.13039/5011000110033. Authors from IREC and Universitat de Barcelona belong to the SEMS (Solar Energy Materials and Systems) Consolidated Research Group of the "Generalitat de Catalunya" (Ref. 2017 SGR 862).

Conflict of Interest

The authors declare no conflict of interest.

Data Availability Statement

The data that support the findings of this study are openly available in https://zenodo.org/record/5744929#.YaZMzsfMI2w.

Keywords

a-Si, oxides, selective contacts, transparent photovoltaics, UV-selective solar cells

Received: November 1, 2021
Revised: November 18, 2021
Published online: December 3, 2021

[1] A. Pérez-Rodríguez, presented in *NEXTGEN '19: 2019 Next Generation High Efficiency Photovoltaics Inter. School and Workshop*, Mallorca, October **2019**.
[2] P. Heinstein, C. Ballif, L.-E. Perret-Aebi, *Green* **2013**, *3*, 125.
[3] F. J. W. Osseweijer, L. B. P. van den Hurk, E. J. H. M. Teunissen, W. G. J. H. M. van Sark, *Renew. Sustain. Energy Rev.* **2018**, *90*, 1027.
[4] E. Biyik, M. Araz, A. Hepbasli, M. Shahrestani, R. Yao, L. Shao, E. Essah, A. C. Oliveira, T. del Caño, E. Rico, J. L. Lechón, L. Andrade, A. Mendes, Y. B. Atlı, *Eng. Sci. Technol. an Int. J.* **2017**, *20*, 833.
[5] K. Lee, H. D. Um, D. Choi, J. Park, N. Kim, H. Kim, K. Seo, *Cell Rep. Phys. Sci.* **2020**, *1*, 100143.
[6] E. P. Thompson, E. L. Bombelli, S. Shubham, H. Watson, A. Everard, V. D'Ardes, A. Schievano, S. Bocchi, N. Zand, C. J. Howe, P. Bombelli, *Adv. Energy Mater.* **2020**, *10*, 2001189.
[7] S. Schindele, M. Trommsdorff, A. Schlaak, T. Obergfell, G. Bopp, C. Reise, C. Braun, A. Weselek, A. Bauerle, P. Högy, A. Goetzberger, E. Weber, *Appl. Energy* **2020**, *265*, 114737.
[8] A. Agostini, M. Colauzzi, S. Amaducci, *Appl. Energy* **2021**, *281*, 116102.
[9] A. Brodu, C. Seydoux, G. Finazzi, C. Dublanche-Tixier, C. Ducros, *Thin Solid Films* **2019**, *689*, 137492.
[10] G. Kim, J. W. Lim, J. Kim, S. J. Yun, M. A. Park, *ACS Appl. Mater. Interfaces* **2020**, *12*, 27122.
[11] X. Lin, Y.-L. Loo, M. Sezen-Edmonds, N. C. Davy, J. Gao, A. Liu, A. Kahn, N. Yao, *Nat. Energy* **2017**, *2*, 17104.
[12] C. J. Traverse, R. Pandey, M. C. Barr, R. R. Lunt, *Nat. Energy* **2017**, *2*, 849.
[13] F. Grifoni, M. Bonomo, W. Naim, N. Barbero, T. Alnasser, I. Dzeba, M. Giordano, A. Tsaturyan, M. Urbani, T. Torres, C. Barolo, F. Sauvage, *Adv. Energy Mater.* **2021**, 2101598.
[14] Q. Xue, R. Xia, C. J. Brabec, H. L. Yip, *Energy Environ. Sci.* **2018**, *11*, 1688.
[15] D. K. Ban, M. Patel, T. T. Nguyen, J. Kim, *Adv. Electron. Mater.* **2019**, *5*, 1.
[16] M. Patel, H. S. Kim, J. Kim, J. H. Yun, S. J. Kim, E. H. Choi, H. H. Park, *Sol. Energy Mater. Sol. Cells* **2017**, *170*, 246.
[17] R. Karsthof, P. Räcke, H. Von Wenckstern, M. Grundmann, *Phys. Status Solidi* **2016**, *213*, 30.
[18] R. Karsthof, H. von Wenckstern, M. Grundmann, *J. Vac. Sci. Technol. B, Nanotechnol. Microelectron. Mater. Process. Meas. Phenom.* **2016**, *34*, 04J107.
[19] A. J. Lopez-Garcia, A. Bauer, R. Fonoll Rubio, D. Payno, Z. Jehl Li-Kao, S. Kazim, D. Hariskos, V. Izquierdo-Roca, E. Saucedo, A. Pérez-Rodríguez, *Sol. RRL* **2020**, *4*, 2000470.
[20] S. Kim, M. Patel, T. T. Nguyen, J. Yi, C. P. Wong, J. Kim, *Nano Energy* **2020**, *77*, 105090.
[21] J. Ramanujam, D. M. Bishop, T. K. Todorov, O. Gunawan, J. Rath, R. Nekovei, E. Artegiani, A. Romeo, *Prog. Mater. Sci.* **2020**, *110*, 100619.
[22] L. G. Gerling, S. Mahato, A. Morales-Vilches, G. Masmitja, P. Ortega, C. Voz, R. Alcubilla, J. Puigdollers, *Sol. Energy Mater. Sol. Cells* **2016**, *145*, 109.
[23] L. Fang, S. J. Baik, K. S. Lim, *Thin Solid Films* **2014**, *556*, 515.
[24] J. Ding, Y. Zhou, G. Dong, M. Liu, D. Yu, F. Liu, *Prog. Photovolt. Res. Appl.* **2018**, *26*, 974.
[25] D. E. Carlson, C. R. Wronski, *Appl. Phys. Lett.* **1976**, *28*, 671.
[26] T. Matsui, A. Bidiville, K. Maejima, H. Sai, T. Koida, T. Suezaki, M. Matsumoto, K. Saito, I. Yoshida, M. Kondo, *Appl. Phys. Lett.* **2015**, *106*, 053901.
[27] K. Fukutani, M. Kanbe, W. Futako, B. Kaplan, T. Kamiya, C. Fortmann, I. Shimizu, *J. Non. Cryst. Solids* **1998**, *227–230*, 63.
[28] A. S. Ferlauto, G. M. Ferreira, J. M. Pearce, C. R. Wronski, R. W. Collins, X. Deng, G. Ganguly, *J. Appl. Phys.* **2002**, *92*, 2424.
[29] G. E. Jellison, F. A. Modine, *Appl. Phys. Lett.* **1996**, *69*, 371.
[30] E. A. Schiff, R. I. Devlen, H. T. Grahn, J. Tauc, S. Guha, *Appl. Phys. Lett.* **1989**, *54*, 1911.
[31] E. Schiff, *Sol. Energy Mater. Sol. Cells* **2003**, *78*, 567.
[32] E. A. Schiff, *J. Non. Cryst. Solids* **2006**, *352*, 1087.
[33] A. Froitzheim, K. Brendel, L. Elstner, W. Fuhs, K. Kliefoth, M. Schmidt, *J. Non. Cryst. Solids* **2002**, *299–302*, 663.
[34] A. Gusain, R. M. Faria, P. B. Miranda, *Front. Chem.* **2019**, *7*, 61.
[35] W. Tress, K. Leo, M. Riede, *Phys. Rev. B* **2012**, *85*, 155201.
[36] W. Tress, O. Inganäs, *Sol. Energy Mater. Sol. Cells* **2013**, *117*, 599.
[37] A. Wagenpfahl, D. Rauh, M. Binder, C. Deibel, V. Dyakonov, *Phys. Rev. B - Condens. Matter Mater. Phys.* **2010**, *82*, 1.
[38] W. Tress, K. Leo, M. Riede, *Adv. Funct. Mater.* **2011**, *21*, 2140.

© 2021 The Authors. Solar RRL published by Wiley-VCH GmbH

[39] R. Saive, *IEEE J. Photovolt.* **2019**, *9*, 1477.
[40] J. Meyer, A. Shu, M. Kröger, A. Kahn, *Appl. Phys. Lett.* **2010**, *96*, 133308.
[41] Irfan, H. Ding, Y. Gao, C. Small, D. Y. Kim, J. Subbiah, F. So, *Appl. Phys. Lett.* **2010**, *96*, 243307.
[42] C. Liu, M. Cai, Y. Yang, Z. Arain, Y. Ding, X. Shi, P. Shi, S. Ma, T. Hayat, A. Alsaedi, J. Wu, S. Dai, G. Cao, *J. Mater. Chem. A* **2019**, *7*, 11086.
[43] M. Kröger, S. Hamwi, J. Meyer, T. Riedl, W. Kowalsky, A. Kahn, *Appl. Phys. Lett.* **2009**, *95*, 123301.
[44] Y. Guo, J. Robertson, *Appl. Phys. Lett.* **2014**, *105*, 222110.
[45] R. García-Hernansanz, E. García-Hemme, D. Montero, J. Olea, A. del Prado, I. Mártil, C. Voz, L. G. Gerling, J. Puigdollers, R. Alcubilla, *Sol. Energy Mater. Sol. Cells* **2018**, *185*, 61.
[46] Y. Abdulraheem, I. Gordon, T. Bearda, H. Meddeb, J. Poortmans, *AIP Adv.* **2014**, *4*, 057122.

© 2021 The Authors. Solar RRL published by Wiley-VCH GmbH

3.4 – Third research article

Solar RRL
www.solar-rrl.com

Ultrathin a-Si:H/Oxide Transparent Solar Cells Exhibiting UV-Blue Selective-Like Absorption

Alex J. Lopez-Garcia, Cristobal Voz, Jose Miguel Asensi, Joaquim Puigdollers, Víctor Izquierdo-Roca, and Alejandro Pérez-Rodríguez*

Herein, the fabrication of transparent solar cells based on nanometric (8 and 30 nm) intrinsic hydrogenated amorphous silicon films (a-Si:H) and using oxide thin films as transparent carrier selective contacts are reported. The ultrathin devices present photovoltaic effect and high average visible transmittance (AVT). Additionally, they display a shifted spectral response toward short wavelengths. Glass/fluorine-doped tin oxide (FTO)/aluminum-doped zinc oxide (AZO)/a-Si:H/MoO_3/indium tin oxide (ITO) prototypes are shown, presenting AVT = 35% and photovoltaic conversion efficiency (PCE) = 2% for a device with a 30 nm a-Si:H film. This yields a light utilization efficiency (LUE) of 0.7%, a record up to this date for inorganic oxide-based transparent solar cells. For devices including an 8 nm a-Si:H film, the AVT reaches 66% with a PCE = 0.6% (LUE = 0.4%). These high AVT values are comparable or even superior in some cases to those achieved for pure oxide devices. These findings confirm the potential of the proposed architectures for the development of highly transparent energy harvesters as functional components in building-integrated photovoltaics (BIPV), agrophotovoltaics (APV), sensors and other low-power devices. In addition, these devices are fabricated with earth-abundant materials and with up-scalable techniques that can allow for a feasible implementation.

1. Introduction

Up to this date, the photovoltaic (PV) landscape shows a clear dependency on first-generation c-Si solar modules (and some second-generation thin-film technologies such as CdTe or copper indium gallium sulfide (CIGS)), with a clear aim toward high-efficiency and high-power production. As so, the implementation of such renewable energy sources has been focused on the deployment of solar farms. In the last decades, overall costs have greatly decreased and in many countries, applications of tariffs have allowed for an even further decrease in costs, allowing the solar technologies to span toward everyday user consumption. Examples of these are typical rooftop installations at home that allow users to auto-consume by having on-site energy generation.[1]

One of the key disadvantages of commercial PV technologies is that their implementation and output power are surface area dependent, among other issues such as high weight, use of relatively large amounts of critical raw materials, and in some cases toxic precursors. This poses an important limitation for conventional PV as many surfaces that are available (e.g., in buildings' façades) cannot be exploited by such technologies. Additionally, in constructions and utilities, there is also a demand to keep certain aesthetics of the surfaces or grazing elements that brings additional limitations for massive and decentralized deployment of solar technologies. To be able to use the available surfaces of façades, sensors, windows, or shading elements (amongst others) for ubiquitous on-site power generation and to allow for distributed applications, it is important to develop alternative concepts.

Transparent photovoltaic (TPV) is a clear example of how the field of PVs is shifting toward this goal to expand the deployment of PV technologies and to increase the clean-energy share of the energy mix. TPV technologies rely on absorption of UV and/or IR light, while avoiding visible range absorption completely or as

A. J. Lopez-Garcia, V. Izquierdo-Roca, A. Pérez-Rodríguez
Institut de Recerca en Energia de Catalunya (IREC)
Jardins de les Dones de Negre, 1, 2ª pl, Sant Adrià del Besòs, 08930 Barcelona, Spain
E-mail: alopez@irec.cat

The ORCID identification number(s) for the author(s) of this article can be found under https://doi.org/10.1002/solr.202200928.

© 2023 The Authors. Solar RRL published by Wiley-VCH GmbH. This is an open access article under the terms of the Creative Commons Attribution-NonCommercial-NoDerivs License, which permits use and distribution in any medium, provided the original work is properly cited, the use is non-commercial and no modifications or adaptations are made.

DOI: 10.1002/solr.202200928

C. Voz, J. Puigdollers
Departament Enginyeria Electrònica
Universitat Politècnica Catalunya
c/Jordi Girona 3-1, 08034 Barcelona, Spain

J. M. Asensi
IN2UB
Departament de Física Aplicada
Universitat de Barcelona
Carrer de Martí i Franquès 1, 08028 Barcelona, Spain

A. Pérez-Rodríguez
IN2UB
Departament d'Enginyeria Electrònica i Biomèdica
Universitat de Barcelona
Carrer de Martí i Franquès 1, 08028 Barcelona, Spain

much as possible (selective and nonselective approaches).[2,3] These device concepts can potentially allow for nonintrusive implementation of transparent solar devices, as they will be essentially transparent to the human eye due to negligible absorption/emission of visible light, while harvesting wavelengths to which the human eye is blind.

Among the different approaches, inorganic technologies based on the use of oxide and chalcogenide materials have a strong interest because they are based on the use of stable, inexpensive, and earth-abundant materials that have a strong compatibility with industrial processes. Oxide materials for example have been extensively studied as UV-selective absorbers due to their wide bandgaps, and absorption onset close to the UV onset. This property leads to potentially highly transparent and color-neutral devices that exploit the UV photons of the solar spectra. Indeed, very high average visible transmission (AVT) values have been obtained with oxide-based transparent solar cells. (AVT is the measurement of how much light in the eye's photopic range is transmitted. Colour rendering index (CRI) is a measure, with values ranging from 0 to 100, of how well the color of an object is reproduced by comparing to a reference. Detailed descriptions of AVT and CRI and their relevance for TPV can be found in Refs. [2,4]). However, these devices have only achieved efficiencies of around 0.5% for the AM1.5G solar spectra limited by a low light utilization efficiency (LUE) value.[5–8] This parameter has been proposed in Ref. [2] as a relevant figure of merit for TPV technologies, and is defined by the product of the AVT and the photovoltaic conversion efficiency (PCE). Recently, new published works have shown that by embedding ultrathin a-Si:H layers in oxide-based devices, it was possible to increase significantly the PCE while maintaining high AVT and CRI values.[9–15]

In this work, transparent PV cells based on ultrathin intrinsic a-Si:H and oxide-based charge-transport layers (CTLs) are presented. The a-Si:H films have been studied in detail via optical characterization techniques including photothermal deflection spectroscopy (PDS) as well as UV–visible–near infrared (NIR) spectrophotometry. These techniques combined have allowed for a precise determination of the optical indices and absorption coefficient of the nanometric films. Full devices are presented afterward, showing record PCE and LUE values for this kind of TPV architecture. It is also shown that the performance of the TPV devices (in terms of AVT and PCE) can be tuned by subtle variation in the nanometric thickness of the a-Si:H film. Spectral response measurements confirmed that the devices preferentially absorb short wavelengths (i.e., $\lambda < 450$ nm) due to the ultrathin nature of the a-Si:H films, which frustrates most of the longer wavelength absorption. This is the desired behavior in this technology to enhance the transparency and aesthetic aspects of the TPV device.

2. Results and Discussion

In this work, TPV devices composed of planar inorganic ultrathin films have been fabricated using an architecture consisting of the intrinsic a-Si:H film coupled to oxide carrier-selective contacts at opposite interfaces (i.e., soda-lime glass (SLG)/fluorine-doped tin oxide (FTO)/ETL/a-Si:H/HTL/indium tin oxide (ITO)). FTO and ITO act as transparent electrodes and the nanometric intrinsic a-Si:H film works as the absorber layer. Aluminum-doped zinc oxide (AZO, 75 nm) is used as electron-transport layer (ETL) while molybdenum oxide (MoO_3, 10 nm) acts as the hole-transport layer (HTL). These transport layers allow for the extraction of electrons at the FTO electrode (cathode) and holes at the ITO electrode (anode), respectively (**Figure 1**). Both selective contacts, AZO and MoO_3, present wide bandgaps above 3.2 eV, thus greatly reducing unwanted parasitic absorption and allowing for increased transparency. Two different thicknesses of a-Si:H have been studied, 8 and 30 nm. Although the device structure does not use doped a-Si:H layers, its working mechanism is similar to a conventional p–*i*–n junction. In this sense, photogenerated carriers are collected first thanks to the electric field within the intrinsic layer and then filtered at the interfaces by the respective CTLs. In doping-free devices like these, the internal electric field builds on the different work function of the respective selective contacts.

We begin by analyzing the optical properties of the ultrathin a-Si:H films grown on quartz substrates and follow with a detailed optoelectronic characterization of the best prototype devices to extract the relevant TPV performance metrics (i.e., PCE, AVT, CRI, LUE) and to discuss the working mechanisms and features of these transparent devices.

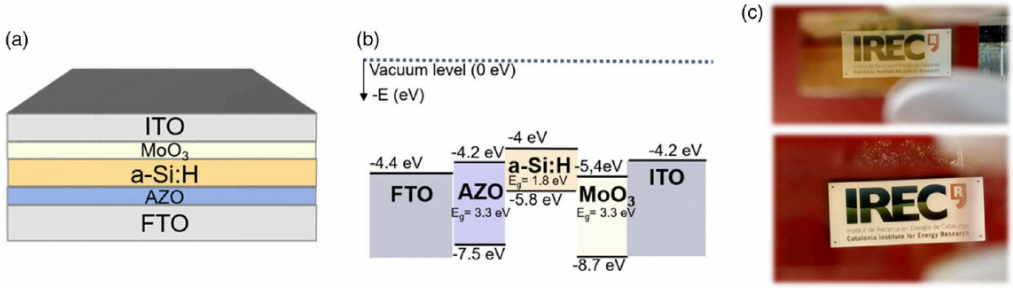

Figure 1. a) Schematic illustration of the transparent photovoltaic (TPV) device architecture (not to scale). b) Band diagram of the different films that conform the full device. c) Pictures of full (top) 30 nm device and (bottom) the 8 nm device, taken outdoors in broad daylight. The picture shows the TPV device, showing a white board with the IREC logo located at the building entrance.

© 2023 The Authors. Solar RRL published by Wiley-VCH GmbH

2.1. Optical Characterization of Ultrathin a-Si:H Films

A prototypical inorganic UV–TPV device should ideally have its bandgap matched to the UV spectral onset (i.e., >2.8 eV), to neglect absorption of visible radiation. This equates to a rather natural wavelength selectivity toward UV harvesting. However, by using extremely thin absorbers with wide bandgap (as the case for a-Si:H), it is possible to mostly absorb UV light and some part of the blue-end spectral range. This occurs due to frustrated absorption engineered through the nanometric thickness, which simultaneously allows for higher transparency. However, devices will present some color even at high AVT values. If this is the case, it is possible to color tune the device to render it as color neutral as possible, for example, with interferometric filters or optical coatings.

Intrinsic a-Si:H films present a direct bandgap usually reported at values around 1.7–1.8 eV. It has also been reported to be extended up to 2.1 eV via quantum confinement, when thickness is reduced to the nanometric scale.[16] Additionally, previous work had shown that devices with 15 nm a-Si:H films presented a blueshifted absorption spectra, as compared to devices with 30 nm. This suggests a possible modification in the bandgap of a-Si:H in this thickness range.[10]

The PDS technique allows for an accurate measurement of the optical absorption in ultrathin a-Si:H films, which can confirm if there is any change in the bandgap as thickness is decreased. Together with spectrophotometry data, it also allows calculation of the optical bandgap and the Urbach. In this section, results on the characterization of a-Si:H ultrathin films are presented. For this, films of two different thicknesses have been assessed, corresponding to 8 and 30 nm (same as for the complete TPV devices). The a-Si:H films have been grown on quartz substrates, which have a flat transmittance profile within the UV–visible–NIR range.

Disordered and low crystallinity materials usually present band tails in the density of states that extend into the sub-band gap region, corresponding to localized states referred as Urbach front or Urbach tail.[17] These band tails are characterized by the Urbach energy (E_U), which can be interpreted as a measure of disorder in the material. The higher this value, the higher density of these states, which relates to poor semiconductor quality such as low lifetime and can have a strong impact in open-circuit voltage (V_{oc}).[18] PDS allows for an accurate determination of this value. **Figure 2** shows the experimental absorption coefficient for both a-Si:H films (8 and 30 nm). The absorption coefficient of the films exceeds 10^5 for wavelengths above 2.5 eV. Additionally, a sub-band gap contribution, below 1.7 eV, is observed in both cases. This sub-band gap contribution could be related to recombination dynamics in the material and localized surface defect states (see Supporting Information). From the experimental absorption coefficient values $\alpha(E)$ and using the Cody optical model, the value of the optical bandgap can be calculated with great precision.[19,20] In both cases, the optical value was found to be of 1.69 and 1.71 eV for the 8 and the 30 nm film, respectively (**Table 1**). This value indicates that at these nanometric thickness values, the bandgap still behaves "classically" and there is no indication of any shift in the bandgap due to quantum confinement.

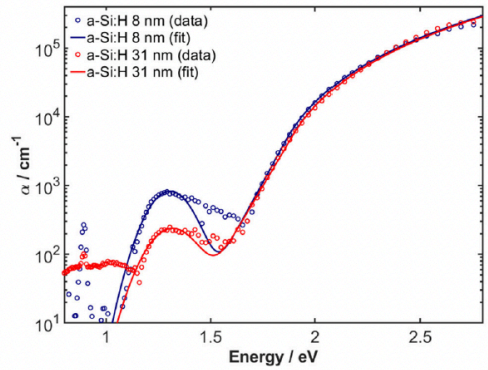

Figure 2. Absorption coefficient of a-Si:H films of 8 and 30 nm extracted from photothermal deflection spectroscopy (PDS) measurements. Solid circles are the experimental values, and solid lines are the fit to the model described in Supporting Information by Equations S(1), S(2), and S(3) (see also Figure S1 and Table S1 in Supporting Information).

Table 1. Summary of parameters extracted from PDS measurements on a-Si:H films of 8 and 30 nm. The optical bandgap (E_g) the Urbach energy (E_u) for both films are presented.

Sample	α(2.5 eV) [cm^{-1}]	E_g [eV]	E_U [meV]
Quartz/a-Si:H (8 nm)	1.22×10^5	1.69	78
Quartz/a-Si:H (30 nm)	1.48×10^5	1.71	84

To extract the numerical value for the Urbach energy, Equation (1) is used, where α_0 and U_1 are constants determined through fitting the data from $\alpha(E)$, h is Planck's constant and ν is the frequency of the incident radiation. Thus, plotting $\ln(\alpha)$ as a function of energy and calculating the inverse of the slope yield the sought value for the Urbach energy E_U

$$\alpha(h\nu) = \alpha_0 \cdot e^{\left(\frac{h\nu - U_1}{E_U}\right)} \quad (1)$$

The Urbach energy was calculated for both a-Si:H film thicknesses, yielding a similar value of around 80 meV. This value is relatively higher than the 50 meV typically measured in thick (200–300 nm) state-of-the-art a-Si:H films.[21,22] This can be explained considering the higher contribution of surface states in the ultrathin a-Si:H layers. A higher E_U value can introduce some V_{oc} loss, which makes interface passivation an important aspect to improve TPV devices.

2.2. Optical Characteristics and *J–V* Characteristics of a-Si:H/Oxide TPV Devices

In this section, complete device structures are characterized by measuring their transmittance by optical spectrophotometry. Complete devices were fabricated with two sets of samples, including 8 and 30 nm a-Si:H absorber layers while leaving the rest of the structure unchanged (i.e., AZO and MoO_3 fixed

© 2023 The Authors. Solar RRL published by Wiley-VCH GmbH

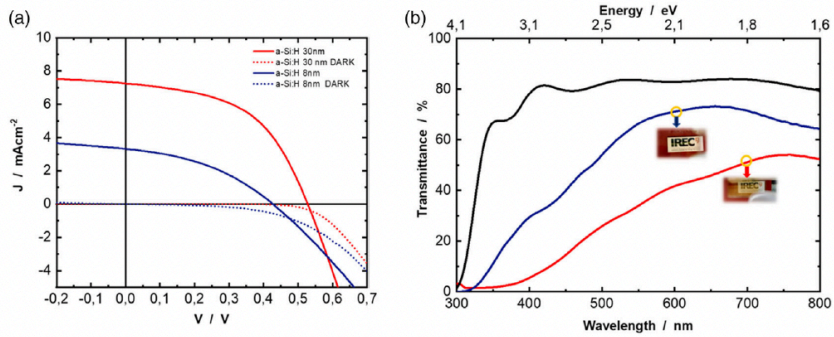

Figure 3. TPV characterization of best devices. a) Current voltage–density (J–V) characteristics measured under AM1.5G illumination of SLG/FTO/AZO(75 nm)/a-Si:H(8, 30 nm)/MoO_3(10 nm)/ITO. b) Transmittance spectra of devices shown in (a). Transmittance of the SLG/FTO substrate is shown as reference (black curve).

to 75 and 10 nm, respectively). These measurements allow for the determination of the transmittance spectra of the complete TPV devices, which will serve as input for the calculation of the TPV figures of merit of AVT and CRI. Afterward, the study of the current density–voltage (J–V) characteristics measured in dark and under AM1.5G illumination is presented.

Figure 3 presents the transmittance spectra from 300 to 800 nm of the complete devices extracted from the spectrophotometry measurements. The SLG/FTO substrate transmittance is also presented as a reference. For both a-Si:H thicknesses, the transmittance in the visible range is quite high, showing an expected increase in transmittance for the sample with a thinner 8 nm a-Si:H layer. From these spectra, the AVT and CRI figures of merit are calculated (**Table 2**). The AVT parameter weighs in the photopic response of the human eye, which sensitivity is centered around the green (550 nm). A notable difference between both samples is observed when calculating the AVT and CRI values, showing the possibility of tuning the aesthetics of the device with changes in the thickness of the a-Si:H layer. The thinner device (8 nm) presents a very high value of AVT = 66%, in fact the highest AVT reported so far for these materials and architecture, and comparable to reported UV selective TPV pure oxide devices.[8–10] The AVT values drop to AVT = 35.4% for the thicker devices (30 nm), though still being quite transparent. As for the CRI parameter, the thinner devices present again higher values. For the 8 nm device, the CRI is as high as CRI = 85, while for the 30 nm case, it shows a value of CRI = 75 resulting in a less color-neutral device. Another notable feature is the UV filtering capabilities of these devices, which is convenient to eliminate unwanted and potentially harmful wavelengths. This added functionality is especially interesting, for example, in smart window applications that include an IR selective organic solar cell in addition to the UV–blue selective device, leading to a tandem-like device architecture.[23] In this device architecture, filtering of the UV radiation by the inorganic top cell is relevant to prevent potential degradation of the bottom IR organic cell.

Table 2. Summary of results with TPV parameters of fabricated devices presented in Figure 3.

TPV device architecture	CRI	AVT [%]	V_{oc} [V]	J_{sc} [mAcm^{-2}]	FF [%]	PCE [%]	LUE [%]
FTO/AZO/a-Si:H(8 nm)/MoO_3/ITO	87	66.0	0.427	3.30	39.4	0.56	0.4
FTO/AZO/a-Si:H(30 nm)/MoO_3/ITO	75	35.4	0.528	7.24	51.0	1.95	0.7

The device with 30 nm a-Si:H layer absorbs almost all the UV radiation evidencing excellent UV-filtering capabilities. However, the 8 nm device is less efficient at this task and still transmits a noticeable amount of this radiation. Absorption in this UV region increases exponentially with the thickness of the a-Si:H layer.

Resuming with the optoelectronic characterization, J–V characteristics in dark and under AM1.5G illumination of the best devices are presented in Figure 3 and PV parameters are presented in Table 2. Statistics on the devices are presented in Figure S2, Supporting Information, presenting box plots of the devices with either a-Si:H film thickness. Measurements were made from −0.2 to 0.7 V, thus including the three quadrants. No hysteresis in the electrical characteristics was observed either sweeping from negative to positive potential or vice versa. The 30 nm device presents a PCE of 1.95% while the 8 nm film presents a still remarkable PCE = 0.56% for a TPV device. This is the highest PCE value reported so far for oxide-based TPV devices. In general, there is an overall improvement in all PV parameters for the 30 nm device as compared to the 8 nm one. In terms of J_{sc}, its value is more than doubled, which can be clearly associated to the increased absorption and subsequent photogeneration. Both the FF and V_{oc} values are also significantly higher for the 30 nm device. The relative increase in FF for the 30 nm device is thought to come from the increased photocurrent, which brings the solar cell to an operation point less influenced by parasitic resistances. The V_{oc} of 0.528 V for the thick device is also

© 2023 The Authors. Solar RRL published by Wiley-VCH GmbH

significantly higher compared to the $V_{OC} = 0.427$ V measured for the 8 nm device. It is worth noting that a V_{oc} deficit is observed in both devices, since state-of-the-art a-Si:H p–*i*–n solar cells have reached values of around 0.9 V.[24–26] Such deficit of V_{oc} is quite important and hence constitutes an aspect to tackle to increase the potential of these TPV devices. For instance, interface recombination losses are expected to be much more relevant for ultrathin PV devices. Additionally, in this work, we use transparent oxide-based selective contacts replacing the highly doped layers of traditional p–*i*–n a-Si:H solar cells. The V_{oc} value finally results from the quasi-Fermi level splitting (QFLS) at the opposite interfaces (selective contacts). If the work functions of the respective selective contacts are misaligned with respect to the conduction and valence bands of the a-Si:H layer, a transport barrier will be created and will lead to QFLS reduction and hence of V_{oc}. With this in mind, finding suitable selective contacts that are optically transparent in the targeted absorption range is very important for improving the overall performance of these devices.

In contrast, when comparing the *J*–*V* characteristics in dark versus under AM1.5G illumination, a cross-over effect is observed in both types of device. This effect has been ascribed either to the presence of a light-dependent barrier or to changes in conductivity of the a-Si:H (i.e., increased photocon ductivity).[27] To deepen in the knowledge of the potential loss mechanisms of the TPV devices, the *J*–*V* curves have been fitted using the 1-diode model for a solar cell equivalent circuit, using the "2–3 diode fit" software.[28,29] The extracted parameters from the fitting are shown in Table S3, Supporting Information. The 30 nm device presents a high shunt resistance value in the order of 10^4 Ωcm^2 confirming high conformality of the films across the device and the absence of relevant shunting paths. On the contrary, for the device with an 8 nm thick a-Si:H layer, the shunt resistance is one order of magnitude less, around 10^3 Ωcm^2. This suggests in this case a poorer level of conformality and coverage of the nanometric layers in the device architecture. When looking at the series resistance values, the results are in the same order of magnitude, yet still higher for the 8 nm device (11 Ωcm^2 for the 30 nm device and 41 Ωcm^2 for the 8 nm device). The relatively high series resistance most probably comes from the wide-bandgap oxide hole-selective contact and the resistance of the TCOs used as transparent electrodes. As for the ideality factor, the values obtained in both types of devices are close or slightly above 2, suggesting that the main recombination pathways are associated to interface recombination. This agrees with the ultrathin nature of the films, as bulk recombination losses are not expected in such device architectures. These results again highlight the relevance of the interfaces in the device performance.[30] In this sense, optimization of the band alignment at the interfaces as well as increasing interface defect passivation are relevant features to achieve an improvement in overall device performance.

Concluding the optoelectronic characterization, *J*–*V* measurements under different light intensities were carried out applying various neutral density filters after the AM1.5G illumination (Figure S3, Table S2, Supporting Information). Plotting the short-circuit current density as a function of light intensity can serve as a tool for checking if monomolecular recombination or bimolecular recombination dominate in the device. From 20 to 100 mW cm^{-2} of power density, the data shows linear dependency, indicating that monomolecular recombination is the dominant mechanism.[30]

Summarizing the optical and optoelectronic characterizations, the device with a thicker a-Si:H layer (30 nm) presents an AVT = 35.4%, CRI = 75, and PCE = 1.95%, yielding a LUE = 0.7%. For the thinner device with 8 nm a-Si:H film, the respective parameters are AVT = 66.0%, CRI = 85, and PCE = 0.56%, yielding an LUE = 0.4%. The thinner sample excels in transparency and color neutrality, while the thicker sample shows the higher LUE and PCE values reported so far for this kind of devices. These results highlight that differences in the thickness of the layers have much higher impact in TPV technologies as compared to conventional opaque PV.

2.3. Spectral Response

Spectral response measurements were performed on both 8 and 30 nm a-Si:H devices to compare and analyze their response (**Figure 4**a). The external quantum efficiency (EQE) maximum

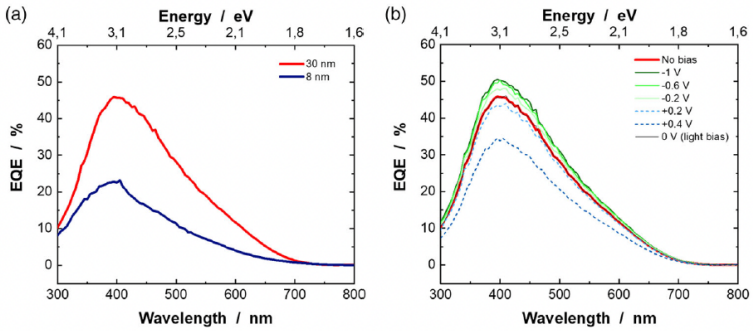

Figure 4. a) Comparison of external quantum efficiency (EQE) of device with 30 nm a-Si:H film and a device with 8 nm a-Si:H film. b) EQE extracted from spectral response measurements on a device with a-Si:H film of 30 nm. EQE is shown with no bias, with white light bias and at different negative electrical biases from +0.4 to −1 V.

© 2023 The Authors. Solar RRL published by Wiley-VCH GmbH

is located at 400 nm in both cases in their respective EQE spectra, showing a steep drop in response toward lower photon energies. As expected, the spectral response of the thinner 8 nm device is lower than for the 30 nm device, but presents a similar profile across the spectral range. This behavior supports that the UV–blue selective absorption responds to the ultrathin nature of the films, which results in a frustrated long wavelength absorption. It is also worth noting that wavelength-selective behavior is not always observed with ultrathin absorber materials. As example, in Ref. [31], ultrathin CIGS devices are presented exhibiting a "flat" EQEs across the whole range from 300 nm to the wavelength corresponding to the energy bandgap of CIGS, showing transparency, but also leveled broadband photoresponse.

In Figure 4b, a detailed analysis on the EQE of the best device at different light and electrical biases is presented. Under either conditions (i.e., with or without electrical bias), the maximum EQE is still located at 400 nm. The spectrum obtained under no light exposure remains almost identical as the one under uniform white light, which indicates good carrier collection irrespectively of bulk illumination. When applying increasingly negative electrical biases, there is a slight enhancement in quantum efficiency of the TPV device. The small change suggests that most of the photogenerated carriers in the a-Si:H absorber reach the interfaces with the CTLs. The relative increase, as compared with the spectra of the device under no electrical bias, is most notable near the EQE peak and almost negligible at wavelengths longer than 450 nm, suggesting improved photocarrier collection mainly near the front interface. The EQE noticeably degrades for positive bias voltages, as it could be expected for the dominant drift-assisted carrier collection in this device architecture. This reduction at high bias could also be an indication of the existence of some transport barrier at the CTL/a-Si:H interfaces. To confirm that no overestimation of J_{sc} has been done, a photon balance check is presented in Figure S4.

3. Conclusion

We have studied the potential of nanometric intrinsic a-Si:H/oxide structures for TPV applications in a metal-free device architecture including transparent conductive oxides as electrical contacts. The optical properties of the ultrathin a-Si:H films have been experimentally determined by spectrophotometric measurements and the Urbach energy of ultrathin a-Si:H absorbers has been determined. Spectral response and optoelectronic measurements have proved a preferential absorption of short wavelengths (UV–blue) from the solar spectra while still presenting high AVT values, comparable to those of full oxide UV-selective devices. The reported devices present a record efficiency of PCE = 2% and AVT = 35.4% (LUE = 0.7%) and PCE = 0.6% and AVT = 66% (LUE = 0.4%) with a 30 and 8 nm a-Si:H film, respectively. Use of substrates with sizes up to $5 \times 5\,cm^2$ has allowed to achieve good statistics to analyze the reproducibility of the results when working with 0.07 cm^2 active area devices that have been defined using a metallic shadow mask during ITO deposition. A first attempt for process upscaling has also been done with the fabrication of a $5 \times 5\,cm^2$ solar cell. However, even in this case, the devices show a dramatic drop in the device efficiency to values lower than 0.1%. This is likely mainly related to the high series resistance of the ITO front contact, which determines a drastic loss in device efficiency. This implies the need for a redesign of the fabrication process when using higher area devices and possibly the introduction of a metallic grid with finger thicknesses of around 100 µm, which could allow to have a nonintrusive grid for efficient carrier collection. Nonetheless, we have demonstrated the potential of the technology using smaller active area, which allowed avoiding these resistive and parasitic losses when upscaling. The results detailed in this work represent a great improvement as compared to state-of-the-art devices with similar architectures. To further improve these TPV devices, it is necessary to optimize their architecture by paying special attention to the interfaces. These structures show a promising route for opening alternative PV applications with seamless integration. Applications of this technology can potentially include BIPV, VIPV, APV, low-power demand applications such as powering future internet of things devices and as self-powered light sensors. The TPV devices present multifunctional capabilities, such as good UV filtering, that add up to the PV effect. To conclude, it is worth noting that all materials and processes used in this work are scalable and compatible with existing and established industries, using low process temperatures as well as earth-abundant, stable, and low-cost materials, which are also key features to have a future deployment of such technologies at an industrial level.

4. Experimental Section

Sample Preparation: The solar cells fabricated in this work presented the structure SLG/FTO/AZO/a-Si:H(8, 30 nm)/MoO_3/ITO with active area of 0.07 cm^2. Commercial SLG/FTO substrates (Merck; $R_{sh} = 10\,\Omega sq^{-1}$) were used as substrate and transparent back-contact for the solar cell devices. Substrates were rinsed in distilled water, dried in Ar flux, and afterward cleaned by subsequent ultrasonic baths in isopropanol and ultrapure H_2O at room temperature for 10 min each. Afterward, the substrates were dried in Ar flux and finally submitted to a 5 min O_3 treatment. A 75 nm AZO film was grown in an atomic layer deposition (ALD) system (Savannah S200, Cambridge Nanotech) at 135 °C. The precursors used are diethylzinc (DEZ 95%, STREM), ultrapure H_2O and trimethylaluminium (TMA 99%, STREM) and using N_2 as purging gas, with a DEZ:TMA ratio of 19:1. 21 supercycles were performed with 19 H_2O/N_2/DEZ/N_2 (20 ms/3 s/15 ms/3 s) cycles and 1 H_2O/N_2/TMA/N_2 (50 ms/1 s/20 ms/5 s) cycle. Afterward, intrinsic a-Si:H ultrathin films of 8 and 30 nm were deposited by plasma-enhanced chemical vapor deposition (PE-CVD) (Elettrorava) with an radio frequency (RF) power supply of 13.56 MHz at 6 W. Substrate temperature was measured at 220–250 °C during deposition, with a mixed 36/12 sccm SiH_4/CH_4 atmosphere and with deposition times of 1 and 4 min, respectively (thickness calibration has been determined by means of a profilometer) (KLA Tencor D-120), studying films with varying deposition times. Additionally, thin layers comparable to the ones studied in this work were characterized by high-resolution transmission electron microscopy (HRTEM) at the advanced microscopy laboratory (Laboratorio de Microscopia Avanzada (LMA), Universidad de Zaragoza). The deposition rate for the conditions used in this work was about $1.3\,Å\,s^{-1}$. MoO_3 films of 10 nm were deposited by thermal evaporation (Oerlikon Univex 250) using raw MoO_3 powder (99.995%, Alfa Aesar) as evaporant in a tungsten boat. The chamber was evacuated to a base pressure of 10^{-6} mbar before evaporation and the deposition took place at room temperature at a rate of $0.3\,Å s^{-1}$ as measured with a Ag-coted 6 MHz quartz crystal microbalance (Inficon SQC-310). To complete the device, a 190 nm ITO film working as front contact was deposited by DC-Pulsed Confocal Magnetron Sputtering (Alliance CT-100). Before deposition, the chamber was evacuated at 10^{-7} mbar and the substrate

© 2023 The Authors. Solar RRL published by Wiley-VCH GmbH

was heated up to 200 °C. The ITO target (Neyco; In_2O_3/SnO_2 90/10 wt%, 4 N) was pre-sputtered with a shutter in closed configuration to remove any surface contaminants. The deposition took place at a working pressure of 3×10^{-3} mbar in a mixed 30/0.5 sccm Ar/O_2 atmosphere, applying a DC power density of 1.9 Wcm^{-2} to the target.

Characterization: The optical absorption of quartz/a-Si:H samples was characterized by PDS. A single-slab model was applied to compute the absorption coefficient. The transverse PDS setup used in this work consisted of a 100 W tungsten halogen lamp, PTI 01-0002 monochromator (two-grating monochromator, spectral range of 400–2000 nm), and Thorlabs MC1000 optical chopper (4 Hz light modulation frequency). A Signal Recovery 7265 lock-in amplifier was connected to a Hamamatsu C10442-02 position-sensitive detector (Hamamatsu C10442-02 PSD) to measure the deflection of an MC632C 10 mW laser probe beam. Samples were put in a quartz cell filled with Fluorinert TM FC-40. A personal computer was used to control the monochromator, change the order filters, and store the PDS signal read from the lock-in amplifier.[32]

Spectrophotometry measurements were acquired with a UV–visible–NIR spectrophotometer (Perkin Elmer Lambda L950) with an integrating sphere and in single-beam setup, in transmittance and reflectance mode with spectral range from 300 to 800 nm to measure the completed device total transmittance and reflectance. This data was also used to calculate the device AVT and CRI.

J–*V* measurements under illumination were carried out using a class AAA solar simulator with AM1.5G illumination calibrated using an NREL-certified Si reference solar cell (Abet Technologies Model 15150). Electrical measurements were carried out with a source–measure unit (Keithley SMU 2400) in 4-wire sense mode, remotely controlled by the software Tracer (ReRa solutions) using an IEEE 488 GPIB Instrument Control Device (National Instruments GPIB-USB-HS). Spectral response measurements were acquired using a spectral response system (Bentham PVE300) calibrated with Si and Ge photodiodes. For optoelectronic measurements, the samples were placed in a dark opaque matt to avoid any back reflections that could alter the characterization of the transparent solar cells.

Supporting Information

Supporting Information is available from the Wiley Online Library or from the author.

Acknowledgements

This work has received funding from the European Union H2020 Framework Programme under Grant Agreement no. 826002 (Tech4Win). This work is also part of the R + D + i MaterOne projects (Refs. PID 2020-116719RB-C42 and PID 2020-116719RB-C41) and of the R + D + i SCALED project (Ref. PID 2019-109215RB-C4) funded by MCIN/AEI/10.13039/5011000110033. Authors from IREC belong to the SEMS (Solar Energy Materials and Systems) Consolidated Research Group of the "Generalitat de Catalunya" (Ref. 2017 SGR 862).

Conflict of Interest

The authors declare no conflict of interest.

Data Availability Statement

The data that support the findings of this study are openly available in Zenodo repository at http://doi.org/10.5281/zenodo.7215223.

Keywords

a-Si:H, hydrogenated amorphous silicon, oxides, selective contacts, transparent photovoltaics, wavelength-selective solar cells, wide-bandgap

Received: October 17, 2022
Revised: January 19, 2023
Published online:

[1] G. Masson, I. Kaizuka, can be found under, https://iea-pvps.org/wp-content/uploads/2020/02/5319-iea-pvps-report-2019-08-lr.pdf (accessed: October 2022).
[2] C. J. Traverse, R. Pandey, M. C. Barr, R. R. Lunt, *Nat. Energy* **2017**, *2*, 849.
[3] R. R. Lunt, *Appl. Phys. Lett.* **2012**, *101*, 43902.
[4] C. Yang, D. Liu, M. Bates, M. C. Barr, R. R. Lunt, *Joule* **2019**, *3*, 1803.
[5] R. Karsthof, P. Räcke, H. Von Wenckstern, M. Grundmann, *Phys. Status Solidi A* **2016**, *213*, 30.
[6] M. Patel, H. Kim, J. Kim, J. Yun, S. Jin, E. Ha, H. Park, *Sol. Energy Mater. Sol. Cells* **2017**, *170*, 246.
[7] D. K. Ban, M. Patel, T. T. Nguyen, J. Kim, *Adv. Electron. Mater.* **2019**, *5*, 1900348.
[8] A. J. Lopez-Garcia, A. Bauer, R. Fonoll Rubio, D. Payno, Z. Jehl Li-Kao, S. Kazim, D. Hariskos, V. Izquierdo-Roca, E. Saucedo, A. Pérez-Rodríguez, *Sol. RRL* **2020**, *4*, 2000470.
[9] S. Kim, M. Patel, T. T. Nguyen, J. Yi, C. P. Wong, J. Kim, *Nano Energy* **2020**, *77*, 105090.
[10] A. J. Lopez-Garcia, O. Blazquez, C. Voz, J. Puigdollers, V. Izquierdo-Roca, A. Pérez-Rodríguez, *Sol. RRL* **2022**, *6*, 2100909.
[11] M. Patel, J. H. Seo, T. T. Nguyen, J. Kim, *Cell Rep. Phys. Sci.* **2021**, *2*, 100591.
[12] S. Kim, J. Yi, J. Kim, *Sol. RRL* **2021**, *5*, 2100162.
[13] M. Patel, S. Kim, T. T. Nguyen, J. Kim, C.-P. Wong, *Nano Energy* **2021**, *90*, 106496.
[14] M. Patel, V. Vitthal Satale, S. Kim, K. Lee, J. Kim, *J. Power Sources* **2022**, *548*, 232009.
[15] S. Kim, M. Patel, T. T. Nguyen, N. Kumar, P. Bhatnagar, J. Kim, *ACS Appl. Mater. Interfaces* **2022**, *14*, 706.
[16] Y. Abdulraheem, I. Gordon, T. Bearda, H. Meddeb, J. Poortmans, *AIP Adv.* **2014**, *4*, 057122.
[17] F. Urbach, *Phys. Rev.* **1953**, *92*, 1324.
[18] J. Chantana, Y. Kawano, T. Nishimura, A. Mavlonov, T. Minemoto, *Sol. Energy Mater. Sol. Cells* **2020**, *210*, 110502.
[19] G. D. Cody, in *Semiconductors and Semimetals* (Eds: J. I. Pankove), Vol. *21*, Elsevier, Amsterdam, Netherlands **1984**, pp. 11–82, Chapter 2.
[20] T. M. Mok, S. K. O'Leary, *J. Appl. Phys.* **2007**, *102*, 113525.
[21] K. Higuchi, K. Tabuchi, K. S. Lim, M. Konagai, K. Takahashi, *Jpn. J. Appl. Phys.* **1991**, *30*, 1635.
[22] V. Dalal, R. Knox, B. Moradi, *Sol. Energy Mater. Sol. Cells* **1993**, *31*, 349.
[23] A. Pérez-Rodríguez, in *presented in NEXTGEN, 19: 2019 Next Generation High Efficiency Photovoltaics Int. School and Workshop*, Mallorca, October **2019**.
[24] T. Matsui, K. Maejima, A. Bidiville, H. Sai, T. Koida, T. Suezaki, M. Matsumoto, K. Saito, I. Yoshida, M. Kondo, *Jpn. J. Appl. Phys.* **2015**, *54*, 08KB10.
[25] M. Stuckelberger, R. Biron, N. Wyrsch, F.-J. Haug, C. Ballif, *Renewable Sustable Energy Rev.* **2017**, *76*, 1497.
[26] K. Belrhiti Alaoui, S. Laalioui, Z. Naimi, B. Ikken, A. Outzourhit, *AIP Adv.* **2020**, *10*, 095315.

© 2023 The Authors. Solar RRL published by Wiley-VCH GmbH

[27] S. S. Hegedus, W. N. Shafarman, *Prog. Photovoltaics Res. Appl.* **2004**, *12*, 155.
[28] S. Suckow, T. M. Pletzer, H. Kurz, *Prog. Photovoltaics Res. Appl.* **2014**, *22*, 494.
[29] G. Yue, B. Yan, C. Teplin, J. Yang, S. Guha, *J. Non-Cryst. Solids* **2008**, *354*, 2440.
[30] S. Ryu, D. C. Nguyen, N. Y. Ha, H. J. Park, Y. H. Ahn, J.-Y. Park, S. Lee, *Sci. Rep.* **2019**, *9*, 19846.
[31] M. Jeong Shin, A. Lee, J. Hyung Park, A. Cho, S. Kyu Ahn, D. Shin, J. Gwak, J. Ho Yun, J. Yoo, J.-S. Cho, *Nano Energy* **2022**, *92*, 106711.
[32] J. Serra, J. Andreu, G. Sardin, C. Roch, J. M. Asensi, J. Bertomeu, J. Esteve, *Phys. B Condens. Matter* **1991**, *170*, 269.

© 2023 The Authors. Solar RRL published by Wiley-VCH GmbH

Ultrathin a-Si:H/oxide transparent solar cells exhibiting UV-blue selective-like absorption

A.J. Lopez-Garcia, C. Voz, J.M. Asensi, J. Puigdollers, V. Izquierdo-Roca, A. Pérez-Rodríguez*

The α(E) spectra for the band-to-band and Urbach tail regions is calculated from the following equations:

$$\alpha(E) = \begin{cases} \alpha_{Cody}(E) = BE(E - E_g)^2 & \text{If } E \geq E_1 \\ \alpha_{Urbach}(E) = \alpha_0 \exp\left(\frac{E}{E_U}\right) & \text{If } E \leq E_1 \end{cases} \qquad (S1)$$

where E_1 is a transition energy near the optical gap (E_g) where the following equalities must be fulfilled:

$$\alpha_{Cody}(E_1) = \alpha_{Urbach}(E_1) \qquad (S2a)$$

$$\frac{d\alpha_{Cody}}{dE}(E_1) = \frac{d\alpha_{Urbach}}{dE}(E_1) \qquad (S2b)$$

A Gaussian model is used to describe the sub-gap absorption:

$$\alpha_D(E) = \alpha_{D0} \exp\left(\frac{E - E_D}{\Delta E_D}\right)^2 \qquad (S3)$$

The total absorption coefficient (the black solid line in **Figure S1**) is obtained by adding Equation S1, S2 and S3.

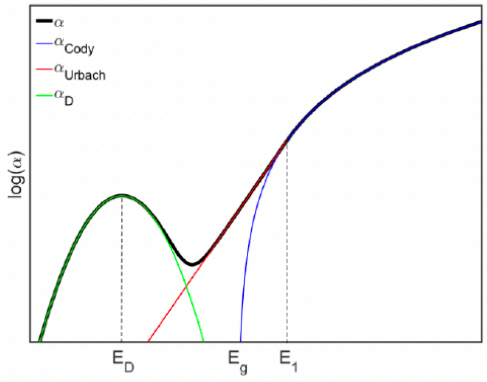

Figure S1. Model used to describe the absorption coefficient of ultrathin layers of a-Si:H on quartz.

Table S1. Summary of parameters extracted from fitting the experimental α(E) spectra

Sample	Bant-to-band & Urbach tail absorption[a]					Sub-gap absorption		
	E_1 [eV]	E_u [meV]	α_0 [cm^{-1}]	E_g [eV]	B [$eV^{-3}cm^{-1}$]	α_{D0} [cm^{-1}]	E_D [eV]	ΔE_D [meV]
Quartz/a-Si:H (8 nm)	1.86	78	$2.05 \cdot 10^{-7}$	1.69	864	822	1.31	131
Quartz/a-Si:H (30 nm)	1.89	84	$9.72 \cdot 10^{-7}$	1.71	872	232	1.31	147

(a) Note that in the model for band-to-band and Urbach absorption (Equation S1 and S2) there are only 3 independent parameters. In the fitting procedure the transition energy (E_1) and band tail parameters (E_u and α_0) are used as independent parameters. The optical gap energy (E_g) and the prefactor (B) are derived from these values by solving Equation S1 and S2.

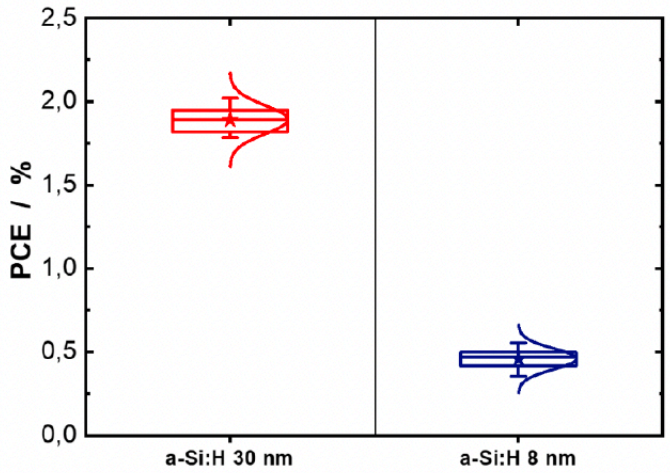

Figure S2. Box plot with distribution profile showing statistics on the fabricated TPV devices with a-Si:H films of 30 nm (N=5) and 8 nm (N=10).

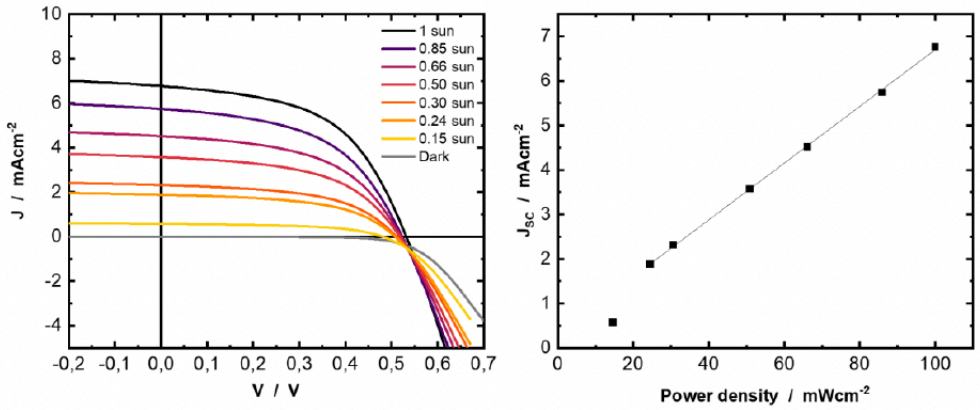

Figure S3. J-V characteristics under AM1.5G illumination at different light intensities using different neutral density filters.

Table S2. Device efficiency as a function of illumination intensity

Illumination intensity	PCE [%]
1 sun	1.95
0.85 sun	1.82
0.66 sun	1.85
0.50 sun	1.91
0.30 sun	2.10
0.24 sun	2.10
0.15 sun	1.00

Table S3. Summary of parameters extracted from fitting J-V characteristics to a single diode model.

Fitting model (device)	A	R_s [Ωcm^2]	R_{sh} [Ωcm^2]	J_0 [Acm^{-2}]
1-diode (30 nm)	1.94	11	$3.2 \cdot 10^4$	$9.4 \cdot 10^{-7}$
1-diode (8 nm)	2.69	41	$3.8 \cdot 10^3$	$1.4 \cdot 10^{-6}$

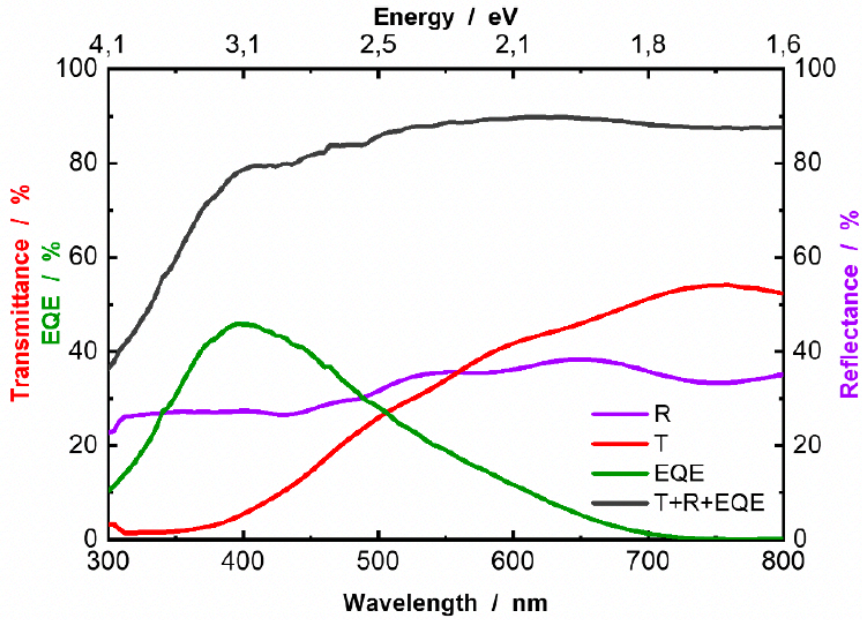

Figure S4. Photon balance check. Device transmittance, reflectance and EQE of device are provided. The sum of the three components shall be <100% in order to confirm that no overestimation of J_{sc} is being done.

4 - Conclusions and Outlook

The ultimate objective of the research conducted within this thesis was to pioneer and jumpstart a novel research line in next generation photovoltaics within the group at IREC that explored the use of inorganic materials as UV-selective absorbers that are transparent in the visible range (and thus to the human eye) in order to develop smart, clean and resource efficient solutions for localized applications, with a main focus of solar windows for on-site and distributed energy generation. In this context, the achievement of record functional UV-selective TPV devices with power conversion efficiencies ranging from 0.5% up to 2% and with average visible transmittance ranging from 69% to 35%, permitted to consolidate a research line exploring and developing these inorganic based transparent solutions. Specifically, the work focused on the comprehension and optimization of mostly oxide-based materials and structures as well as ultrathin a-Si:H absorbers in the research facilities available for the SEMS group laboratories. So far, the work presented has shown fruitful results in the form of record devices when compared to state-of-the-art work in this field and is showing promise for further improving device efficiency as well as consolidating the understanding of this specific technology which has become an emerging topic that is becoming increasingly relevant within the PV field in the recent years and also outside of the specialists field, being sought out by the industry in order to further expand the PV toolkit for deployment in real world applications.

Transparent Photovoltaics is still a quite novel and niche field but it is strongly gaining traction and becoming an increasingly notorious and pursued topic that can allow for ubiquitous integration with low visual impact and very high applicability in real-life industrially viable products. In the framework and context of the SEMS research group, there was no prior work on this technology, so significant effort had to be put in, from the basic understanding of the fundamental aspects of the technology to establishing suitable methodologies within the group labs in order to characterize these devices.

In the initial stages of the thesis the work began by developing ZnO films via sputtering and fabricate TPV devices based on this material, in an attempt to reproduce and match what was present in SoA in inorganic TPV technologies, which revolved around the use of this material. However, it was well known that this material presents very limited absorption and thus had a low potential for improvement and attainment of TPV devices. Nonetheless, the work served as an introduction to the field and first steps towards the planning of future devices implemented the novelty of using mixed crystal via anionic substitution of oxygen with chalcogenide, which showed promise of obtaining materials with a lower bandgap while keeping high transparency and aesthetics while promising way higher efficiency, all of which was carried in the next stage of the thesis. As so, in this initial stage of the thesis the main efforts were placed in synthesis approaches of the ZnO films as well as the synthesis of many other potential oxide candidates to be used as Charge Transport Layers (CTL) in the final TPV devices. All these synthesis techniques mainly relied on physical vapour deposition approaches, using sputtering and evaporation techniques. Complementarily, different characterization tools were used to assess the viability of use of the different layers. For this, different techniques were used, such as Raman spectroscopy, UV-VIS spectrophotometry, resistivity measurements, XRD, and FE-SEM. Finally, given the novelty of the work within the group, different protocols and methodology were implemented for the fabrication and characterization of the TPV devices. Adequate measurement protocols and setups were designed, highlighting the preparation of a UV-specific light source closely matching the Sun's spectrum and establishing a calibration protocol for measurements, as well as creating a measurement protocol establishing the voltage and current limits as well as the polarization needed to be applied to characterize these devices.

In the second stage of the thesis, the primal effort was placed in the development of the novel Zn(O,S) mixed crystal absorbers as well as its characterization and the implementation of TPV devices based on this approach. The results of this work led to the first research article presented in Chapter 3.

As part of the next stage, a-Si:H was explored as a candidate for absorber material in TPV devices, while conserving the strategy of developing a

solar cell with CTL/absorber/CTL architecture and building up on the previous knowledge developed throughout the first experimental stage of the doctoral period. The results of this later stage resulted in the second and third research articles presented in Chapter 3.

Table 2: Device comparative between the thesis results and SoA best performing devices.

Optoelectronic TPV parameters	This thesis (Zn(O,S))[37]	This thesis (a-Si:H)[38]	(ZnO)[18]	(a-Si:H)[36]
J_{sc} [mA/cm²]	3.64*	7.24	0.80	2.70
V_{oc} [mV]	450	528	815	0.598
FF [%]	28.5	51	86.1	34
PCE [%]	0.50*	1.95*	0.56*	0.55
AVT [%]	69.3	35.4	74	40

*PCE value based on simulation using AM1.5G. Reported a 3.13% PCE under intense UV.

As a final remark, the results achieved in this thesis included the first report in scientific literature on Transparent PV devices using Zn(O,S) mixed crystal as an absorber and the synthesis and characterization of record TPV devices based on ultrathin a-Si:H/oxide architectures, overcoming the bottleneck that was present for UV-selective pure oxide-based devices (Table 2). The research performed during this thesis and the resulting knowledge presented in scientific publications is reflected in an important number of citations, totalling 25 citations at the present time. Additionally, the work has been presented in different international scientific conferences and workshops, having presented the work with contributions including oral presentations, poster presentations and an invited talk. Within the SEMS group, the impact of this research has been notable: it has allowed to successfully complete a pilot H2020 European project (Tech4Win), it has become an important research line and topic within the SEMS group and further development of these technologies is being pursued in the form of different national and European project proposals that have found support and a starting basis in this work. The consecution of this work was also possible thanks to the collaborative work performed with different partners including national and international research groups as well as collaboration with industrial partners with expertise in the field.

Bibliography

[1] R. Aymar, *IEEE Trans. plasma Sci.* **1997**, *25*, 1187.

[2] N. Holtkamp, I. P. Team, *Fusion Eng. Des.* **2007**, *82*, 427.

[3] *Economic Evaluation of Alternative Nuclear Energy Systems*, INTERNATIONAL ATOMIC ENERGY AGENCY, Vienna, **2022**.

[4] IEA, *World Energy Outlook 2023*, Paris, **2023**.

[5] IEA, *Global Energy and Climate Model*, Paris, **2023**.

[6] S. Philipps, F. ISE, W. Warmuth, P. Projects GmbH, *Photovoltaics Report*, **2023**.

[7] C. J. Traverse, R. Pandey, M. C. Barr, R. R. Lunt, *Nat. Energy* **2017**, *2*, 849.

[8] P. Heinstein, C. Ballif, L.-E. Perret-Aebi, *Green* **2013**, *3*, 125.

[9] X. Lin, Y.-L. Loo, M. Sezen-Edmonds, N. C. Davy, J. Gao, A. Liu, A. Kahn, N. Yao, *Nat. Energy* **2017**, *2*, 17104.

[10] Q. Xue, R. Xia, C. J. Brabec, H. L. Yip, *Energy Environ. Sci.* **2018**, *11*, 1688.

[11] S. Schindele, M. Trommsdorff, A. Schlaak, T. Obergfell, G. Bopp, C. Reise, C. Braun, A. Weselek, A. Bauerle, P. Högy, A. Goetzberger, E. Weber, *Appl. Energy* **2020**, *265*, 114737.

[12] F. Grifoni, M. Bonomo, W. Naim, N. Barbero, T. Alnasser, I. Dzeba, M. Giordano, A. Tsaturyan, M. Urbani, T. Torres, C. Barolo, F. Sauvage, *Adv. Energy Mater.* **2021**, 2101598.

[13] G. Kim, J. W. Lim, J. Kim, S. J. Yun, M. A. Park, *ACS Appl. Mater. Interfaces* **2020**, *12*, 27122.

[14] J. Ramanujam, D. M. Bishop, T. K. Todorov, O. Gunawan, J. Rath, R. Nekovei, E. Artegiani, A. Romeo, *Prog. Mater. Sci.* **2020**, *110*, 100619.

[15] P. Santos, P. Anacleto, D. Brito, S. Shital, R. G. Poeira, A. Debot, P. J. Dale, S. Sadewasser, *Thin Solid Films* **2023**, *770*, 139778.

[16] K. Ellmer, A. Bikowski, *J. Phys. D. Appl. Phys.* **2016**, *49*.

[17] M. Grundmann, F. Klüpfel, R. Karsthof, P. Schlupp, F. L. Schein, D. Splith, C. Yang, S. Bitter, H. Von Wenckstern, *J. Phys. D. Appl. Phys.* **2016**, *49*.

[18] D. K. Ban, M. Patel, T. T. Nguyen, J. Kim, *Adv. Electron. Mater.* **2019**, *5*, 1.

[19] T. T. Nguyen, M. Patel, J. Kim, *Sol. Energy Mater. Sol. Cells* **2020**, *217*.

[20] R. Karsthof, P. Räcke, H. Von Wenckstern, M. Grundmann, *Phys. status solidi* **2016**, *213*, 30.

[21] M. Patel, H. Kim, J. Kim, J. Yun, S. Jin, E. Ha, H. Park, *Sol. Energy Mater. Sol. Cells* **2017**, *170*, 246.

[22] C. Persson, C. Platzer-Björkman, J. Malmström, T. Törndahl, M. Edoff, *Phys. Rev. Lett.* **2006**, *97*, 1.

[23] M. Guc, M. Neuschitzer, D. Hariskos, A. Bauer, W. Witte, W. Hempel, L. Calvo-Barrio, P. Pistor, A. Perez-Rodriguez, V. Izquierdo-Roca, *RSC Adv.* **2016**, *6*, 24536.

[24] A. Polity, B. K. Meyer, T. Krämer, C. Wang, U. Haboeck, A. Hoffmann, *Phys. status solidi* **2006**, *203*, 2867.

[25] G. Baldissera, C. Persson, *J. Appl. Phys.* **2016**, *119*.

[26] P. Würfel, U. Würfel, *Physics of Solar Cells*, Wiley-VCH, **2013**.

[27] S. M. Sze, K. K. Ng, *Physics of Semiconductor Devices*, John Wiley & Sons, Hoboken, New Jersey, **2008**.

[28] A. H. Smets, K. Jäger, O. Isabella, R. A. van Swaaij, M. Zeman, *Solar Energy*, UIT Cambridge, **2011**.

[29] W. Shockley, H. J. Queisser, *J. Appl. Phys.* **1961**, *32*, 510.

[30] J. F. Guillemoles, T. Kirchartz, D. Cahen, U. Rau, *Nat. Photonics* **2019**, *13*, 501.

[31] R. R. Lunt, *Appl. Phys. Lett.* **2012**, *101*, 43902.

[32] T Smith, J Guild, *Trans. Opt. Soc.* **1931**, *33*, 73.

[33] C. Yang, D. Liu, M. Bates, M. C. Barr, R. R. Lunt, *Joule* **2019**, *3*, 1803.

[34] A. Pérez-Rodríguez, in *Nanotechnol. Next Gener. High Effic. Photovoltaics Int. Sch. Work.*, **2019**.

[35] M. Guc, D. Hariskos, L. Calvo-Barrio, P. Jackson, F. Oliva, P. Pistor, A. Perez-Rodriguez, V. Izquierdo-Roca, *Sci. Rep.* **2017**, *7*, 1.

[36] S. Kim, M. Patel, T. T. Nguyen, J. Yi, C. P. Wong, J. Kim, *Nano Energy* **2020**, *77*, 105090.

[37] A. J. Lopez-Garcia, A. Bauer, R. Fonoll Rubio, D. Payno, Z. Jehl Li-Kao, S. Kazim, D. Hariskos, V. Izquierdo-Roca, E. Saucedo, A. Pérez-Rodríguez, *Sol. RRL* **2020**, *4*, 2070112.

[38] A. J. Lopez-Garcia, C. Voz, J. M. Asensi, J. Puigdollers, V. Izquierdo-Roca, A. Pérez-Rodríguez, *Sol. RRL* **2023**, *7*, 2200928.

Appendix A

UV-Selective Optically Transparent Zn(O,S)-based Solar Cells Featured Cover

Alex J. Lopez-Garcia*, A. Bauer, R. Fonoll, D. Payno, Z. Jehl, S. Kazim, D. Hariskos, V. Izquierdo-Roca, E. Saucedo, A. Pérez-Rodríguez

Permission conveyed through Copyright Clearance Center. Republished with permission of © John Wiley and Sons, from Solar RRL, UV-Selective Optically Transparent Zn(O,S)-Based Solar Cells, with license number 5574810012546.

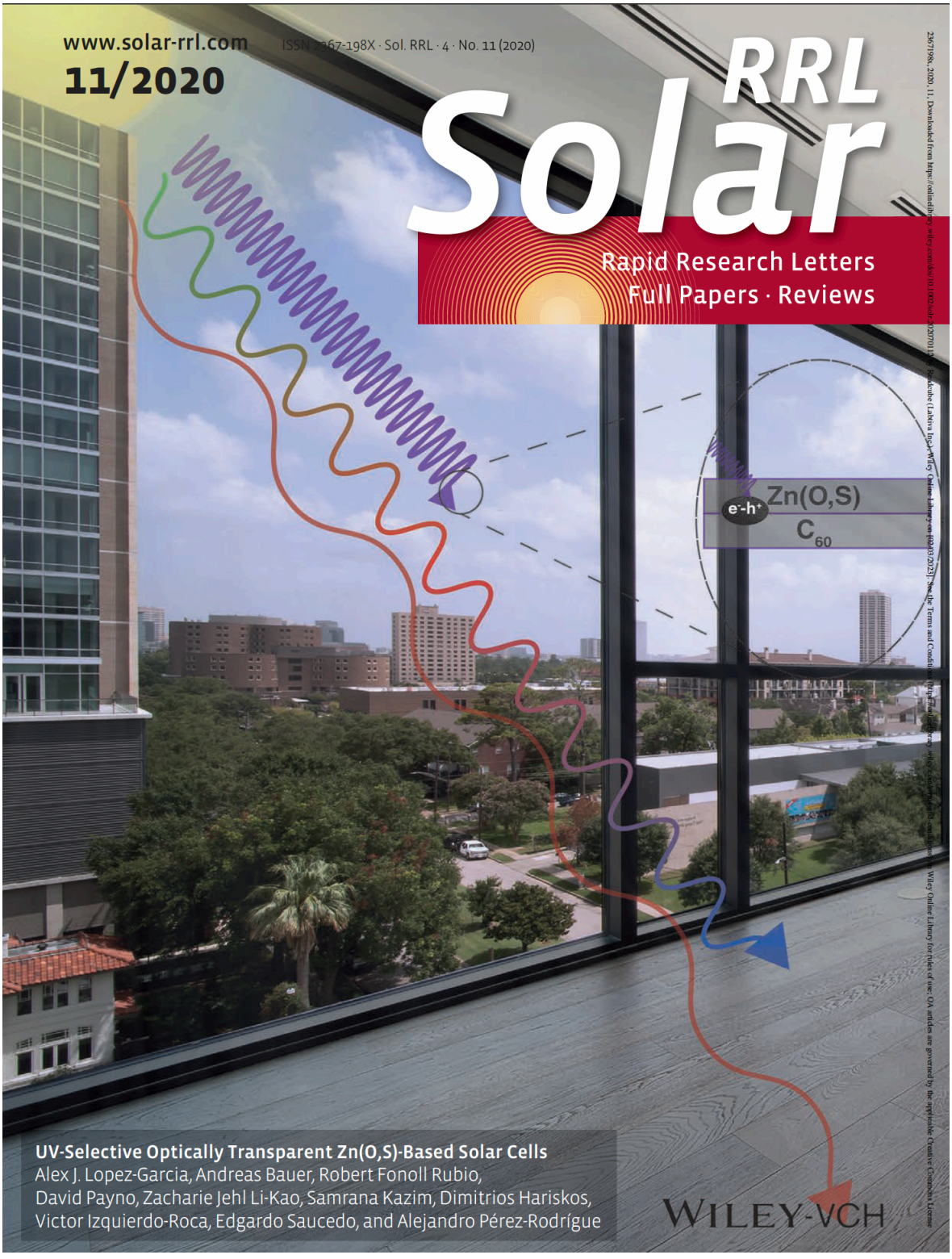

2367198x, 2020, 11, Downloaded from https://onlinelibrary.wiley.com/doi/10.1002/solr.202070113 by Readcube (Labtiva Inc.) - Wiley Online Library on [08/03/2023]. See the Terms and Conditions (https://onlinelibrary.wiley.com/terms-and-conditions) on Wiley Online Library for rules of use; OA articles are governed by the applicable Creative Commons License

Appendix B

Transversal skills, congresses, courses and workshops attended

During the 4-year period of the thesis, so many things are learnt and participation in different facets of science and communication is extensive. Many times, these aspects go unnoticed and are not highlighted; however, they are very relevant as they consequently involve added experience and growth in the context of the researcher career. In the following lines, all the transversal skills, courses and workshops attended as well as oral and poster presentations in congresses are enumerated in chronological order:

Scientific Publications

- Lopez-Garcia, A.J., Bauer, A., Fonoll Rubio, R., Payno, D., Jehl Li-Kao, Z., Kazim, S., Hariskos, D., Izquierdo-Roca, V., Saucedo, E. and Pérez-Rodríguez, A. (2020), "*UV-Selective Optically Transparent Zn(O,S)-Based Solar Cells"*, Sol. RRL, 4(11): 2000470. doi:10.1002/solr.202000470

- Lopez-Garcia, A.J., Blazquez, O., Voz, C., Puigdollers, J., Izquierdo-Roca, V., Saucedo, E. and Pérez-Rodríguez, A. (2022), "*Ultrathin Wide-Bandgap a-Si:H-based Solar Cells for Transparent Photovoltaic Applications"*, Sol. RRL, 6(1): 2100909. doi:10.1002/solr.202100909

- Lopez-Garcia, A.J., Asensi, J.M., Voz, C., Puigdollers, J., Izquierdo-Roca, V., Pérez-Rodríguez, A. (2022) "*Ultrathin a-Si:H/oxide transparent solar cells exhibiting UV-blue selective-like absorption*", Sol. RRL, 7(7), 2200928, doi: 10.1002/solr.202200928

Courses, Schools and Workshops

- Preparació de Propostes de Projectes de Recerca Europeus, Càpsula Formativa UB, June 2019

- Energy Mining in the 21st Century. Severo Ochoa Workshop on Energy Storage and Harvesting, Barcelona, Spain, July 12, 2019

- Nanotechnology and Next Generation High Efficiency Photovoltaics International School and Workshop, Palma, Mallorca, Spain, October 1 – 4, 2019

- Physics of Solar Cells: from basic principles to advanced characterization, Les Houches School of Physics, March 1-6, 2020

- Emergent Phenomena in Moiré Materials, ICFO-MIT Schools on the Frontiers of Light, Barcelona, Spain, 6-17 July, 2020

- Magnetically driven micro- and nanoswimmers, Prof. Dr. Salvador Pané i Vidal, IN2UB International Research Seminar, UB, October 2020

- La gestió de la bibliografia: l'ús del gestor bibliogràfic Mendeley, Càpsula Formativa UB, November 2020

- Estadística comprimida per a no estadìstics (C. Experimentals), Càpsula Formativa UB, November 2020

- UB's Learning and Research resources: services and resources, Càpsula Formativa UB, November 2020

- La gestión de la bibliografía: el uso del gestor bibliográfico Mendeley (Nivel Avanzado), Càpsula Foramtiva UB, December 2020

- Managing and Sharing Research Data, Càpsula Formativa UB, December 2020

- ESpinRed School on Spintronics, Virtual, 17-31 May, 2021

- TPV Workshop Clustering Event, Roma, Italy, 27-28 April, 2022

Oral presentations

- Alex J. Lopez-Garcia, Robert Fonoll Rubio, Victor Izquierdo-Roca, Alejandro Pérez Rodríguez, Edgardo Saucedo. *Wide-bandgap all-oxide UV-selective transparent heterojunction solar cells for BIPV.* Nanotechnology and Next Generation High Efficiency Photovoltaics International School and Workshop, Palma, Mallorca, Spain, October 1 – 4, 2019

- Alex J. Lopez-Garcia, Robert Fonoll Rubio, Victor Izquierdo-Roca, Alejandro Pérez Rodríguez, Edgardo Saucedo. *Wide-bandgap UV-selective transparent solar cells based on ZnO and Zn(O,S) absorbers for BIPV applications.* European PV Solar Energy Conference and Exhibition, Lisboa, Portugal, September 7-11, 2020

- Alex J. Lopez-Garcia, Cristobal Voz, José Miguel Asensi, Joaquim Puigdollers, Victor Izquierdo Roca, Alejandro Pérez Rodríguez. *Nanometric a-Si:H/oxide for Transparent Photovoltaics.* E-MRS Spring 2022.

- Alex J. Lopez-Garcia, Cristobal Voz, José Miguel Asensi, Joaquim Puigdollers, Victor Izquierdo Roca, Alejandro Pérez Rodríguez. *Wavelength-selective Ultrathin a-Si:H/oxide Transparent Solar Cells*, WCPEC-8, Milan, Italy, September 26-30, 2022

- Alex López-García, Alejandro Pérez-Rodríguez, Víctor Izquierdo-Roca, Cristobal Voz, Joaquim Puigdollers, *Oxide-based strategies for UV-selective Transparent Solar Cells: perspectives and challenges,* Sixth International Symposium on Innovative Materials and Processes in Energy Systems (IMPRESS 2022, Barcelona, Spain, 25-27 October 2022)

Invited talks

- Alex J. Lopez-Garcia, *Oxide-based Strategies for UV-selective Transparent Solar Cells.* TPV Workshop Clustering Event, Roma, Italy, April 27 – 28, 2022

- Alejandro Pérez-Rodríguez, Alex López-García, Víctor Izquierdo-Roca, Cristobal Voz, Joaquim Puigdollers, *UV/blue selective oxide based solar cells for transparent PV: perspectives and challenges,* XVI Workshop on Condensed Matter Physics (Univ. Autónoma de Morelos, Cuernavaca, México, June 20 – 22 2022)

Poster presentations

- Alex J. Lopez-Garcia, Robert Fonoll Rubio, Zacharie Jehl Li-Kao. Victor Izquierdo-Roca, Alejandro Pérez Rodríguez, Edgardo Saucedo. *Wide-bandgap UV-selective Transparent Oxide Solar Cells for BIPV Applications*. PV School Les Houches, 01-06 March 2020.

- Alex J. Lopez-Garcia, Cristobal Voz, José Miguel Asensi, Joaquim Puigdollers, Victor Izquierdo Roca, Alejandro Pérez Rodríguez. *Ultrathin a-Si:H/oxide UV-selective transparent solar cells*. SeeFuture PV, Lausanne, Switzerland, 23-24 June 2022

- Alex J. Lopez-Garcia, Eloi Ros, Gustavo Alvarez-Suarez, Lorenzo Calvo-Barrio, Pablo Ortega, Cristobal Voz, Joaquim Puigdollers, Victor Izquierdo-Roca, Alejandro Pérez Rodríguez. *Ultrathin a-Si:H/oxide Transparent PV Devices with Improved V_{OC} via Electron Transport Layer Optimization*. MRS Spring Meeting, San Francisco, USA, 10-14 April 2023

Features in specialized scientific dissemination magazines

- Article in pv magazine: Hydrogenated amorphous silicon oxide solar cell for BIPV, VIPV, agrivoltaics. https://www.pv-magazine.com/2023/02/13/hydrogenated-amorphous-silicon-oxide-solar-cell-for-bipv-vipv-agrivoltaics/

Supervised Thesis

- Ares Lladós Flores. *Development Of $Zn_{1-X}Mg_xO$ Layers By RF-Magnetron Sputtering For Photovoltaic Applications*, Bachelor's Degree Thesis in Nanoscience and Nanotechnology, Universitat Autònoma de Barcelona (UAB), 2019-2020.

- Gustavo Álvarez Suárez. . PhD in Physics, Universitat de Barcelona/Universidad de Bogotá, 2022-ongoing.

National and International collaborations

- Collaboration with ZSW (Stuttgart) in the planning, development and synthesis of Zn(O,S) films with different relative sulfur content via sputtering deposition.

- Collaboration with different institutions, national and international, within the Tech4Win consortium. Direct collaboration with imec (Belgium) as part of a dedicated work package related to the development of UV-selective TPV devices based on oxides and chalcogenides. Participation in optical characterization of thin films with CEA (France). Participation in upscaling of processes and optical characterization of final window concept mini-module with imec and industrial partner Onyx (Spain).

- Collaboration with the MNT Group and Photovoltaic group at Universitat Politècnica de Catalunya (UPC). Direct access and work in Clean Room for the development of ultrathin a-Si:H absorber films.

Transversal and specific skills

- Writing and generating internal reports, technical reports and official deliverables within the Tech4Win and FOTO-CER projects. Direct participation in consortium meetings.

- Collaboration with national and international research and industrial institutions.

- Planning and Supervision of bachelor's degree Thesis and PhD Thesis students.

- Extensive experience working in Clean Room environment with different synthesis equipment.

- Development of presentation and divulgation skills in international and national projects and in national and international congresses (oral presentations, invited talks, poster presentations).

- Direct involvement in the preparation of public tender for the purchase, deployment and running-up of an Atomic Layer Deposition system for deposition of oxides and chalcogenides.

- Basic user level in the following techniques: X-Ray Fluorescence (XRF), XRD, Raman spectroscopy, Spectral Response measurements, J-V-T (dark and under illumination) measurements at low temperatures, UV lithography and development, Spectral Ellipsometry.

- Advanced user level in the following synthesis and characterization techniques: DC-Pulsed and RF Confocal Magnetron Sputtering system, Thermal and electron-beam evaporation, 4pp resistivity measurements, reactive annealing in tubular furnaces from mid vacuum to atmospheric pressure, wet chemical etching with different acids, mechanical scribing, FE-SEM, UV-VIS Spectroscopy, PE-CVD, Spin-coating, Atomic Layer Deposition, Optoelectronic characterization (J-V dark and under illumination).

- Participation as reviewer for scientific publications in different journals, including a Q1 high IF journal (Sol. RRL).